2007

QUANTITATIVE THREE DIMENSIONAL ELASTICITY IMAGING

QUANTITATIVE THREE DIMENSIONAL

ELASTICITY IMAGING

MICHAEL SCOTT RICHARDS

Dissertation submitted in partial fulfillment

of the requirements for the degree of

Doctor of Philosophy

BOSTON

UNIVERSITY

BOSTON UNIVERSITY

COLLEGE OF ENGINEERING

Dissertation

QUANTITATIVE THREE DIMENSIONAL ELASTICITY IMAGING

by

MICHAEL SCOTT RICHARDS

B.S., University of Rochester, 2001

Submitted in partial fulfillment of the

requirements for the degree of

Doctor of Philosophy

2007

Approved by

First Reader
_____

Paul E. Barbone, Ph.D.
Professor of Aerospace and Mechanical Engineering, Boston University

Second Reader
_____

Kenneth R. Lutchen, Ph.D.
Dean of the College of Engineering, Boston University

Third Reader
_____

Assad A. Oberai, Ph.D.
Assistant Professor of Aerospace, Mechanical and Nuclear Engineering, Rensselaer Polytechnic Institute

Fourth Reader
_____

Dimitrije Stamenovic, Ph.D.
Associate Professor of Biomedical Engineering, Boston University

Fifth Reader
_____

Irving Bigio, Ph.D.
Professor of Biomedical Engineering, Boston University

The men of experiment are like the ant, they only collect and use; the reasoners resemble spiders, who make cobwebs out of their own substance. But the bee takes the middle course: it gathers its material from the flowers of the garden and field, but transforms and digests it by a power of its own. Not unlike this is the true business of philosophy (science); for it neither relies solely or chiefly on the powers of the mind, nor does it take the matter which it gathers from natural history and mechanical experiments and lay up in the memory whole, as it finds it, but lays it up in the understanding altered and disgested. Therefore, from a closer and purer league between these two faculties, the experimental and the rational (such as has never been made), much may be hoped.

Sir Francis Bacon (Novum Organum)

Acknowledgments

Upon entering graduate school there have been many people who have helped me to grow, both academically and professionally. First and foremost is my research adviser, Paul Barbone. I would like to thank him for all his help, his patience and his encouragement. I am truly lucky to have been a part of the intellectually stimulating environment fostered by Paul over the last few years. I cannot imagine my graduate career being the positive experience it was without him. Now, I am fortunate enough to have him as a colleague and friend.

I would also like to thank Assad Oberai. Assad was another research adviser of mine. He too helped me through my graduate career with great patience and a zest for teaching. I am forever in his debt for all the discussions we have had and, hopefully, will have in the years to come.

To all the Biomechanical Imaging Group, whose members have come and gone over the years, thank you for the many thought provoking discussions which have helped me more times than I can remember. In particular I would like to thank Nachiket Gokhale and John Wanderer for sharing an office with me and with all their help with my many computer questions.

I would also like to thank the members of my Committee: Prof. Ken Lutchen for his help and guidance over the years, Prof. Irving Bigio for his thoughtful insights into my work, and Prof. Dimitrije Stamenovic was not only a member of my committee but also my academic adviser. I would like to thank him in particular for all his help throughout my time at BU.

A few labs at BU were also kind enough to allow me access to their facilities and equipment. First, thanks to the Klapperich Lab for their use of the DMA machine. Also thanks to the PAC Lab for allowing me a space with which to make and test my phantoms. Also, thank you for the use of and help with the laboratory equipment.

I need to also thank the collaborators of this project. Thanks to the Richard Moore and

Dan Kopans at MGH who were an integral part in the tomosynthesis experiments. Thanks for all your help and patience. A special thanks to Jeff Bamber who allowed me to visit his laboratory in Sutton. I learned a tremendous amount from the thoughtful discussions over teleconference and in person.

I would also like to thank all my friends and colleagues who I have met at BU, at the University of Rochester and those friends I have had since high school. You have all been an important support system for me and I have been very lucky to have you all in my life.

Lastly, I would like to thank my family. My sisters who have been my greatest strength. I could not have become the person I am today without you both and I love you very much. And of course my parents, who have been my role models and mentors for all my years. Thank you for showing me the importance of learning and teaching me to always strive for greatness. It is by your example that I have shaped my life and was able to accomplish what I have. Thank you and I love you both.

QUANTITATIVE THREE DIMENSIONAL ELASTICITY IMAGING

(Order No.   )

MICHAEL SCOTT RICHARDS

Boston University, College of Engineering, 2007

Major Professor: Paul E. Barbone, Ph.D., Professor of Aerospace and Mechanical Engineering

ABSTRACT

Neoplastic tissue is typically highly vascularized, contains abnormal concentrations of extracellular proteins (e.g. collagen, proteoglycans) and has a high interstitial fluid pressure compared to most normal tissues. These changes result in an overall stiffening typical of most solid tumors. Elasticity Imaging (EI) is a technique which uses imaging systems to measure relative tissue deformation and thus noninvasively infer its mechanical stiffness. Stiffness is recovered from measured deformation by using an appropriate mathematical model and solving an inverse problem. The integration of EI with existing imaging modalities can improve their diagnostic and research capabilities.

The aim of this work is to develop and evaluate techniques to image and quantify the mechanical properties of soft tissues in three dimensions ($3D$). To that end, this thesis presents and validates a method by which three dimensional ultrasound images can be used to image and quantify the shear modulus distribution of tissue mimicking phantoms. This work is presented to motivate and justify the use of this elasticity imaging technique in a clinical breast cancer screening study. The imaging methodologies discussed are intended to improve the specificity of mammography practices in general. During the development of these techniques, several issues concerning the accuracy and uniqueness of the result were elucidated.

Two new algorithms for $3D$ EI are designed and characterized in this thesis. The first

provides three dimensional motion estimates from ultrasound images of the deforming material. The novel features include finite element interpolation of the displacement field, inclusion of prior information and the ability to enforce physical constraints. The roles of regularization, mesh resolution and an incompressibility constraint on the accuracy of the measured deformation is quantified. The estimated signal to noise ratio of the measured displacement fields are approximately 1800, 21 and 41 for the axial, lateral and elevational components, respectively. The second algorithm recovers the shear elastic modulus distribution of the deforming material by efficiently solving the three dimensional inverse problem as an optimization problem. This method utilizes finite element interpolations, the adjoint method to evaluate the gradient and a quasi-Newton BFGS method for optimization. Its novel features include the use of the adjoint method and TVD regularization with piece-wise constant interpolation. A source of non-uniqueness in this inverse problem is identified theoretically, demonstrated computationally, explained physically and overcome practically. Both algorithms were test on ultrasound data of independently characterized tissue mimicking phantoms. The recovered elastic modulus was in all cases within 35% of the reference elastic contrast. Finally, the preliminary application of these techniques to tomosynthesis images showed the feasiblity of imaging an elastic inclusion.

Contents

List of Tables

List of Figures

List of Abbreviations

$1D$	. . . .	One Dimensional
$3D$	. . . .	Three Dimensional
BFGS	. . . .	Broyden Fletcher Goldfarb Shanno
CC	. . . .	Cross Correlation
CT	. . . .	Compterized Tomography
EI	. . . .	Elasticity Imaging
EIT	. . . .	Electrical Impedance Tomography
MGH	. . . .	Massachusetts General Hospital
MRI	. . . .	Magnetic Resonance Imaging
RF	. . . .	Radio Frequency
SFM	. . . .	Screen Film Mammography
SNR	. . . .	Signal to Noise Ratio
SRR	. . . .	Simultaneous Registration and Reconstruction
TDFT	. . . .	Time Dependent Fourier Transform
TVD	. . . .	Total Variation Diminishing

Chapter 1

Introduction

1.1   Specific Aims

Currently, screen film mammography is the most common imaging method used for screening and diagnostic mammography. Although this imaging technology has a high success rate for diagnosing cancer (up to 85%), it also suffers from a high number of false positives. To improve the specificity of mammography practices in general, adjunct imaging technologies are being developed to reveal new information for clinicians to base a diagnosis. One such imaging technology is elasticity imaging, which can image a tissue's stiffness. This technology would produce images of information which is already used in mammography screening during breast palpation examinations.

Biomechanical imaging is technique which measures tissue deformations, using existing imaging modalities, and then infers the underlying mechanical properties of the tissue from the measured deformations. Biomechanical imaging techniques, in general, vary depending on their method of imposing and measuring tissue motion, the model used to describe the tissue motion and the method with which the model parameters are inferred or quantified. Elasticity imaging can be considered a subset of biomechanical imaging in which the imaged tissue is modeled as an elastic solid.

The broad goal of this research project is to create a methodology which can image and quantify the shear elastic modulus of breast tissue while the breast is held in compression in a clinical mammography device.

The first specific aim of this work is to develop, implement and evaluate a method to accurately and noninvasively measure tissue deformations. This measurement technique

is developed in contrast to other displacement measurement techniques which sacrifice accuracy for computational speed. The method outlined in this thesis uses a finite element interpolation of the displacement field, has the ability to enforce physical constraints in the measurements and uses a Gauss-Newton optimization method to measure the displacements.

The second aim of this work is to develop, implement and evaluate an algorithm which can estimate the tissue's stiffness from those measured displacements. This algorithm will utilize a linear elastic model of breast tissue. Additionally, this method utilizes finite element interpolations, a quasi-Newton BFGS method for optimization and the adjoint method to evaluate the gradient. The uniqueness of the solution, given the available *a priori* data, is also investigated.

The final goal of this thesis work is to evaluate the ability of the developed measurement and inversion techniques to image and quantify shear modulus distribution using tissue mimicking phantoms for three dimensional ultrasound and tomosynthesis imaging.

1.2   Elasticity Imaging

Elasticity imaging is a technique which is rapidly gaining attention in the field of medical imaging (see e.g. reviews by Gao et al., 1996; Insana and Bamber, 2000; Ophir et al., 2001). Its development initiated within the context of cancer diagnosis and treatment and it is continuing to find broader biomedical applications. The idea underlying this technique is that traditional imaging systems are used to image a tissue's response to a mechanical stress. When a material is subject to stress, stiffer regions will tend to deform less than softer regions. Monitoring this deformation with an imaging system allows regions with contrasting mechanical properties to be identified and possibly quantified.

A key motivation behind this technique, as it applies to cancer diagnosis, is observed in the correlation between the pathology of tumors and their mechanical properties (Ophir et al., 1999). Many carcinomas tend to be stiffer than healthy tissue. This observation

underlies the reason that stiffness of tissue is routinely assessed qualitatively by palpation during physical exams. Elasticity imaging has the potential to add some unique clinical advantages, such as: provide quantitative assessment of stiffness in difficult to palpate regions, detect lesions that are unresolved in other approaches, and provide improved information related to the size and shape of tumors to improve the accuracy of tumor staging. Any of these would result in improvement in diagnosis and treatment of cancer.

There are three necessary components for elasticity imaging of soft tissue *in vivo*. The first of which is an imposed tissue deformation. There are several different types of deformations which have been commonly used in elasticity imaging. A quasi-static compressive deformation can be imposed externally on the tissue, which is suitable for breast and prostate imaging (Gao et al., 1996). The work discussed in this thesis will utilize the quasi-static compressive deformation, such as that which is imposed on breast tissue in typical mammographic procedures. Low frequency time-harmonic shear waves have been used for breast and liver imaging, in particular in conjunction with magnetic resonance imaging (MRI) (Sarvazyan et al., 1998; Sinkus et al., 2000; Chen et al., 1996). The radiation force produced by a focused ultrasound transducer also results in a controllable and measurable localized deformation (Nightingale et al., 2002; Fatemi et al., 2002; Bercoff et al., 2004). Such a capability may prove particularly useful in otherwise inaccessible organs. In some organs, the natural internal body motions such as cardiac rhythms can provide useful deformations for elasticity imaging (de Korte, 1999; Kolen et al., 2004).

The second required component for elasticity imaging is a method to image the deformation of the tissue. Some imaging systems already have the ability to measure relative velocities of tissues in real time (e.g. Doppler ultrasound, phase contrast MRI). These imaging systems have been used to image shear wave propagation in tissue (Taylor et al., 2000; Manduca et al., 2001; Fatemi and Greenleaf, 1998). Those imaging systems that do not directly measure velocities or displacements may still be used. In these cases the underlying tissue motion can be measured by registering image sequences of deforming tissue. Specifically, this means that by acquiring images of the same tissue in two distinct deforma-

tion states, one can measure image feature displacement as a direct method of measuring tissue displacement. Ultrasound is the most common imaging modality used to measure displacements in elasticity imaging. Many ultrasound elasticity imaging researchers apply a compressive force or strain to tissue in the direction of sound propagation and use the measured strain contrast to identify regions of low strain (Gao et al., 1996). The high frequency content of ultrasound in the direction of sound propagation lends itself to very accurate measurements of displacement and strain in that direction. Ultrasound is the primary imaging modality used for deformation measurements in this work.

The last required component for elasticity imaging is a method to infer the tissue mechanical properties from a measured displacement field. To do this, a mechanical model of soft tissue deformation is needed to mathematically relate measured displacements or strains to the tissue's material properties. The simplest and most commonly used model in elasticity imaging is the uniform uniaxial stress model (Ophir et al., 1991). In this model, tissue is treated as a one dimensional material in the direction of applied compression. This model neglects mechanical coupling between adjacent lines of material. Two dimensional linear elastic models, such as plane strain or plane stress, account for mechanical coupling within a plane of the tissue, such as an image slice, but of course neglects coupling out of that plane. Such models are often used because of the ubiquity of imaging systems that collect only planar data (Oberai et al., 2004; Kallel and Bertrand, 1996; Skovoroda et al., 1995; Doyley et al., 2000). Full three dimensional elastic models are rarer in the literature (Taylor et al., 2000; Sinkus et al., 2000; Houten et al., 2001). Of these, only Van Houten et al treats the full vector three dimensional elasticity equations. A three dimensional model used in conjunction with a measured three dimensional displacement vector field or fields accounts for coupling of tissue throughout its volume and thus more accurately represents three dimensional tissue structures. More complex models for tissue behavior may be chosen to account for dynamic behavior, tissue nonlinearity, viscosity, porosity, plasticity, etc. The complexity of the model will determine the extent of displacement information needed to correctly characterize the tissue's mechanical properties.

1.3   Breast Cancer Screening and Diagnosis

Elasticity imaging has a potentially large role to play in breast cancer management. Breast cancer is one of the most commonly occurring cancers among women and is the second leading cause of cancer related deaths for women (American Cancer Society, 2006d). Prevailing wisdom suggests that the sooner a cancer is detected, diagnosed and treated, the greater the chance of survival. Although breast cancer incidence has continued to increase by 2% per year, the death rates have been declining due at least in part to continually improved detection and screening regimens (American Cancer Society, 2006a).

In general, cancer develops when cells in the body begin to grow in an uncontrolled manner. Cancer usually forms as a tumor, or lump, in tissue, but not all tumors are cancerous. Fibrocystic adenomas or fibroadenomas are benign breast tumors of the glandular tissue, composed mostly of fibrous tissue. Cancerous lesions are typically described clinically as hard, non-elastic, turgid, poorly movable nodules (Anderson, 1977). It is in part because breast tumors are known to be hard that elasticity imaging is an attractive means to image them.

Regular breast self-examinations and clinical breast examinations facilitate the early detection of cancer. During a clinical breast screening examination, a physician will palpate or feel the breasts to locate any lumps or suspicious areas. If a lump is found, the physician then feels for its texture, size, firmness, mobility and relationship to the skin and chest muscles. A painless, hard mass that has irregular edges is more likely to be cancerous than not. There are some cancers, however, that are tender, soft and rounded (American Cancer Society, 2006d). Beginning at age forty, women are recommended to have a screening x-ray mammogram once per year in addition to physical exams (see Figure 1.1). These imaging examinations produce gray scale pictures which are related to the x-ray attenuation of the tissue. The size, shape and margins of a suspicious breast mass identified in an x-ray image are indicators of the likelihood of cancer (American Cancer

Society, 2006d).

If suspicious areas were found during a clinical breast exam or screening mammogram,
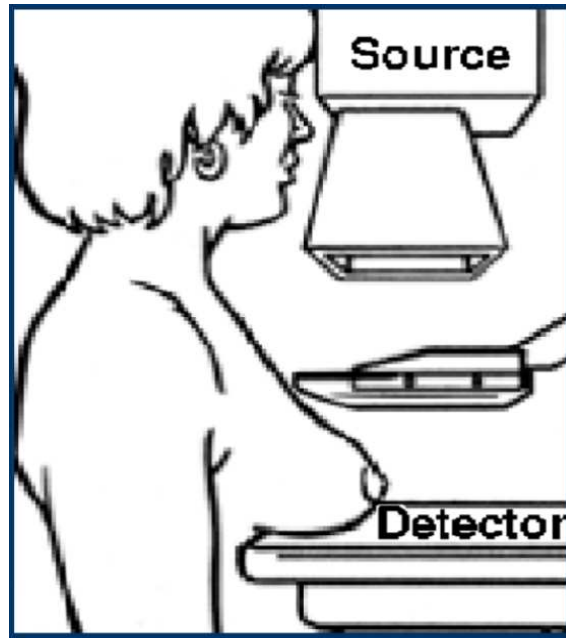
Figure 1.1: X-Ray mammography (Adapted from American Cancer Society, 2006c).

the patient is usually given a diagnostic x-ray mammogram. During this exam, more x-ray images of the breast are taken to carefully study the specific breast condition. These images are often difficult to interpret due to variability among patients, the physical nature of the imaging system or the difficulty in detecting certain types of breast cancers. Often physicians and radiologists use more than one imaging modality or technique to diagnose breast cancers (e.g. ultrasound). The only conclusive test for the presence of cancer is a biopsy: a removal of a portion of the suspicious tissue for investigation under a microscope. This procedure is considered invasive and is avoided whenever possible. Normally a biopsy is performed whenever a physical exam or image analysis cannot fully rule out the presence of cancer (American Cancer Society, 2006b).

It is common for younger (pre menopausal) women to have denser breast tissue. This dense tissue tends to obscure mammography images as well as increase the difficulty of locating breast masses by palpation. It is for this reason that mammography exams are not as strongly recommended for pre menopausal women, unless their medical history suggests they may be at high risk. Although, breast cancer is less common in younger women, the breast cancers which are diagnosed tend to be more aggressive.

Much of the focus in breast imaging research is centered around earlier detection and more accurate diagnostic tools. The current gold standard for breast cancer detection is screen-film mammography (SFM). While SFM is highly sensitive to breast tumors in post menopausal women, it is known to suffer from a large percentage of false positive diagnoses (Elmore et al., 1998; Fletcher and Elmore, 2003). In addition SFM is known to have poor sensitivity in pre menopausal women. Thus, some improvement to standard SFM is highly desirable. This is sought primarily in two directions: improving x-ray mammography itself, and developing new imaging systems to be used as an adjunct to x-ray mammography.

One important development in mammography is the advent of digital images, which can be created by digitizing a film mammogram or acquired directly using a digital x-ray detector. Digital images allow for shorter examination times, less storage space and computer aided detection or other computerized analysis (Simonetti et al., 1998). Furthermore, the availability of high resolution x-ray detectors has enabled the development of a novel imaging modality based on x-ray tomography. Digital x-ray tomosynthesis is an imaging methodology which can calculate three dimensional images of tissue volumes from a series of x-ray projections taken at different positions relative to a digital detector and the tissue being imaged. Tomosynthesis imaging systems are expected to increase the specificity of mammography, especially in radiographically dense tissue, due to its ability to resolve three dimensional image volumes (Niklason et al., 1997; Chen and Ning, 2003). The tomosynthesis system, like most standard mammography systems, holds the breast in compression with a transparent plate during image acquisition. This creates a method to impose a tissue deformation, thus lending itself to elasticity imaging.

MRI has also become a useful adjunct to mammography in high risk patients (Kriege et al., 2004) but concerns over costs, lack of standardized exam techniques and evaluations and poor specificity in preliminary data may limit MRI's overall usefulness (Smith et al., 2003).

Breast sonography is considered an indispensable adjunct to mammography. Although its usefulness in screening mammography is limited, it has been shown to differentiate cysts from solid masses with an accuracy approaching 100% (Jackson, 1990; Bassett and Kimme-Smith, 1991). It is also used to image radiographically dense breasts typical of younger women (Jackson, 1990; Jackson et al., 1993). Elasticity images, created from ultrasound, have been shown to result in relatively accurate and high resolution displacement measurements in the direction of sound propagation (Ophir et al., 1999). It has also been shown that ultrasound elasticity images, when used in conjunction with ultrasound images, improve the diagnostic sensitivity and specificity of ultrasound images alone (Garra et al., 1997; Bamber et al., 2002).

Smith et al., 2003 provides extensive list of other novel imaging technologies that are currently being developed and evaluated as potential adjuncts to conventional mammography. The more promising technologies include electrical impedance tomography (EIT) (e.g. Ross et al., 2003) and diffuse optical tomography (e.g. Boverman et al., 2005), besides of course elastography or elasticity imaging (e.g. Garra et al., 1997).

The work outlined in this thesis develops measurement techniques and inversion algorithms to create three dimensional (3D) elasticity images by processing images from another modality. The modalities under consideration in this work are three dimensional ultrasound and x-ray tomosynthesis imaging. The specific motivation of this work is to develop an elasticity imaging technique as an adjunct imaging technology to improve the specificity of mammography screening and diagnosis. These techniques will produce elastic modulus images which are perfectly aligned with the original ultrasound or tomosynthesis images. If the ultrasound images are taken with a spatial reference to the tomosynthesis or other mammography system, the shear modulus images, created from the ultrasound,

can easily be register with the x-ray images as well. It is expected that the viability of this technology will ultimately improve a physicians ability to diagnose and treat breast cancer as well as increase understanding of the relationship between the pathological changes of breast tissue and the changes observed in tissue's mechanical properties.

1.4   Thesis Overview

In this thesis, methods are developed, implemented, and validated to measure 3D deformations from pre and post deformation images. Similarly, an elastic modulus reconstruction algorithm is developed, implemented, and validated to recover the 3D elastic modulus distribution from the measured displacement. The inversion algorithms are based on three dimensional linear incompressible elasticity. The methods are extensively validated on 3D ultrasound data of tissue mimicking phantoms, and are also applied to 3D tomosynthesis image data.

The next chapter of this thesis will discuss the biomechanics of breast tissue. It gives an overview of the current available information on measured mechanical properties of breast tissue, what models best describe the tissue and the consequences of the model assumptions made in this thesis. The third chapter will discuss an image registration technique to accurately measure tissue deformations. It identifies the sources and relative magnitudes of noise in the displacement measurements. The fourth chapter will introduce the formulation of the inverse problem used to reconstruct the elastic modulus from the measured displacements. It will also discuss the relevant computational parameters used for these reconstructions. The fifth chapter will discuss the uniqueness of the reconstructed solutions. The sixth chapter presents an ultrasound imaging protocol and phantom study to characterize the accuracy of the reconstructed modulus distributions from ultrasound images. The seventh chapter introduces a tomosynthesis imaging protocol and discusses the feasibility of using these images to create elasticity images. The final chapter provides a discussions of results and draws conclusions from the work presented in this thesis.

Chapter 2

Biomechanics

2.1 Breast Tissue and Tissue Pathology

Typical breast tumors present as hard lesions or lumps in otherwise soft breast tissue. Tumor stiffness may be attributed to an elevated interstitial fluid pressure, an increased solid stress due to tissue proliferation or an extracellular matrix stiffening linked to fibrosis (Paszek et al., 1999). The observed differences in tissue stiffness, due to the altered physiology of malignancies, is the property which EI exploits to distinguish healthy tissue from diseased tumors.

Much of the research in the field of biomechanics of soft tissue has dealt with tissues whose primary function is mechanical (i.e. muscles, ligaments, tendons, cartilage, skin, and pulmonary or cardiovascular tissue). Breast tissue is outside of this category. Certain pathologies of breast tissue, however, result in significant changes to the tissue's mechanical properties (e.g. fibrosis, cysts, and localized malignancies). The practice of breast palpation, either in a self or clinical screening examination, is a qualitative assessment of the stress response of breast tissue at very low frequencies. Although the mechanical nature of the particular pathology does not directly affect any large scale mechanical function, the microscopic changes in the tissue's phenotype consequently lead to changes in macroscopic mechanical properties. This allows for the possibility of studying macroscopic tissue parameters, via elasticity imaging, as a means to monitor location and severity of these pathological tissues.

The breast organ contains several different types of soft tissues. Primarily it is composed of fibrous tissue, containing large amounts of collagen, elastin and the cells which

maintain these proteins. It also contains glandular or ductal tissue, which contains the lymphatic system and functional part of the breast. Lastly it contains adipose tissue, which is high in fat. The macroscopic mechanical properties of breast tissue are related primarily to the relative concentration of these tissue types (Krouskop et al., 1998). These relative proportions and distributions of different tissues comprising the breast vary from person to person, with age and, of course, with certain pathologies.

There are several possible mechanisms by which pathological conditions of breast tissue, in general, may lead to altered mechanical properties. One pathological condition, commonly associated with many breast and other soft tissue diseases, is that of fibrosis. Fibrosis is a condition which results in an increase in the relative density of the fibrous connective tissue, leading to a bulk stiffening in those areas. This can occur locally, forming stiff lesions, or over the organ as a whole. Another possible mechanism for changes in mechanical conditions is a local increase in the overall tissue density due to unregulated cell proliferation within a tumor and the resulting confinement from the surrounding tissue, like that seen in ductal carcinomas (Sarntinoranont et al., 2003). The increase in cell density creates residual "proliferation" stress within the tumor and surrounding tissue (Sarntinoranont et al., 2003). Another characteristic of tumor tissue is an abnormal interstitial fluid exchange. This results from the recruitment of blood vessels by a tumor, which it requires to support its increasing growth rate and metabolism. The fact that these blood vessels tend to be characteristically leaky and that the tumor lacks functional lymphatic vessels to drain the fluid may explain the increase in interstitial fluid pressure which has been measured *in vivo* for many tumors (Jain, 1999; Sarntinoranont et al., 2003; Nathanson and Nelson, 1994). The formation of calcifications in and around the tumor volume may also result in changes to the tissue's bulk mechanical properties.

One of the most commonly diagnosed benign tumors of the breast are fibroadenomas (Powell and Stelling, 1994). Fibroadenomas are often found to be palpable, firm, smooth nodules. They are often classified as rubbery, well-circumscribed and distinct from the surrounding tissue (Powell and Stelling, 1994). Fibroadenomas also often have calcifications

of varying degrees along their periphery. These tumors are marked by a local increase in fibrous tissue and very rarely contain adipose tissue (Powell and Stelling, 1994). The most common breast carcinoma is a ductal carcinoma, where ductal is a classification describing its histology rather than its location (Powell and Stelling, 1994). Ductal carcinoma *in situ* is a malignant tumor which has not yet invaded the surrounding tissues. It may be diagnosed as a palpable mass as well. Ductal carcinoma *in situ* is known to have an increased proliferation of malignant cells with atypical morphology. It is marked by regions of necrotic tissue which often form small, scattered calcifications within the tumor volume (Harris et al., 1996).

A recent study by Paszek et al., 1999 suggests that the stiffness of the stroma in a tumor region may have a mechanically regulated feedback on the cells in that stiff region which promotes a malignant phenotype. Integrins, which are responsible for the binding of cells to its extracellular matrix, function as a mechanotransductors which relay the forces in this matrix to the intracellular signaling pathways. It was found that cells whose extracellular matrix was stiffer would show more pronounced characteristics typical of metastatic cancer cells (Paszek et al., 1999).

The fact that disease alters a tissue's mechanical properties motivates the development of a tool to quantify mechanical properties *in vivo*. Quantification requires a mathematical model, which is described next.

2.2   Tissue Modeling

The constitutive relation defines the response of a material to applied loads. This relation depends directly on the internal composition of the specific material of interest. Breast tissue has a very complex structure with varying tissue types, concentrations and thermomechanical states. It has both solid and liquid components and it has the ability to remodel and change over time. A constitutive relation that accounts for all the phases of the material at all length scales, time dependent responses over many time scales, the ad-

dition and subtraction of material and any preexisting stress states would be impractically complicated. A more practical approach is to consider what observations or measurements are relevant to the anticipated loading conditions and then to use a simple constitutive relation which can capture the phenomena of interest. The following section describes and justifies the assumptions, conditions and constitutive model used for the elasticity imaging technique developed in this thesis. In particular breast tissue in model as a linear elastic, incompressible, single phase continuum.

The primary assumption of modeling tissue mechanics is that the material of interest may be treated as a continuum. Fung, 1993 defines a continuum based on some limiting value of a length scale used to represent a volume or area. Thus, the density at any point within the tissue, given a volume (ΔV) of tissue which has a certain mass (ΔM), can be defined as $\frac{\Delta M}{\Delta V}$ as the volume approaches this limiting length scale. One can similarly define the other material parameters, the stress and strain, and assume that these quantities will be continuous for all points within the tissue. For the purposes of elasticity imaging, these lengths scales are limited by the resolution of the displacement or strain observations, which is directly determined by the imaging system used. For the purposes of this work it is assumed breast tissue can be considered a continuum material for length scales on the order of hundreds of microns and larger, more than an order of magnitude greater than that of most microscopic histological features, including those of breast tissue.

In this work the breast tissue is modeled as a single phased, elastic solid material. Although it is true that breast tissue contains both liquid and solid phases, if there is a sufficient amount of time between the pre and post image acquisition, it can be expected that the resulting stress field is due only to the solid phase of the material imaged. That is, if the fluid in the breast is allowed to flow and equilibrate its contribution to the stress field, the resulting deformation is assumed to be due to the solid phase of the material alone.

Once it is established that breast tissue may be treated as a single phase continuum material, it must also be stipulated that it will obey the basic postulates of mechanics

(e.g. conservation of mass, momentum and energy). Therefore, prior to any assumptions concerning its constitutive behavior, breast tissue is expected to obey the law of the conservation of linear momentum. For slow motion of a single phase continuum, this may be expressed in Eulerian, or spatial, coordinates as:

$$\nabla \cdot \boldsymbol{\sigma} = \rho \frac{\partial^2 \mathbf{u}}{\partial t^2} \, . \tag{2.1}$$

In writing equation (2.1) $\boldsymbol{\sigma}$ is the Cauchy stress tensor, ρ is the density, $\mathbf{u}$ is the displacement vector field and all the body forces have been neglected.

To model the constitutive behavior of the breast tissue the equations for an isotropic, incompressible linear elastic solid will be used. The constitutive equations for an isotropic, compressible linear elastic solid are:

$$\boldsymbol{\sigma} = -p\mathbf{1} + 2\mu\boldsymbol{\epsilon} \tag{2.2}$$

$$\boldsymbol{\epsilon} = \frac{1}{2}(\nabla\mathbf{u} + (\nabla\mathbf{u})^{\mathbf{T}}) \tag{2.3}$$

$$-\frac{p}{\lambda} = \nabla \cdot \mathbf{u}. \tag{2.4}$$

Here, λ and μ are the Lamé parameters. The shear modulus of the tissue, μ, represents a material's resistance to a change in shape. The bulk modulus (k) of a material, represents a material's resistance to a change in volume. It can be expressed in terms of the Lamé parameters by the equation $k = \frac{2}{3}\mu + \lambda$. An incompressible material is one with an infinite resistance to volume change, a special case of a compressible material in which $k \rightarrow \infty$, thus $\lambda \rightarrow \infty$, but μ remains finite. In this case, equation (2.4) implies $\nabla \cdot \mathbf{u} \rightarrow 0$, but p remains finite. In this limit, p may be interpreted as the hydrostatic pressure distribution within the tissue.

Isotropy of the tissue follows from the assumption that the tissue structure within a continuum averaging volume is randomly oriented. This assumption is typically violated for tissues known to be associated with mechanical functions of the body (e.g. muscle,
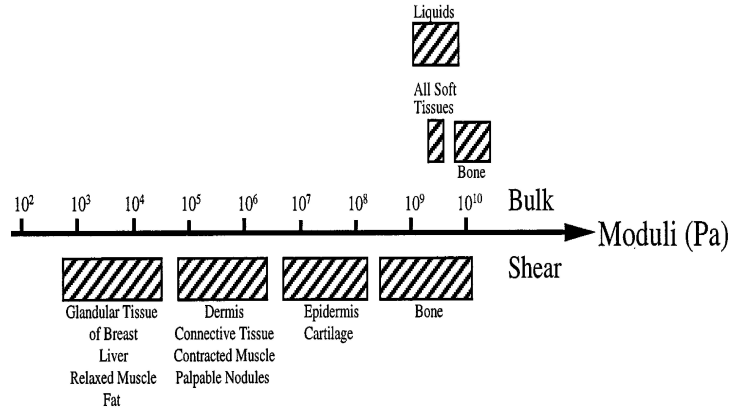
Figure 2.1: Tissue moduli distribution (Adapted from Sarvazyan et al., 1998)

bone, skin), particularly where tissue microstructure is strongly oriented. Isotropy is expected to be a more appropriate assumption for the microscopically unoriented glandular tissues of the breast, liver or prostate.

The assumption of tissue incompressibility of the tissue is justified, in part, on *in vitro* measurements which show the bulk modulus of soft tissue, including breast tissue, to be orders of magnitude higher than the shear modulus ($k \gg \mu$ and thus $\lambda \gg \mu$) (Sarvazyan et al., 1998). The cause of the incompressibility is the large fluid content within the these tissues (i.e. water). Figure 2.1 shows the relative distribution of breast tissue moduli as reported from the literature and collected by Sarvazyan et al., 1998. Also shown in figure 2.1 is the relative contrast in shear modulus between palpable nodules and healthy glandular tissue of the breast.

Breast tissue, like most soft tissues, cannot be fully characterized as linear elastic. As shown in Figure 2.2(a), the modulus of many breast tissues is expected to increase with increasing strain levels. Using a linear elastic model for tissue known to be non-linear may still yield relevant and repeatable results if the observed strains are small enough to assume that the stress-strain behavior is linear. Thus, given an initial stress or strain within the

(a)   (b)
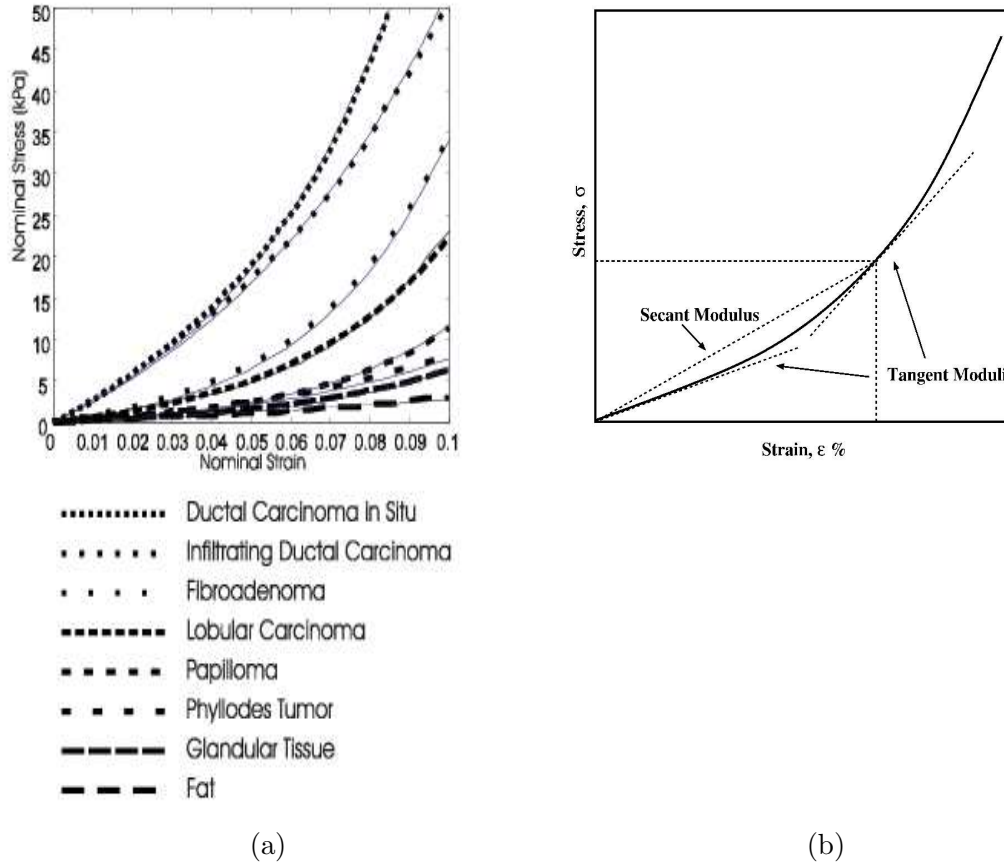
Figure 2.2: (a) Stress-strain curves for various breast tissue types measured *in vitro* (Adapted from Wellman et al., 1999) (b) Example plot showing secant and tangent moduli.

tissue, a linear model would yield the tangent modulus, or slope of the stress strain curve at that initial state (Figure 2.2(b)). The initial stress or strain of the tissue may affect the modulus measurements. Therefore it is important to be consistent in this regard when designing the experimental setup or imaging protocol. It may also be necessary, in certain instances, to measure larger strains and thus violate the linear stress-strain relationship. In this case one would effectively be measuring the secant modulus of the breast tissue (Figure 2.2(b)). If an imaging protocol is established to maintain a consistent initial state and magnitude of applied strain then the elastic modulus images are expected to recover repeatable contrast ratios between normal and healthy tissue types for clinically feasible

strain levels ($< 15\%$).

The assumption of linear elasticity also neglects any time dependent behavior of the tissue. In the breast images scenario considered here the tissue will be undergoing quasi-static deformations. Although the breast is expected to exhibit both viscoelastic or poroelastic behavior, the tissue will be imaged such that any relaxation can be assumed to have subsided. Thus only the elastic component of the tissue is being measured.

It shall also be assumed, due to the quasi-static imposed deformation, that the inertia of equation (2.1) can be neglected, and thus equations (2.1), (2.2) and the momentum equation become:

$$-\nabla p + 2\nabla \cdot (\mu \boldsymbol{\epsilon}) = 0. \tag{2.5}$$

Given a shear modulus distribution, equation (2.5) and the incompressibility constraint $\nabla \cdot \mathbf{u} = 0$ are sufficient to determine the pressure and displacement fields everywhere within a domain of interest, when the necessary boundary conditions are specified. It is these equations which will be used to calculate the shear modulus, given a distribution of displacements, within a region of interest of the tissue. Formulation of this inverse problem will be discussed in Chapter 4.

Table 2.1 shows the shear moduli or elastic moduli of both healthy and diseased breast tissues under a variety of loading conditions. These values were measured under the assumption that breast tissue is an isotropic and incompressible material. The effect of tissue nonlinearity can be seen by the dependence of the elastic modulus on the amount of applied precompression. A larger precompression leads to larger values for the measured tangent modulus. The appropriate amount of the precompression for EI will depend on the imaging modality used to measure tissue deformation. The effect of varying compression rates can also be seen in Table 2.1. For most of the breast tissue types measured by Krouskop et al., 1998, the values of the shear modulus increased with increasing frequency or loading rate, though only slightly. The sample to sample variability on the other hand is rather large. In most tissue types, this variability is about $30 - 50\%$ of the mean value. At this stage, it is not clear whether such heterogeneity can be expected within a single

Breast Tissue Type	Tissue Tangent Elastic Modulus (kPa)					
	5% precompression Loading frequency (Hz)			20% precompression Loading frequency (Hz)		
	0.1	1.0	4.0	0.1	1.0	4.0
Normal Fat (samples=8)	18 ± 7	19 ± 7	22 ± 12	20 ± 8	20 ± 6	24 ± 6
Normal glandular tissue (samples=31)	28 ± 14	33 ± 11	35 ± 14	48 ± 15	57 ± 19	66 ± 17
Fibrous tissue (samples=18)	96 ± 34	107 ± 31	116 ± 28	218 ± 87	232 ± 60	244 ± 85
Ductal carcinoma *in situ* (samples=23)	22 ± 8	25 ± 4	26 ± 5	291 ± 67	301 ± 58	307 ± 78
Invasive and infiltrating ductal carcinoma (samples=32)	106 ± 32	93 ± 33	112 ± 43	558 ± 180	490 ± 112	460 ± 178

Table 2.1: Elastic moduli of breast tissues measured *in vitro*. Adapted from Krouskop et al., 1998.

breast, or if the variation is primarily patient to patient variability.

For the quasi-static deformations proposed in this thesis, the deformation frequency is assumed to be much lower than $0.1\,Hz$. This table suggests that for a specific precompression and loading frequency, it is reasonable to expect repeatable measurements of shear modulus across patients and patient visits.

Table 2.1 shows the high contrast one could expect to see between tissues within the breast. For example, at low frequencies, there is more than a four to one contrast in shear modulus between a ductal carcinoma *in situ* and an infiltrating ductal carcinoma. This suggests it may also be possible, using elasticity imaging, to diagnose specific tumor types as well as possibly determine whether a tumor has infiltrated its surroundings.

Chapter 3

Displacement Estimation

3.1 Introduction

Fundamental to the process of elasticity imaging is the ability to measure physically accurate displacements from image sets of deforming tissues or phantoms. Measuring displacements from images is a subset of the problem of image registration. Image registration is the process of aligning two images (often of the same tissue). Medical image registration involves comparison of images from different modalities, different points in time or from different patients in order to compare image information, track disease progression or evaluate patient variability (Zitova and Flusser, 2003). In the case of elasticity imaging, the images compared are of tissue taken before and after some mechanical perturbation. The information desired is not the final registration but the intervening tissue motion.

This chapter presents a method for the characterization of imaging system noise and discusses how that noise can affect displacement estimations. It will then introduce a novel algorithm for measuring displacements from sets of images. It also evaluates the accuracy of the algorithm to measure displacements and identifies the possible sources of errors in the measurements.

The primary assumption, the validity of which dictates one's ability to accurately measure displacements from any imaging system, is that the deformation required to map one image to another results directly from the underlying tissue motion alone. That is, given an initial image of some tissue, $I_1(\mathbf{x})$, and an image after the tissue has undergone some mechanical perturbation, $I_2(\mathbf{x})$, the images can be related by:

$$I_1(\mathbf{x}) = I_2(\mathbf{x} + \mathbf{u}(\mathbf{x})). \qquad (3.1)$$

Here, the displacement field $\mathbf{u}(\mathbf{x})$ is the underlying tissue motion. In effect, this displacement field acts as a nonlinear scaling of the position vector defining the intensities of the original image. A graphical example of possible image pairs is shown in Figure 3.1. In this simple example a two dimensional image is acquired, the underlying tissue is then compressed and a second, post deformation image is acquired. It is clear from the one and two dimensional plots that the tissue displacement can be recovered from these image pairs by warping one image such that the features align. It is this image warping which is assumed to be equivalent to the tissue motion.

In equation (3.1), the functions $I_1(\mathbf{x})$ and $I_2(\mathbf{x})$ are spatial distributions of the scalar
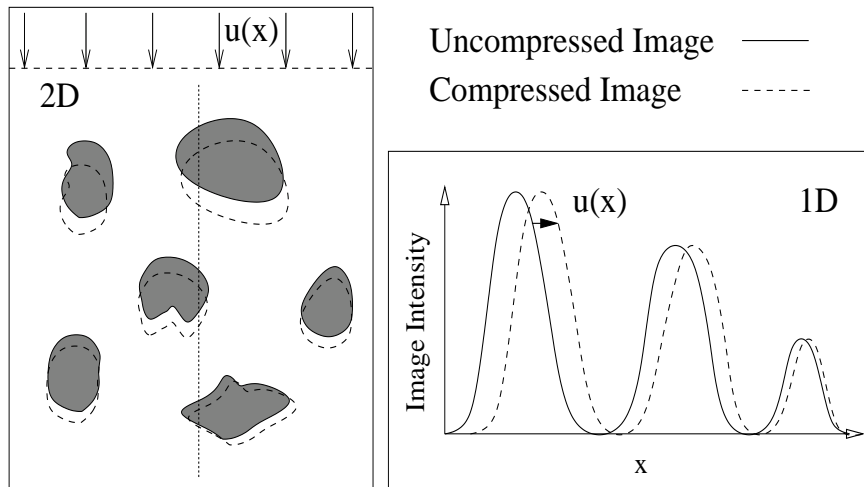
Figure 3.1: Example one and two dimensional pre and post deformation image pairs.

image intensities. These images are typically discrete and organized in multi-dimensional pixel matrices. However, if the voxel size can be identified, these matrices may be mapped to their actual positions in space, defined by the location $\mathbf{x}$. Then the value of the intensity at any location within the image can be determined by an interpolation of neighboring pixels.

In practice, equation (3.1) is never exactly satisfied. Typically, the point spread functions of imaging systems tend to blur tissue features to varying degrees. The resolution

of the displacement estimations will, therefore, be limited by the size of the point spread function as well as the spatial feature density. The presence of imaging system noise also violates this assumption. Assuming the noise is white and normally distributed, it can be shown that the magnitude of the signal to noise ratio will directly affect the variance of the displacement estimates. An explicit relation between the signal to noise ratio, as a function of frequency, and the accuracy and resolution of displacement measurements will be discussed in more detail in Section 3.2. Other types of image noise or image artifacts will also corrupt displacement calculations and should be avoided or filtered out prior to measuring displacements whenever possible.

One of the most common techniques for measuring displacements in ultrasound elastography is the cross correlation, block matching method (Ophir et al., 1991). The necessary assumption of this method is that the displacement is slowly varying and therefore can be approximated as constant in a relatively small subsection of the imaged domain. Under this assumption, equation (3.1) would reduce to:

$$I_1(\mathbf{x}) = I_2(\mathbf{x} + \mathbf{u}), \tag{3.2}$$

where $\mathbf{u}$ is no longer a function of x within that pair of image subsections. Time delay estimation techniques, such as normalized cross correlation (CC), are then used to calculate approximate displacements within these image windows. The distance from the origin to the maximum of the CC function (i.e. the spatial shift where the image signals are the most correlated) is the measured displacement for that image subsection. The dimensionality of the cross correlation will determine the dimensionality of the displacement vectors measured. Once a displacement estimate is found for this pair of image subsections, the process can be repeated for many similar subsections over the entire imaged domain. It is in this manner that a one or two dimensional displacement field is typically measured using two dimensional ultrasound images. This idea is similar in nature to that of the time dependent Fourier transform (TDFT) (Oppenheim and Schafer, 1999). Where the TDFT is an analysis of the time dependent changes in the frequency content of a single

signal, however, the CC block matching method compares the spatially dependent phase difference of two signals. The phase difference of the two signals corresponds to a spatial delay, or in this case, the spatial displacement. The resulting measured displacement field can be thought of as a discrete representation of a continuous displacement vector function.

One of the most important advantages of cross correlation based techniques is that they are computationally inexpensive calculations and are easily parallelized and implemented in hardware. These algorithms have been implemented in real time imaging modalities for one dimensional strain applications (Hall et al., 2003). In addition to being efficient, each individual cross correlation measurement is an optimization with a quasi-global search and as such does not require an initial guess. These techniques do have several drawbacks, however. Displacement estimations using these techniques tend to be very noisy when the signals in corresponding data windows become decorrelated. This can happen either because the local displacement gradients are large, or because the displacements themselves are too large. In the first case, when the local displacement gradients are too large, the assumption of constant displacement is violated and thus equation (3.2) is no longer valid. In the second case, the displacement is so large that the corresponding image windows no longer contain enough similar image information to calculate an accurate displacement. This image noise is further amplified when differentiating the displacement images to create strain images. These problems can be mitigated by "companding", a process of compressing and expanding the images locally to compensate for the decorrelation (Chaturvedi et al., 1998). Cross correlation techniques can also suffer from finding false peak correlations which can lead to unphysical displacement fields.

3.2   Imaging System Accuracy (The Cramér-Rao Bound)

The relative resolution of the CC algorithms depends on the size and spacing of the image matching blocks. The accuracy, or variance, of a delay estimator has a clear dependence on the window size of the CC as well as the frequency content of the image

intensity. The evaluation of the accuracy and resolution of a displacement calculation requires a method to relate the measurements to the original image characteristics. This relation can be made explicit through the Cramér-Rao bound (Walker and Trahey, 1995). The Cramér-Rao bound is the ultimate limit on the accuracy of a statistical estimator. For one dimensional delay estimation it is a statistical formulation for determining the lower limit of the delay variance based on the window size and the power spectra of the original signals. The calculation of the Cramér-Rao lower bound, as it applies to one dimensional displacement estimation, assumes the signals to be one dimensional and have a constant displacement in a given window (Walker and Trahey, 1995). The Cramér-Rao bound on the variance of the delay estimator is given by

$$\sigma_u^2(u - \hat{u}) = \frac{1}{W \int\limits_{-\infty}^{\infty} (2\pi f)^2 \dfrac{C_{I_1 I_2}(f)}{1 - C_{I_1 I_2}(f)} df}. \tag{3.3}$$

Here u is the true displacement, $\hat{u}$ is the estimated displacement, σ_u^2 is the variance of the displacement estimate, W is the window length used for the calculation and $C_{I_1 I_2}$ is the magnitude squared coherence function given as

$$C_{I_1 I_2}(f) = \left| \frac{G_{I_1 I_2}(f)}{\sqrt{G_{I_1 I_1}(f) G_{I_2 I_2}(f)}} \right|^2. \tag{3.4}$$

(Walker and Trahey, 1995) The G_{II}'s are the auto or cross power spectrum functions, depending on the subscripted signals, given by the equation:

$$G_{I_p I_q}(f) = \int\limits_{-\infty}^{\infty} \left(\int\limits_{-\infty}^{\infty} I_p(y) I_q(y + x) \, dy \right) e^{i2\pi f x} \, dx. \tag{3.5}$$

Equation (3.4) may be simplified in the case that the image signals take the form of

$$I_1(x) = s(x + u) + n_1(x) \tag{3.6}$$

$$\text{and} \quad I_2(x) = s(x) + n_2(x). \tag{3.7}$$

Here $s(x)$ is the underlying signal amplitude and $n_1(x)$ and $n_2(x)$ are uncorrelated white noise with equivalent power spectra. Under these conditions the coherence function reduces to

$$C_{I_1 I_2}(f) = \frac{1}{\left|1 + \frac{1}{SNR^2}\frac{\bar{G}_{nn}(f)}{G_{ss}(f)}\right|^2}. \tag{3.8}$$

SNR is the signal to noise ratio of the imaging system and the $\bar{G}_{ss}$ and $\bar{G}_{nn}$ are the normalized power spectra of the signal and noise, respectively. Their values are scaled such that their integrals are unity.

A bound on the variance in the strain estimates can be derived from the Cramér-Rao lower bound. If it is assumed that no new information is gained by overlapping windows of displacement information, a strain calculation would be the difference of displacement estimates spaced W pixels from each other ($\epsilon = \frac{u_1 - u_2}{W}$). The measurement of u_1 and u_2 are independent random variables with equal variances. Thus the estimated strain variance is

$$\sigma_\epsilon^2 = Var(\frac{u_1 - u_2}{W}) = \frac{Var(u_1) + Var(u_2)}{W^2} = \frac{2\sigma_u^2}{W^2}. \tag{3.9}$$

This analysis does not account for strain decorrelation (non-constant delays) or three dimensional CCs. However, an independent analysis of images in each direction may aid in experimental design and help determine algorithm parameters as well the limitations of the resulting calculations (resolution and signal to noise ratio).

3.3 The Cramér-Rao Bound For Two Imaging Systems

The calculation of the Cramér-Rao bound requires the power density spectra of the signal and noise in each direction of the image. To find these spectra, several images of the same material, with no deformation, were obtained for each modality (20 ultrasound images and 4 tomosynthesis images were compared)[1]. The mean of these images was used as the underlying signal ($s(x)$) and the individual images with the mean subtracted were

---

[1]See Chapter 6 for ultrasound image and Chapter 7 for tomosynthesis image acquisition techniques.
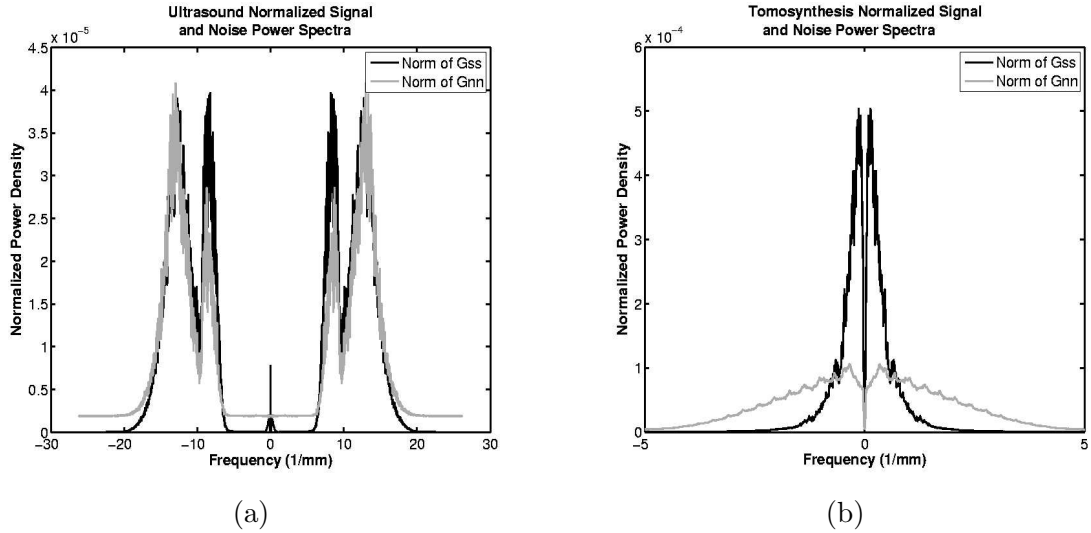
Figure 3.2: (a) Ultrasound power density. (b) Tomosynthesis power density.

used as the noise $(n(x))$. Directional Fourier transforms were used to find the power spectra. A comparison of the normalized signal and noise spectra for the axial direction of the ultrasound images and the high resolution directions of the tomosynthesis images is shown in Figure 3.2(a) and (b), respectively. The similarity of the noise and signal spectra in the ultrasound images may indicate a systematic error or movement in these images during the sequence acquisition. The results of the analysis, shown in Figure 3.3(a), compare the variance in the displacement estimates of the axial and lateral directions of the ultrasound image and either the (x) or (y) directions of the tomosynthesis image, which are assumed to have equal variances. Figure 3.3(b) shows the variance in the strain estimates of these same images and directions. The analysis was not performed for the elevation direction of the ultrasound images or the low resolution direction of the tomosynthesis images.

The variance computed for the lateral direction of the ultrasound image is larger than the axial variance for all window lengths. For the axial displacement estimates, if a resolution and thus a window size of about $5\,mm$ is desired for a strain image, the Cramér-Rao lower bound states that an applied strain of approximately 0.6% is needed to obtain a strain image signal to noise ratio of 100. This signal to noise ratio is well within the range
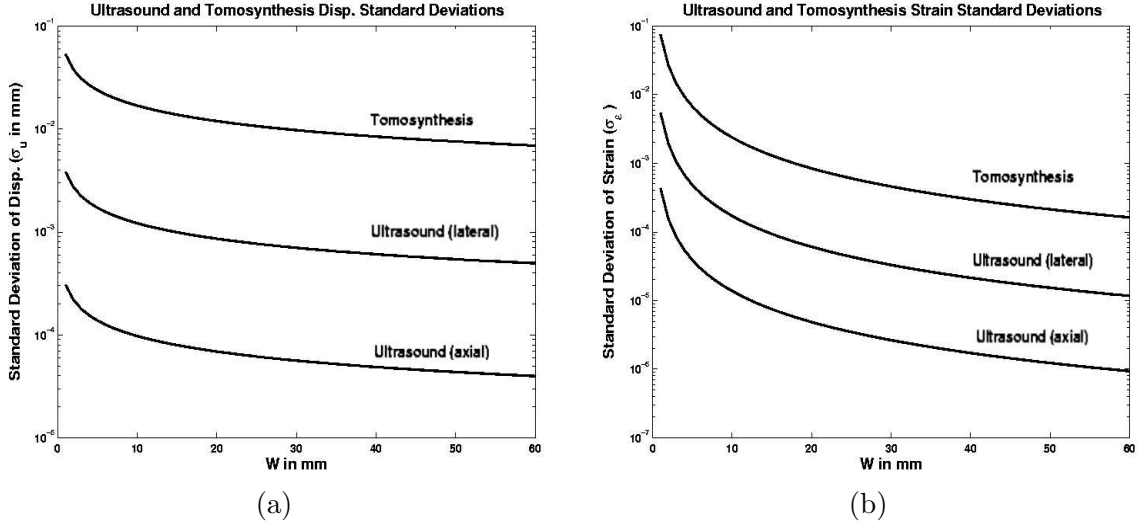
Figure 3.3: (a) Displacement Cramér-Rao lower bound. (b) Strain Cramér-Rao lower bound.

for strain signal to noise ratios seen in ultrasound elasticity images which yield noticable strain contrast (Ophir et al., 1999). The results for the tomosynthesis are not as promising as the ultrasound data. The variances are several orders of magnitude larger than either of the ultrasound variances. This is due in part to the lower SNR ratio of the tomosynthesis system and also the low spatial frequency range of the signal power of the tomosynthesis images. However, the equations defining the Cramér-Rao Lower Bound show that the variance in the displacement and strain estimates are independent of the applied strain. Thus, by applying higher strain values during compression experiments it may be possible to create images with a SNR within a reasonable range.

3.4   Image Registration Algorithm

Many of the researchers who study elastography or elasticity imaging use strain images for diagnostic purposes. These are created by taking the gradients of displacement fields measured with CC techniques. Despite these images being noisy, systems are now being sold which can create strain images in real time. In situations where further processing

of the measured displacement fields is required, as in model based parameter inversions for example, it is likely that a pseudo-real-time imaging system is no longer feasible. In such cases, it would be favorable to develop a more accurate displacement estimation technique and sacrifice the speed of cross correlation based algorithms. The image registration algorithm developed in this chapter is a gradient based, iterative optimization technique which minimizes the image intensity difference of the pre and post deformation images with respect to the measured displacement. Using an optimization technique such as this allows for the implementation of regularization and other constraints to decrease noise and avoid erroneous results. It also allows for a higher order interpolation of the underlying displacement functions. Using a linear interpolation of $\mathbf{u}(\mathbf{x})$, for instance, reduces the effect of image decorrelation in the displacement estimates.

The image registration algorithm used here is formulated as an optimization problem. Excluding any regularization or constraint terms, the functional minimized in each measurement is:

$$\pi[\mathbf{u}(\mathbf{x})] = \frac{1}{2} \int_\Omega \left(I_1(\mathbf{x}) - I_2(\mathbf{x} + \mathbf{u}(\mathbf{x})) \right)^2 d\Omega. \tag{3.10}$$

In this functional, I_1 and I_2 are the pre and post deformation images, respectively, and Ω is the spatial domain of interest. For Gaussian distributed image noise, minimizing this functional gives the maximum likelihood estimate for $\mathbf{u}$ (Press et al., 2002). For the following equations in this section the $\mathbf{x}$ dependence is implied for all images, image gradients, displacements and variants of displacements (i.e. $\mathbf{u} = \mathbf{u}(\mathbf{x})$ and $I_1(\mathbf{u}) = I_1(\mathbf{x} + \mathbf{u})$). The minimization of this functional by Gauss-Newton's method requires both the first derivative and an approximation to the second derivative of the functional $\pi[\mathbf{u}]$ with respect to the function $\mathbf{u}$.

The first derivative of $\pi(\mathbf{u})$ is found using the functional derivative, defined by the equations:

$$D_{\mathbf{u}}\pi \cdot \mathbf{w} = \left. \frac{d}{d\varepsilon} \right|_{\varepsilon \to 0} \pi[\mathbf{u} + \varepsilon\mathbf{w}], \tag{3.11}$$

where $D_{\mathbf{u}}\pi$ is the gradient of π with respect to $\mathbf{u}$. In these equations the function $\mathbf{w}(\mathbf{x})$ is an arbitrary admissible variation of $\mathbf{u}$ such that for all values of ε, $\mathbf{u} + \varepsilon\mathbf{w}$ satisfies all the boundary conditions that $\mathbf{u}$ must satisfy. Using equations (3.10) in the right hand side of equation (3.11) gives:

$$D_{\mathbf{u}}\pi \cdot \mathbf{w} = -\int_{\Omega} (I_1 - I_2(\mathbf{u})) \, \nabla I_2(\mathbf{u}) \cdot \mathbf{w} \, d\Omega. \tag{3.12}$$

If a minimum of the functional π exists, then equation (3.12) is equal to zero at that minimum. Thus equation (3.12) becomes:

$$\int_{\Omega} \mathbf{w} \cdot \nabla I_2(\mathbf{u}) \, (I_1 - I_2(\mathbf{u})) \, d\Omega = 0. \tag{3.13}$$

Equation (3.13) is solved iteratively. To that end, let $\mathbf{u}_v$ be the current guess of $\mathbf{u}$ and let $\delta\mathbf{u}$ be the update to $\mathbf{u}_v$ such that:

$$\mathbf{u}_{v+1} = \mathbf{u}_v + \delta\mathbf{u}. \tag{3.14}$$

Then substituting equation (3.14) into equation (3.13) and expanding with a first order Taylor series gives:

$$\int_{\Omega} \mathbf{w} \cdot (\nabla I_2(\mathbf{u}_v) + \nabla\nabla I_2(\mathbf{u}_v) \cdot \delta\mathbf{u}) \, (I_1 - I_2(\mathbf{u}_v) - \nabla I_2(\mathbf{u}_v) \cdot \delta\mathbf{u}) \, d\Omega = O(\delta\mathbf{u}^2). \tag{3.15}$$

To simplify this equation, terms of $O(\|\delta\mathbf{u}\|^2)$ will be neglected. It is assumed that when $\mathbf{u}_v$ is sufficiently close to $\mathbf{u}$, $(I_2(\mathbf{x}) - I_1(\mathbf{x} + \mathbf{u}_v)) \approx O(\|\delta\mathbf{u}\|)$. Then equation (3.15) reduces to

$$\int_{\Omega} \mathbf{w} \cdot (\nabla I_2(\mathbf{u}_v) \otimes \nabla I_2(\mathbf{u}_v)) \, \delta\mathbf{u} \, d\Omega = \int_{\Omega} \mathbf{w} \cdot \nabla I_2(\mathbf{u}_v) \, (I_1 - I_2(\mathbf{u}_v)) \, d\Omega. \tag{3.16}$$

This equation is used to solve for $\delta\mathbf{u}$ at each iteration to create a new guess of $\mathbf{u}_v$ via (3.14).

To solve equation (3.16) it is necessary to discretize the functions $\mathbf{u}$ and its variants. These functions are approximated using the following finite element, linear interpolation

function expansions:

$$\mathbf{u}_v^h = \sum_{A=1}^{N} \sum_{i=1}^{nsd} N_A(\mathbf{x}) \, f_{Ai} \, \mathbf{e}_i \qquad (3.17)$$

$$\mathbf{w}^h = \sum_{A=1}^{N} \sum_{i=1}^{nsd} N_A(\mathbf{x}) \, c_{Ai} \, \mathbf{e}_i \qquad (3.18)$$

$$\delta\mathbf{u}^h = \sum_{A=1}^{N} \sum_{i=1}^{nsd} N_A(\mathbf{x}) \, d_{Ai} \, \mathbf{e}_i. \qquad (3.19)$$

Here N is the total number of nodes in the discretization and nsd is the number of spatial dimensions. The N_A's are the linear shape functions defined at each nodal value A and the f_{Ai}'s, c_{Ai}'s and d_{Ai}'s are the nodal values for the discretized vector functions $\mathbf{u}_v$, $\mathbf{w}$ and $\delta\mathbf{u}$, respectively. In these equations h is used to denote the approximation of the functions $\mathbf{u}_v$, $\mathbf{w}$ and $\delta\mathbf{u}$ with functions in finite dimensional space. This algorithm calculates the coefficients d_{Bj} at each iteration by solving the discrete counterpart to equation (3.16):

$$\left[\int_{\Omega} N_A(I_{2,i}(\mathbf{u}_v^h))(I_{2,j}(\mathbf{u}_v^h)) \, N_B \, d\Omega \right] d_{Bj} = \int_{\Omega} N_A \, I_{2,i}(\mathbf{u}_v^h) \, (I_1 - I_2(\mathbf{u}_v^h)) \, d\Omega \,. \qquad (3.20)$$

The above equation can be represented by a matrix equation with the form:

$$\mathbf{M}_{kq} \, \mathbf{d}_q = \mathbf{r}_k \qquad (3.21)$$

where,

$$k = \sum_{A=1}^{N} \sum_{i=1}^{nsd} nsd \times (A - 1) + i \qquad (3.22)$$

and

$$q = \sum_{B=1}^{N} \sum_{j=1}^{nsd} nsd \times (B - 1) + j. \qquad (3.23)$$

In equation (3.21) the square matrix $\mathbf{M}$ and vector $\mathbf{r}$ are known quantities, and the vector $\mathbf{d}$ is the sought unknown vector.

Each iteration of the above algorithm requires the building of the left hand side matrix $\mathbf{M}(\text{size} = (nsd \times N)^2)$ and the right hand side vector $\mathbf{r}(\text{size} = (nsd \times N))$. To build this

matrix and vector, integration of equation (3.20) over the measurement domain is required. This function is integrated using a three dimensional midpoint rule where the number of integration points is approximately equivalent to that of the number of image pixels. The images are interpolated at each integration point using cubic Lagrange polynomials. The integration of equation (3.20) is divided into element sub domains, and integrated over each individual element separately. The process of calculating each element contribution and the subsequent matrix and vector builds was parallelized to improve the speed of the iterations (OpenMP). After the matrix and vectors are created, a parallelized linear solver is used to find the vector of nodal values of $\delta \mathbf{u}^h$ (PARDISO). The iterations are terminated when the displacements have converged (i.e. when the normalized L^2 norm of the images has fallen below some threshold value).

3.4.1 Regularization

When defining the image registration problem in the above form, the displacement estimates may still result in erroneous measurements in areas of high noise. This formulation, however, allows for the implementation of regularization. To limit the effect of noise it is often assumed that the solution, in this case $\mathbf{u}(\mathbf{x})$, is smooth (i.e. has a bounded H^1 norm) and thus another term is added to the functional which penalizes noise in the measurement. There are different types of regularization typically used in inverse problems. The implementation of the above algorithm uses an H^1 semi-norm regularization to penalize large gradients in $\mathbf{u}(\mathbf{x})$. The regularization is added as a term in the functional π:

$$\pi[\mathbf{u}(\mathbf{x})] = \frac{1}{2} \int_\Omega (I_1(\mathbf{x}) - I_2(\mathbf{x} + \mathbf{u}(\mathbf{x})))^2 \, d\Omega + \frac{1}{2} \int_\Omega \alpha_1 (\nabla \mathbf{u}(\mathbf{x}) : \nabla \mathbf{u}(\mathbf{x})) \, d\Omega. \qquad (3.24)$$

The assumption of small gradients of $\mathbf{u}(\mathbf{x})$ is expected to be an accurate assumption in this case because the set of all possible displacement fields resulting from the deformation of a continuous medium with any material parameter distribution is inherently smoother than the underlying parameter distribution.

The amount or strength of the regularization will depend on the value of the scalar α_1. To determine the appropriate choice for α_1, consider the assumptions made in Section 3.1 and the three dimensional extensions of equations (3.6) and (3.7),

$$I_1(\mathbf{x}) = s(\mathbf{x} + \mathbf{u}(\mathbf{x})) + n_1(\mathbf{x}) \tag{3.25}$$

$$\text{and} \quad I_2(x) = s(\mathbf{x}) + n_2(\mathbf{x}). \tag{3.26}$$

Substituting these equations into equation (3.10) gives

$$\pi[\mathbf{u}(\mathbf{x})] = \frac{1}{2} \int_\Omega (n_1(\mathbf{x}) - n_2(\mathbf{x} + \mathbf{u}(\mathbf{x})))^2 \, d\Omega. \tag{3.27}$$

If it is further assumed that the non-linear stretching of the white noise function n_2 does not significantly change its power spectrum, then the magnitude of π in equation (3.24) at the exact $\mathbf{u}(\mathbf{x})$ is equivalent to the integrated noise power of the images. This value is a measurable quantity for any imaging system and is inversely proportional to the system's SNR. According to the theory of residues due to Morozov, α_1 should be chosen such that the value of the regularization functional in equation (3.10), at the exact value $\mathbf{u}(\mathbf{x})$, is approximately equal to the integrated noise power of the images (Oberai et al., 2004). That is:

$$\frac{1}{2} \int_\Omega \alpha_1 (\nabla \mathbf{u}(\mathbf{x}) : \nabla \mathbf{u}(\mathbf{x})) \, d\Omega \approx \frac{1}{2} \int_\Omega (I_1(\mathbf{x}) - I_2(\mathbf{x} + \mathbf{u}(\mathbf{x})))^2 \, d\Omega$$

$$= \frac{1}{2} \int_\Omega (n_1(\mathbf{x}) - n_2(\mathbf{x} + \mathbf{u}(\mathbf{x})))^2 \, d\Omega. \tag{3.28}$$

One of the drawbacks of regularization as a method for smoothing images is that the added term can introduce certain artifacts in the resulting $\mathbf{u}^h(\mathbf{x})$, particularly when α_1 is large. The introduction of these artifacts into the measured displacement limits the algorithm's ability to reach a minimum such that the residual is equal to the noise power. Thus it is necessary to run simulated examples, with known displacements, to determine the α_1 for which the most accurate $\mathbf{u}(\mathbf{x})$ result is measured (See Section 3.4.3).

3.4.2 Incompressibility

One advantage of capturing a full three dimensional data set is that the a priori knowledge that breast tissue is an incompressible material may be used to further constrain the displacements measured from these image pairs. To implement this, another term is added to the functional of equation (3.24) which penalizes non zero values of the divergence of the displacement. The three term functional thus becomes:

$$\pi[\mathbf{u}(\mathbf{x})] = \int_{\Omega} \frac{1}{2}(I_1(\mathbf{x}) - I_2(\mathbf{x} + \mathbf{u}(\mathbf{x})))^2 + \frac{\alpha_1}{2}(\nabla \mathbf{u}(\mathbf{x}) : \nabla \mathbf{u}(\mathbf{x})) + \frac{\alpha_2}{2}(\nabla \cdot \mathbf{u}(\mathbf{x}))^2 \, d\Omega. \quad (3.29)$$

Again, the relative strength of the incompressibility term will be determined by the magnitude of the α_2 parameter. This term, however, is not appropriately considered a regularization term. Rather, it is a constraint that is being enforced via a penalty. Ideally and naively, therefore, α_2 could be taken to infinity. In practice however, α_2 is determined as the highest value after which no improvement in the measured $\mathbf{u}(\mathbf{x})$ is present. An example of the effect of increasing α_2 will be illustrated in Section 3.4.3.

One of the important considerations when dealing with incompressible materials within the context of finite element methods is that of mesh locking (Hughes, 1999). This phenomenon affects finite element approximations of incompressible and nearly incompressible materials by overly confining the possible outcomes of the resulting displacements fields. To alleviate the tendency of mesh locking in this algorithm, selective reduced integration is used in the computation of this functional term (Hughes, 1999). Selective reduced integration is a method which reduces the integration of the $\nabla \cdot \mathbf{u}$ term to first order.

3.4.3 Parameter Values

To characterize the effect of varying the algorithm's parameters on the resulting measurements, a series of tests was performed to register images with a known applied dis-

placement field. Five different images were extracted from measured radio frequency (RF) ultrasound images taken with the same ultrasound scanner and of the same phantom. The images were taken in different regions of the phantom such that the image information is uncorrelated, but the resolution is the same and the frequency power spectrum is approximately equal. Then the images were artificially deformed to create a second, pre deformation image for each. The assumed deformation field corresponds to an unconfined compression test, with slip boundaries, of a homogeneous block of incompressible linear elastic material at a strain level of 4%. Thus the displacement field is linear in each direction and volume conserving. Then, on each of these five image pairs, a displacement was measured using the image registration algorithm with five different values of α_1, four different values of α_2 and five different finite element mesh sizes. The values of these parameters span above and below the values typically used in practice for the phantom displacement measurements discussed in this thesis. The mesh sizes represent the number of elements spanning an equivalent volume in each test, thus an increasing number of elements implies a higher displacement resolution. No artificial noise is added to the images, however, the images are rounded to a 16 bit integer to simulate digitization.

Tables 3.1-3.15 show the L^2 norms of the measured displacement field. Each displacement direction is considered a scalar function with its own distinct norm value. The values of the norms are defined as follows:

$$\text{Total Error:} \qquad n_i = \frac{\sqrt{\frac{1}{5}\sum_{j=1}^{5}\int_\Omega (u_i^{ex} - u_i^j)^2\, d\Omega}}{\sqrt{\int_\Omega (u_i^{ex})^2\, d\Omega}} \qquad \text{for} \quad i = x, y \, or \, z \qquad (3.30)$$

$$\text{Precision Error:} \qquad \bar{n}_i = \frac{\sqrt{\frac{1}{5}\sum_{j=1}^{5}\int_\Omega (u_i^j - \bar{u}_i)^2\, d\Omega}}{\sqrt{\int_\Omega (u_i^{ex})^2\, d\Omega}} \qquad \text{for} \quad i = x, y \, or \, z \qquad (3.31)$$

$$\text{Bias Error:} \qquad \hat{n}_i = \frac{\sqrt{\int_\Omega (u_i^{ex} - \bar{u}_i)^2\, d\Omega}}{\sqrt{\int_\Omega (u_i^{ex})^2\, d\Omega}} \qquad \text{for} \quad i = x, y \, or \, z. \qquad (3.32)$$

Here $\bar{u}$ is the average displacement of the measurements made from the five image pairs and u^{ex} is the exact displacement with which the images were deformed prior to measurement.

α_2 α_1	0	1×10^{10}	1×10^{20}	1×10^{30}
0	$n_x = 0.1095$ $n_y = 0.0003965$ $n_z = 0.06984$	$n_x = 0.05345$ $n_y = 0.0003702$ $n_z = 0.03784$	$n_x = 0.07022$ $n_y = 0.0004048$ $n_z = 0.04466$	$n_x = 0.07022$ $n_y = 0.0004048$ $n_z = 0.04466$
1×10^6	$n_x = 0.1092$ $n_y = 0.000396$ $n_z = 0.06964$	$n_x = 0.0532$ $n_y = 0.0003696$ $n_z = 0.03773$	$n_x = 0.06995$ $n_y = 0.0004041$ $n_z = 0.04454$	$n_x = 0.06995$ $n_y = 0.0004041$ $n_z = 0.04454$
1×10^8	$n_x = 0.09854$ $n_y = 0.0003705$ $n_z = 0.06541$	$n_x = 0.04697$ $n_y = 0.0003315$ $n_z = 0.03266$	$n_x = 0.0608$ $n_y = 0.000359$ $n_z = 0.03798$	$n_x = 0.0608$ $n_y = 0.000359$ $n_z = 0.03798$
1×10^9	$n_x = 0.2448$ $n_y = 0.0009459$ $n_z = 0.1641$	$n_x = 0.07876$ $n_y = 0.0008669$ $n_z = 0.0439$	$n_x = 0.05427$ $n_y = 0.0008474$ $n_z = 0.02984$	$n_x = 0.05427$ $n_y = 0.0008474$ $n_z = 0.02984$
1×10^{10}	$n_x = 0.8413$ $n_y = 0.006943$ $n_z = 0.681$	$n_x = 0.3857$ $n_y = 0.007786$ $n_z = 0.2756$	$n_x = 0.07187$ $n_y = 0.007312$ $n_z = 0.05591$	$n_x = 0.07187$ $n_y = 0.007312$ $n_z = 0.05591$

Table 3.1: Total Error, n_i for a finite element mesh with dimensions $5 \times 5 \times 5$.

α_2 α_1	0	1×10^{10}	1×10^{20}	1×10^{30}
0	$\bar{n}_x = 0.04406$ $\bar{n}_y = 0.0002606$ $\bar{n}_z = 0.03736$	$\bar{n}_x = 0.03002$ $\bar{n}_y = 0.0001841$ $\bar{n}_z = 0.02103$	$\bar{n}_x = 0.03301$ $\bar{n}_y = 0.0002104$ $\bar{n}_z = 0.02394$	$\bar{n}_x = 0.03301$ $\bar{n}_y = 0.0002104$ $\bar{n}_z = 0.02394$
1×10^6	$\bar{n}_x = 0.04371$ $\bar{n}_y = 0.0002602$ $\bar{n}_z = 0.03721$	$\bar{n}_x = 0.02973$ $\bar{n}_y = 0.0001838$ $\bar{n}_z = 0.02092$	$\bar{n}_x = 0.03264$ $\bar{n}_y = 0.0002101$ $\bar{n}_z = 0.02381$	$\bar{n}_x = 0.03265$ $\bar{n}_y = 0.0002101$ $\bar{n}_z = 0.02381$
1×10^8	$\bar{n}_x = 0.03532$ $\bar{n}_y = 0.0002432$ $\bar{n}_z = 0.03164$	$\bar{n}_x = 0.02154$ $\bar{n}_y = 0.0001759$ $\bar{n}_z = 0.016$	$\bar{n}_x = 0.02172$ $\bar{n}_y = 0.0001975$ $\bar{n}_z = 0.01776$	$\bar{n}_x = 0.02172$ $\bar{n}_y = 0.0001975$ $\bar{n}_z = 0.01776$
1×10^9	$\bar{n}_x = 0.05853$ $\bar{n}_y = 0.0006546$ $\bar{n}_z = 0.04775$	$\bar{n}_x = 0.01863$ $\bar{n}_y = 0.0005216$ $\bar{n}_z = 0.01409$	$\bar{n}_x = 0.01342$ $\bar{n}_y = 0.0005107$ $\bar{n}_z = 0.011$	$\bar{n}_x = 0.01342$ $\bar{n}_y = 0.0005107$ $\bar{n}_z = 0.011$
1×10^{10}	$\bar{n}_x = 0.07599$ $\bar{n}_y = 0.003983$ $\bar{n}_z = 0.1341$	$\bar{n}_x = 0.1116$ $\bar{n}_y = 0.004135$ $\bar{n}_z = 0.04022$	$\bar{n}_x = 0.01844$ $\bar{n}_y = 0.003735$ $\bar{n}_z = 0.01574$	$\bar{n}_x = 0.01844$ $\bar{n}_y = 0.003735$ $\bar{n}_z = 0.01574$

Table 3.2: Precision Error, $\bar{n}_i$ for a finite element mesh with dimensions $5 \times 5 \times 5$.

α_2 \ α_1	0	1×10^{10}	1×10^{20}	1×10^{30}
0	$\hat{n}_x = 0.1003$ $\hat{n}_y = 0.0002988$ $\hat{n}_z = 0.059$	$\hat{n}_x = 0.04422$ $\hat{n}_y = 0.0003212$ $\hat{n}_z = 0.03146$	$\hat{n}_x = 0.06198$ $\hat{n}_y = 0.0003458$ $\hat{n}_z = 0.03771$	$\hat{n}_x = 0.06198$ $\hat{n}_y = 0.0003458$ $\hat{n}_z = 0.03771$
1×10^6	$\hat{n}_x = 0.1001$ $\hat{n}_y = 0.0002985$ $\hat{n}_z = 0.05887$	$\hat{n}_x = 0.04412$ $\hat{n}_y = 0.0003206$ $\hat{n}_z = 0.0314$	$\hat{n}_x = 0.06186$ $\hat{n}_y = 0.0003452$ $\hat{n}_z = 0.03764$	$\hat{n}_x = 0.06186$ $\hat{n}_y = 0.0003452$ $\hat{n}_z = 0.03764$
1×10^8	$\hat{n}_x = 0.092$ $\hat{n}_y = 0.0002796$ $\hat{n}_z = 0.05725$	$\hat{n}_x = 0.04174$ $\hat{n}_y = 0.000281$ $\hat{n}_z = 0.02848$	$\hat{n}_x = 0.05678$ $\hat{n}_y = 0.0002997$ $\hat{n}_z = 0.03357$	$\hat{n}_x = 0.05678$ $\hat{n}_y = 0.0002997$ $\hat{n}_z = 0.03357$
1×10^9	$\hat{n}_x = 0.2377$ $\hat{n}_y = 0.0006828$ $\hat{n}_z = 0.157$	$\hat{n}_x = 0.07652$ $\hat{n}_y = 0.0006925$ $\hat{n}_z = 0.04158$	$\hat{n}_x = 0.05259$ $\hat{n}_y = 0.0006762$ $\hat{n}_z = 0.02774$	$\hat{n}_x = 0.05259$ $\hat{n}_y = 0.0006762$ $\hat{n}_z = 0.02774$
1×10^{10}	$\hat{n}_x = 0.8379$ $\hat{n}_y = 0.005687$ $\hat{n}_z = 0.6677$	$\hat{n}_x = 0.3692$ $\hat{n}_y = 0.006597$ $\hat{n}_z = 0.2726$	$\hat{n}_x = 0.06947$ $\hat{n}_y = 0.006286$ $\hat{n}_z = 0.05365$	$\hat{n}_x = 0.06947$ $\hat{n}_y = 0.006286$ $\hat{n}_z = 0.05365$

Table 3.3: Bias Error, $\hat{n}_i$ for a finite element mesh with dimensions $5 \times 5 \times 5$.

α_2 \ α_1	0	1×10^{10}	1×10^{20}	1×10^{30}
0	$n_x = 0.1212$ $n_y = 0.00052$ $n_z = 0.07861$	$n_x = 0.06718$ $n_y = 0.0004838$ $n_z = 0.04492$	$n_x = 0.08193$ $n_y = 0.0005273$ $n_z = 0.05186$	$n_x = 0.08193$ $n_y = 0.0005273$ $n_z = 0.05186$
1×10^6	$n_x = 0.1193$ $n_y = 0.0005179$ $n_z = 0.07776$	$n_x = 0.06494$ $n_y = 0.0004815$ $n_z = 0.04406$	$n_x = 0.07958$ $n_y = 0.0005248$ $n_z = 0.05092$	$n_x = 0.07959$ $n_y = 0.0005248$ $n_z = 0.05092$
1×10^8	$n_x = 0.09248$ $n_y = 0.00047$ $n_z = 0.06412$	$n_x = 0.04583$ $n_y = 0.0004182$ $n_z = 0.03235$	$n_x = 0.05865$ $n_y = 0.0004526$ $n_z = 0.03765$	$n_x = 0.05865$ $n_y = 0.0004526$ $n_z = 0.03765$
1×10^9	$n_x = 0.2317$ $n_y = 0.001458$ $n_z = 0.1506$	$n_x = 0.07712$ $n_y = 0.001334$ $n_z = 0.04313$	$n_x = 0.0541$ $n_y = 0.001238$ $n_z = 0.03044$	$n_x = 0.0541$ $n_y = 0.001238$ $n_z = 0.03044$
1×10^{10}	$n_x = 0.8407$ $n_y = 0.009189$ $n_z = 0.6786$	$n_x = 0.3966$ $n_y = 0.009568$ $n_z = 0.2804$	$n_x = 0.0811$ $n_y = 0.008064$ $n_z = 0.06472$	$n_x = 0.0811$ $n_y = 0.008064$ $n_z = 0.06472$

Table 3.4: Total Error, n_i for a finite element mesh with dimensions $10 \times 10 \times 10$.

α_2 \ α_1	0	1×10^{10}	1×10^{20}	1×10^{30}
0	$\bar{n}_x = 0.06089$ $\bar{n}_y = 0.0004075$ $\bar{n}_z = 0.04696$	$\bar{n}_x = 0.04557$ $\bar{n}_y = 0.0003207$ $\bar{n}_z = 0.02902$	$\bar{n}_x = 0.05064$ $\bar{n}_y = 0.0003549$ $\bar{n}_z = 0.03258$	$\bar{n}_x = 0.05065$ $\bar{n}_y = 0.000355$ $\bar{n}_z = 0.03258$
1×10^6	$\bar{n}_x = 0.05827$ $\bar{n}_y = 0.0004057$ $\bar{n}_z = 0.04601$	$\bar{n}_x = 0.04306$ $\bar{n}_y = 0.0003189$ $\bar{n}_z = 0.02804$	$\bar{n}_x = 0.04763$ $\bar{n}_y = 0.0003531$ $\bar{n}_z = 0.03147$	$\bar{n}_x = 0.04763$ $\bar{n}_y = 0.0003531$ $\bar{n}_z = 0.03148$
1×10^8	$\bar{n}_x = 0.03507$ $\bar{n}_y = 0.0003694$ $\bar{n}_z = 0.03022$	$\bar{n}_x = 0.02158$ $\bar{n}_y = 0.0002947$ $\bar{n}_z = 0.01551$	$\bar{n}_x = 0.02155$ $\bar{n}_y = 0.0003237$ $\bar{n}_z = 0.01714$	$\bar{n}_x = 0.02155$ $\bar{n}_y = 0.0003237$ $\bar{n}_z = 0.01714$
1×10^9	$\bar{n}_x = 0.05736$ $\bar{n}_y = 0.001034$ $\bar{n}_z = 0.04587$	$\bar{n}_x = 0.01909$ $\bar{n}_y = 0.0008445$ $\bar{n}_z = 0.01364$	$\bar{n}_x = 0.01424$ $\bar{n}_y = 0.0007797$ $\bar{n}_z = 0.01098$	$\bar{n}_x = 0.01424$ $\bar{n}_y = 0.0007797$ $\bar{n}_z = 0.01098$
1×10^{10}	$\bar{n}_x = 0.07755$ $\bar{n}_y = 0.005268$ $\bar{n}_z = 0.1362$	$\bar{n}_x = 0.1207$ $\bar{n}_y = 0.005083$ $\bar{n}_z = 0.04215$	$\bar{n}_x = 0.02088$ $\bar{n}_y = 0.004188$ $\bar{n}_z = 0.01813$	$\bar{n}_x = 0.02088$ $\bar{n}_y = 0.004188$ $\bar{n}_z = 0.01813$

Table 3.5: Precision Error, $\bar{n}_i$ for a finite element mesh with dimensions $10 \times 10 \times 10$.

α_2 \ α_1	0	1×10^{10}	1×10^{20}	1×10^{30}
0	$\hat{n}_x = 0.1048$ $\hat{n}_y = 0.000323$ $\hat{n}_z = 0.06304$	$\hat{n}_x = 0.04935$ $\hat{n}_y = 0.0003622$ $\hat{n}_z = 0.03429$	$\hat{n}_x = 0.0644$ $\hat{n}_y = 0.00039$ $\hat{n}_z = 0.04034$	$\hat{n}_x = 0.0644$ $\hat{n}_y = 0.00039$ $\hat{n}_z = 0.04034$
1×10^6	$\hat{n}_x = 0.1041$ $\hat{n}_y = 0.0003219$ $\hat{n}_z = 0.06269$	$\hat{n}_x = 0.0486$ $\hat{n}_y = 0.0003608$ $\hat{n}_z = 0.03399$	$\hat{n}_x = 0.06376$ $\hat{n}_y = 0.0003883$ $\hat{n}_z = 0.04002$	$\hat{n}_x = 0.06376$ $\hat{n}_y = 0.0003883$ $\hat{n}_z = 0.04002$
1×10^8	$\hat{n}_x = 0.08557$ $\hat{n}_y = 0.0002905$ $\hat{n}_z = 0.05655$	$\hat{n}_x = 0.04043$ $\hat{n}_y = 0.0002968$ $\hat{n}_z = 0.02839$	$\hat{n}_x = 0.05455$ $\hat{n}_y = 0.0003164$ $\hat{n}_z = 0.03353$	$\hat{n}_x = 0.05455$ $\hat{n}_y = 0.0003164$ $\hat{n}_z = 0.03353$
1×10^9	$\bar{n}_x = 0.2245$ $\hat{n}_y = 0.001027$ $\hat{n}_z = 0.1434$	$\hat{n}_x = 0.07472$ $\hat{n}_y = 0.001033$ $\hat{n}_z = 0.04092$	$\hat{n}_x = 0.05219$ $\hat{n}_y = 0.0009614$ $\hat{n}_z = 0.02839$	$\hat{n}_x = 0.05219$ $\hat{n}_y = 0.0009614$ $\hat{n}_z = 0.02839$
1×10^{10}	$\bar{n}_x = 0.8372$ $\hat{n}_y = 0.007529$ $\hat{n}_z = 0.6648$	$\hat{n}_x = 0.3778$ $\hat{n}_y = 0.008106$ $\hat{n}_z = 0.2772$	$\hat{n}_x = 0.07837$ $\hat{n}_y = 0.006891$ $\hat{n}_z = 0.06213$	$\hat{n}_x = 0.07837$ $\hat{n}_y = 0.006891$ $\hat{n}_z = 0.06213$

Table 3.6: Bias Error, $\hat{n}_i$ for a finite element mesh with dimensions $10 \times 10 \times 10$.

α_1 \ α_2	0	1×10^{10}	1×10^{20}	1×10^{30}
0	$n_x = 0.1805$ $n_y = 0.000793$ $n_z = 0.116$	$n_x = 0.0913$ $n_y = 0.0006456$ $n_z = 0.05113$	$n_x = 0.09821$ $n_y = 0.0006728$ $n_z = 0.05441$	$n_x = 0.09822$ $n_y = 0.0006729$ $n_z = 0.05442$
1×10^6	$n_x = 0.1484$ $n_y = 0.0007384$ $n_z = 0.1011$	$n_x = 0.07462$ $n_y = 0.0006296$ $n_z = 0.04424$	$n_x = 0.0819$ $n_y = 0.0006567$ $n_z = 0.04742$	$n_x = 0.0819$ $n_y = 0.0006567$ $n_z = 0.04742$
1×10^8	$n_x = 0.05181$ $n_y = 0.0005831$ $n_z = 0.04048$	$n_x = 0.04881$ $n_y = 0.0005557$ $n_z = 0.02455$	$n_x = 0.05381$ $n_y = 0.0005678$ $n_z = 0.02614$	$n_x = 0.05382$ $n_y = 0.0005678$ $n_z = 0.02614$
1×10^9	$n_x = 0.3078$ $n_y = 0.002272$ $n_z = 0.1948$	$n_x = 0.09465$ $n_y = 0.001681$ $n_z = 0.05223$	$n_x = 0.0578$ $n_y = 0.001514$ $n_z = 0.03037$	$n_x = 0.0578$ $n_y = 0.001514$ $n_z = 0.03037$
1×10^{10}	$n_x = 0.8192$ $n_y = 0.009006$ $n_z = 0.6591$	$n_x = 0.374$ $n_y = 0.009088$ $n_z = 0.299$	$n_x = 0.08593$ $n_y = 0.007926$ $n_z = 0.07012$	$n_x = 0.08593$ $n_y = 0.007926$ $n_z = 0.07012$

Table 3.7: Total Error, n_i for a finite element mesh with dimensions $20 \times 20 \times 20$.

α_1 \ α_2	0	1×10^{10}	1×10^{20}	1×10^{30}
0	$\bar{n}_x = 0.1007$ $\bar{n}_y = 0.0006578$ $\bar{n}_z = 0.07113$	$\bar{n}_x = 0.06878$ $\bar{n}_y = 0.0005092$ $\bar{n}_z = 0.03942$	$\bar{n}_x = 0.07148$ $\bar{n}_y = 0.0005339$ $\bar{n}_z = 0.0413$	$\bar{n}_x = 0.0715$ $\bar{n}_y = 0.000534$ $\bar{n}_z = 0.0413$
1×10^6	$\bar{n}_x = 0.07848$ $\bar{n}_y = 0.0006098$ $\bar{n}_z = 0.05903$	$\bar{n}_x = 0.05101$ $\bar{n}_y = 0.0004946$ $\bar{n}_z = 0.03253$	$\bar{n}_x = 0.05333$ $\bar{n}_y = 0.0005192$ $\bar{n}_z = 0.03417$	$\bar{n}_x = 0.05332$ $\bar{n}_y = 0.0005192$ $\bar{n}_z = 0.03417$
1×10^8	$\bar{n}_x = 0.02016$ $\bar{n}_y = 0.0004771$ $\bar{n}_z = 0.01549$	$\bar{n}_x = 0.01158$ $\bar{n}_y = 0.00045$ $\bar{n}_z = 0.0106$	$\bar{n}_x = 0.01208$ $\bar{n}_y = 0.0004612$ $\bar{n}_z = 0.01067$	$\bar{n}_x = 0.01208$ $\bar{n}_y = 0.0004612$ $\bar{n}_z = 0.01067$
1×10^9	$\bar{n}_x = 0.06178$ $\bar{n}_y = 0.001639$ $\bar{n}_z = 0.06978$	$\bar{n}_x = 0.01308$ $\bar{n}_y = 0.00105$ $\bar{n}_z = 0.01457$	$\bar{n}_x = 0.009975$ $\bar{n}_y = 0.0009472$ $\bar{n}_z = 0.009417$	$\bar{n}_x = 0.009975$ $\bar{n}_y = 0.0009472$ $\bar{n}_z = 0.009417$
1×10^{10}	$\bar{n}_x = 0.07769$ $\bar{n}_y = 0.004779$ $\bar{n}_z = 0.1233$	$\bar{n}_x = 0.03159$ $\bar{n}_y = 0.004557$ $\bar{n}_z = 0.04204$	$\bar{n}_x = 0.01998$ $\bar{n}_y = 0.003971$ $\bar{n}_z = 0.01898$	$\bar{n}_x = 0.01998$ $\bar{n}_y = 0.003971$ $\bar{n}_z = 0.01898$

Table 3.8: Precision Error, $\bar{n}_i$ for a finite element mesh with dimensions $20 \times 20 \times 20$.

α_2 α_1	0	1×10^{10}	1×10^{20}	1×10^{30}
0	$\hat{n}_x = 0.1498$ $\hat{n}_y = 0.0004428$ $\hat{n}_z = 0.0916$	$\hat{n}_x = 0.06004$ $\hat{n}_y = 0.0003968$ $\hat{n}_z = 0.03256$	$\hat{n}_x = 0.06734$ $\hat{n}_y = 0.0004094$ $\hat{n}_z = 0.03543$	$\hat{n}_x = 0.06733$ $\hat{n}_y = 0.0004094$ $\hat{n}_z = 0.03544$
1×10^6	$\hat{n}_x = 0.126$ $\hat{n}_y = 0.0004165$ $\hat{n}_z = 0.08206$	$\hat{n}_x = 0.05447$ $\hat{n}_y = 0.0003896$ $\hat{n}_z = 0.02998$	$\hat{n}_x = 0.06216$ $\hat{n}_y = 0.0004021$ $\hat{n}_z = 0.03289$	$\hat{n}_x = 0.06216$ $\hat{n}_y = 0.0004021$ $\hat{n}_z = 0.03289$
1×10^8	$\hat{n}_x = 0.04773$ $\hat{n}_y = 0.0003352$ $\hat{n}_z = 0.0374$	$\hat{n}_x = 0.04742$ $\hat{n}_y = 0.000326$ $\hat{n}_z = 0.02214$	$\hat{n}_x = 0.05244$ $\hat{n}_y = 0.0003312$ $\hat{n}_z = 0.02387$	$\hat{n}_x = 0.05244$ $\hat{n}_y = 0.0003312$ $\hat{n}_z = 0.02387$
1×10^9	$\hat{n}_x = 0.3015$ $\hat{n}_y = 0.001573$ $\hat{n}_z = 0.1819$	$\hat{n}_x = 0.09374$ $\hat{n}_y = 0.001312$ $\hat{n}_z = 0.05016$	$\hat{n}_x = 0.05693$ $\hat{n}_y = 0.001181$ $\hat{n}_z = 0.02887$	$\hat{n}_x = 0.05693$ $\hat{n}_y = 0.001181$ $\hat{n}_z = 0.02887$
1×10^{10}	$\hat{n}_x = 0.8155$ $\hat{n}_y = 0.007634$ $\hat{n}_z = 0.6475$	$\hat{n}_x = 0.3726$ $\hat{n}_y = 0.007862$ $\hat{n}_z = 0.296$	$\hat{n}_x = 0.08357$ $\hat{n}_y = 0.006859$ $\hat{n}_z = 0.0675$	$\hat{n}_x = 0.08357$ $\hat{n}_y = 0.006859$ $\hat{n}_z = 0.0675$

Table 3.9: Bias Error, $\hat{n}_i$ for a finite element mesh with dimensions $20 \times 20 \times 20$.

α_2 α_1	0	1×10^{10}	1×10^{20}	1×10^{30}
0	$n_x = 0.1907$ $n_y = 0.001139$ $n_z = 0.1236$	$n_x = 0.1213$ $n_y = 0.001$ $n_z = 0.08058$	$n_x = 0.135$ $n_y = 0.001079$ $n_z = 0.0942$	$n_x = 0.135$ $n_y = 0.001079$ $n_z = 0.09411$
1×10^6	$n_x = 0.1554$ $n_y = 0.001075$ $n_z = 0.106$	$n_x = 0.08644$ $n_y = 0.0009404$ $n_z = 0.05916$	$n_x = 0.09799$ $n_y = 0.001013$ $n_z = 0.06872$	$n_x = 0.09799$ $n_y = 0.001013$ $n_z = 0.06872$
1×10^8	$n_x = 0.09279$ $n_y = 0.000887$ $n_z = 0.06263$	$n_x = 0.04655$ $n_y = 0.0007109$ $n_z = 0.03296$	$n_x = 0.05797$ $n_y = 0.0007525$ $n_z = 0.03783$	$n_x = 0.05797$ $n_y = 0.0007525$ $n_z = 0.03783$
1×10^9	$n_x = 0.2374$ $n_y = 0.002286$ $n_z = 0.1497$	$n_x = 0.07974$ $n_y = 0.001614$ $n_z = 0.0448$	$n_x = 0.05559$ $n_y = 0.001482$ $n_z = 0.03178$	$n_x = 0.05559$ $n_y = 0.001482$ $n_z = 0.03178$
1×10^{10}	$n_x = 0.8466$ $n_y = 0.008526$ $n_z = 0.6856$	$n_x = 0.4092$ $n_y = 0.008624$ $n_z = 0.2878$	$n_x = 0.08606$ $n_y = 0.007744$ $n_z = 0.06918$	$n_x = 0.08606$ $n_y = 0.007744$ $n_z = 0.06918$

Table 3.10: Total Error, n_i for a finite element mesh with dimensions $30 \times 30 \times 30$.

α_2 / α_1	0	1×10^{10}	1×10^{20}	1×10^{30}
0	$\bar{n}_x = 0.1312$ $\bar{n}_y = 0.0009793$ $\bar{n}_z = 0.09029$	$\bar{n}_x = 0.09825$ $\bar{n}_y = 0.0008185$ $\bar{n}_z = 0.06455$	$\bar{n}_x = 0.1067$ $\bar{n}_y = 0.0008875$ $\bar{n}_z = 0.07569$	$\bar{n}_x = 0.1068$ $\bar{n}_y = 0.0008874$ $\bar{n}_z = 0.0756$
1×10^6	$\bar{n}_x = 0.08942$ $\bar{n}_y = 0.0009218$ $\bar{n}_z = 0.07176$	$\bar{n}_x = 0.06318$ $\bar{n}_y = 0.0007638$ $\bar{n}_z = 0.04277$	$\bar{n}_x = 0.06789$ $\bar{n}_y = 0.0008267$ $\bar{n}_z = 0.04982$	$\bar{n}_x = 0.06789$ $\bar{n}_y = 0.0008267$ $\bar{n}_z = 0.04982$
1×10^8	$\bar{n}_x = 0.03699$ $\bar{n}_y = 0.0007503$ $\bar{n}_z = 0.03099$	$\bar{n}_x = 0.022$ $\bar{n}_y = 0.0005814$ $\bar{n}_z = 0.01517$	$\bar{n}_x = 0.02146$ $\bar{n}_y = 0.0006179$ $\bar{n}_z = 0.01647$	$\bar{n}_x = 0.02146$ $\bar{n}_y = 0.0006179$ $\bar{n}_z = 0.01647$
1×10^9	$\bar{n}_x = 0.05871$ $\bar{n}_y = 0.001519$ $\bar{n}_z = 0.04563$	$\bar{n}_x = 0.01971$ $\bar{n}_y = 0.0009798$ $\bar{n}_z = 0.01338$	$\bar{n}_x = 0.01469$ $\bar{n}_y = 0.0009049$ $\bar{n}_z = 0.01085$	$\bar{n}_x = 0.01469$ $\bar{n}_y = 0.0009049$ $\bar{n}_z = 0.01085$
1×10^{10}	$\bar{n}_x = 0.07348$ $\bar{n}_y = 0.004485$ $\bar{n}_z = 0.1342$	$\bar{n}_x = 0.1226$ $\bar{n}_y = 0.004303$ $\bar{n}_z = 0.04221$	$\bar{n}_x = 0.02092$ $\bar{n}_y = 0.003821$ $\bar{n}_z = 0.01819$	$\bar{n}_x = 0.02092$ $\bar{n}_y = 0.003821$ $\bar{n}_z = 0.01819$

Table 3.11: Precision Error, $\bar{n}_i$ for a finite element mesh with dimensions $30 \times 30 \times 30$.

α_2 / α_1	0	1×10^{10}	1×10^{20}	1×10^{30}
0	$\hat{n}_x = 0.1384$ $\hat{n}_y = 0.0005816$ $\hat{n}_z = 0.08436$	$\hat{n}_x = 0.07118$ $\hat{n}_y = 0.0005749$ $\hat{n}_z = 0.04823$	$\hat{n}_x = 0.08258$ $\hat{n}_y = 0.0006145$ $\hat{n}_z = 0.05608$	$\hat{n}_x = 0.08259$ $\hat{n}_y = 0.0006145$ $\hat{n}_z = 0.05604$
1×10^6	$\hat{n}_x = 0.1271$ $\hat{n}_y = 0.0005533$ $\hat{n}_z = 0.07797$	$\hat{n}_x = 0.059$ $\hat{n}_y = 0.0005487$ $\hat{n}_z = 0.04087$	$\hat{n}_x = 0.07066$ $\hat{n}_y = 0.0005858$ $\hat{n}_z = 0.04733$	$\hat{n}_x = 0.07066$ $\hat{n}_y = 0.0005858$ $\hat{n}_z = 0.04733$
1×10^8	$\hat{n}_x = 0.0851$ $\hat{n}_y = 0.0004731$ $\hat{n}_z = 0.05443$	$\hat{n}_x = 0.04102$ $\hat{n}_y = 0.000409$ $\hat{n}_z = 0.02927$	$\hat{n}_x = 0.05386$ $\hat{n}_y = 0.0004295$ $\hat{n}_z = 0.03406$	$\hat{n}_x = 0.05386$ $\hat{n}_y = 0.0004295$ $\hat{n}_z = 0.03406$
1×10^9	$\bar{n}_x = 0.23$ $\hat{n}_y = 0.001708$ $\hat{n}_z = 0.1426$	$\hat{n}_x = 0.07727$ $\hat{n}_y = 0.001282$ $\hat{n}_z = 0.04275$	$\hat{n}_x = 0.05361$ $\hat{n}_y = 0.001173$ $\hat{n}_z = 0.02987$	$\hat{n}_x = 0.05361$ $\hat{n}_y = 0.001173$ $\hat{n}_z = 0.02987$
1×10^{10}	$\bar{n}_x = 0.8434$ $\hat{n}_y = 0.007252$ $\hat{n}_z = 0.6723$	$\hat{n}_x = 0.3904$ $\hat{n}_y = 0.007473$ $\hat{n}_z = 0.2847$	$\hat{n}_x = 0.08348$ $\hat{n}_y = 0.006736$ $\hat{n}_z = 0.06674$	$\hat{n}_x = 0.08348$ $\hat{n}_y = 0.006736$ $\hat{n}_z = 0.06674$

Table 3.12: Bias Error, $\hat{n}_i$ for a finite element mesh with dimensions $30 \times 30 \times 30$.

α_2 / α_1	0	1×10^{10}	1×10^{20}	1×10^{30}
0	$n_x = 0.2195$ $n_y = 0.001309$ $n_z = 0.1421$	$n_x = 0.1383$ $n_y = 0.0011$ $n_z = 0.0874$	$n_x = 0.1425$ $n_y = 0.001129$ $n_z = 0.08941$	$n_x = 0.1425$ $n_y = 0.001129$ $n_z = 0.08939$
1×10^6	$n_x = 0.1208$ $n_y = 0.001086$ $n_z = 0.08915$	$n_x = 0.07535$ $n_y = 0.0009774$ $n_z = 0.05112$	$n_x = 0.08095$ $n_y = 0.001008$ $n_z = 0.05356$	$n_x = 0.08094$ $n_y = 0.001008$ $n_z = 0.05356$
1×10^8	$n_x = 0.05759$ $n_y = 0.0009039$ $n_z = 0.0422$	$n_x = 0.04915$ $n_y = 0.00071$ $n_z = 0.02556$	$n_x = 0.05314$ $n_y = 0.000718$ $n_z = 0.027$	$n_x = 0.05314$ $n_y = 0.000718$ $n_z = 0.027$
1×10^9	$n_x = 0.3334$ $n_y = 0.002427$ $n_z = 0.2052$	$n_x = 0.09556$ $n_y = 0.001599$ $n_z = 0.05422$	$n_x = 0.0581$ $n_y = 0.001471$ $n_z = 0.03196$	$n_x = 0.0581$ $n_y = 0.001471$ $n_z = 0.03196$
1×10^{10}	$n_x = 0.8218$ $n_y = 0.008158$ $n_z = 0.6622$	$n_x = 0.3779$ $n_y = 0.008392$ $n_z = 0.303$	$n_x = 0.08686$ $n_y = 0.007652$ $n_z = 0.07126$	$n_x = 0.08686$ $n_y = 0.007652$ $n_z = 0.07126$

Table 3.13: Total Error, n_i for a finite element mesh with dimensions $40 \times 40 \times 40$.

α_2 / α_1	0	1×10^{10}	1×10^{20}	1×10^{30}
0	$\bar{n}_x = 0.1785$ $\bar{n}_y = 0.001132$ $\bar{n}_z = 0.1162$	$\bar{n}_x = 0.1152$ $\bar{n}_y = 0.0009689$ $\bar{n}_z = 0.07362$	$\bar{n}_x = 0.1171$ $\bar{n}_y = 0.0009948$ $\bar{n}_z = 0.07484$	$\bar{n}_x = 0.1171$ $\bar{n}_y = 0.0009948$ $\bar{n}_z = 0.07483$
1×10^6	$\bar{n}_x = 0.07871$ $\bar{n}_y = 0.0009303$ $\bar{n}_z = 0.06398$	$\bar{n}_x = 0.05088$ $\bar{n}_y = 0.0008597$ $\bar{n}_z = 0.03841$	$\bar{n}_x = 0.05243$ $\bar{n}_y = 0.0008865$ $\bar{n}_z = 0.03955$	$\bar{n}_x = 0.05243$ $\bar{n}_y = 0.0008865$ $\bar{n}_z = 0.03955$
1×10^8	$\bar{n}_x = 0.02161$ $\bar{n}_y = 0.0007546$ $\bar{n}_z = 0.01827$	$\bar{n}_x = 0.01051$ $\bar{n}_y = 0.0006215$ $\bar{n}_z = 0.0103$	$\bar{n}_x = 0.01106$ $\bar{n}_y = 0.0006295$ $\bar{n}_z = 0.01033$	$\bar{n}_x = 0.01106$ $\bar{n}_y = 0.0006295$ $\bar{n}_z = 0.01033$
1×10^9	$\bar{n}_x = 0.06936$ $\bar{n}_y = 0.001651$ $\bar{n}_z = 0.07577$	$\bar{n}_x = 0.01224$ $\bar{n}_y = 0.000949$ $\bar{n}_z = 0.0143$	$\bar{n}_x = 0.009239$ $\bar{n}_y = 0.0008717$ $\bar{n}_z = 0.009114$	$\bar{n}_x = 0.009239$ $\bar{n}_y = 0.0008717$ $\bar{n}_z = 0.009113$
1×10^{10}	$\bar{n}_x = 0.07588$ $\bar{n}_y = 0.004286$ $\bar{n}_z = 0.1205$	$\bar{n}_x = 0.02808$ $\bar{n}_y = 0.004191$ $\bar{n}_z = 0.04281$	$\bar{n}_x = 0.01945$ $\bar{n}_y = 0.00376$ $\bar{n}_z = 0.01861$	$\bar{n}_x = 0.01945$ $\bar{n}_y = 0.00376$ $\bar{n}_z = 0.01861$

Table 3.14: Precision Error, $\bar{n}_i$ for a finite element mesh with dimensions $40 \times 40 \times 40$.

α_1 \ α_2	0	1×10^{10}	1×10^{20}	1×10^{30}
0	$\hat{n}_x = 0.1277$ $\hat{n}_y = 0.0006581$ $\hat{n}_z = 0.0817$	$\hat{n}_x = 0.07646$ $\hat{n}_y = 0.000521$ $\hat{n}_z = 0.0471$	$\hat{n}_x = 0.08116$ $\hat{n}_y = 0.0005345$ $\hat{n}_z = 0.04892$	$\hat{n}_x = 0.08117$ $\hat{n}_y = 0.0005346$ $\hat{n}_z = 0.0489$
1×10^6	$\hat{n}_x = 0.09158$ $\hat{n}_y = 0.0005598$ $\hat{n}_z = 0.06209$	$\hat{n}_x = 0.05559$ $\hat{n}_y = 0.000465$ $\hat{n}_z = 0.03373$	$\hat{n}_x = 0.06167$ $\hat{n}_y = 0.0004792$ $\hat{n}_z = 0.03612$	$\hat{n}_x = 0.06167$ $\hat{n}_y = 0.0004792$ $\hat{n}_z = 0.03611$
1×10^8	$\hat{n}_x = 0.05338$ $\hat{n}_y = 0.0004975$ $\hat{n}_z = 0.03804$	$\hat{n}_x = 0.04801$ $\hat{n}_y = 0.0003434$ $\hat{n}_z = 0.02339$	$\hat{n}_x = 0.05198$ $\hat{n}_y = 0.0003454$ $\hat{n}_z = 0.02494$	$\hat{n}_x = 0.05198$ $\hat{n}_y = 0.0003454$ $\hat{n}_z = 0.02494$
1×10^9	$\hat{n}_x = 0.3261$ $\hat{n}_y = 0.001779$ $\hat{n}_z = 0.1907$	$\hat{n}_x = 0.09477$ $\hat{n}_y = 0.001287$ $\hat{n}_z = 0.0523$	$\hat{n}_x = 0.05736$ $\hat{n}_y = 0.001185$ $\hat{n}_z = 0.03063$	$\hat{n}_x = 0.05736$ $\hat{n}_y = 0.001185$ $\hat{n}_z = 0.03063$
1×10^{10}	$\hat{n}_x = 0.8183$ $\hat{n}_y = 0.006941$ $\hat{n}_z = 0.6511$	$\hat{n}_x = 0.3768$ $\hat{n}_y = 0.007271$ $\hat{n}_z = 0.2999$	$\hat{n}_x = 0.08466$ $\hat{n}_y = 0.006664$ $\hat{n}_z = 0.06879$	$\hat{n}_x = 0.08466$ $\hat{n}_y = 0.006664$ $\hat{n}_z = 0.06879$

Table 3.15: Bias Error, $\hat{n}_i$ for a finite element mesh with dimensions $40 \times 40 \times 40$.

The results of these tests apply only to the RF ultrasound system, setup and tissue phantoms described in Chapter 6. A similar set of experiments may be performed for different types of imaging systems. Also note that α_1 and α_2 have units of $(intensity)^2$. The α parameters may be repeatable for different imaging systems if a reasonable value of $\int_\Omega (I_1 - I_2(\mathbf{u}^{ex}))^2 \, d\Omega$, can be calculated prior to the measurement and the α parameters are normalized by this value. Tables 3.1-3.15 suggest that the optimal parameter values for this algorithm are approximately $\alpha_1 = 1 \times 10^8$ and $\alpha_2 = 1 \times 10^{10}$ for all mesh sizes. It is these parameter values which will be used in the displacement estimation for the images of the phantoms designed in this thesis. No predictable optimum can be seen for a particular mesh size, in these examples. Thus, for reasons of computation size, a mesh size for displacement measurements will be chosen such that the element size is approximately equivalent to the $20 \times 20 \times 20$ mesh in these examples. The element size or measurement resolution for this mesh is approximately $1mm$ in all directions. An example of displacements measured from a set of phantom images is shown in Figure 3.4.
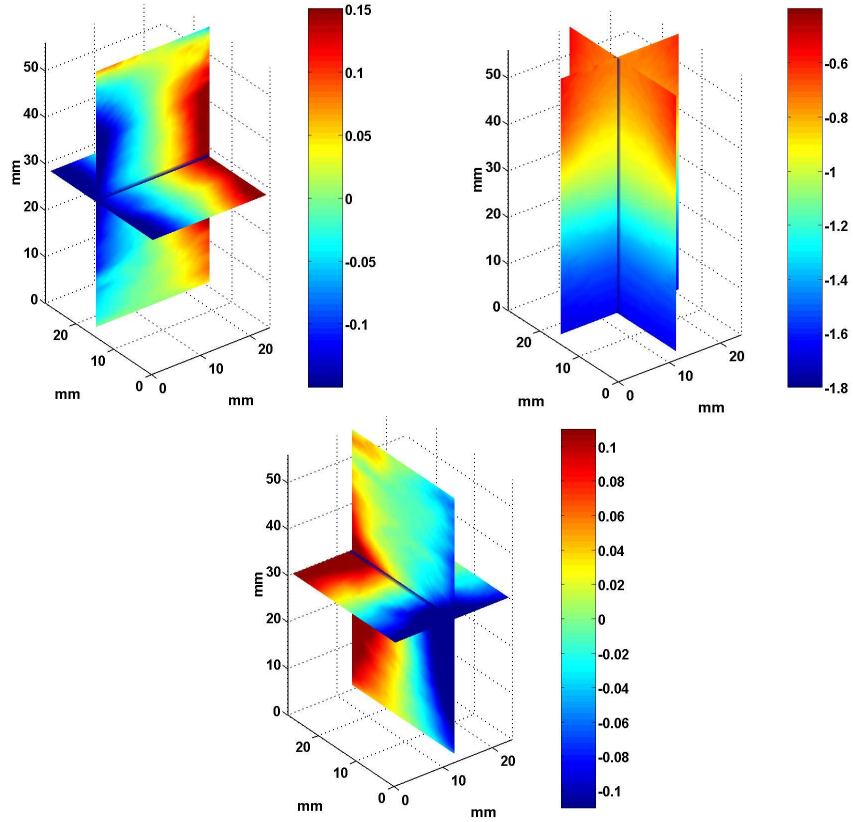
Figure 3.4: Example displacement estimates from ultrasound phantom images.

3.5   Discussion

The algorithm outlined in this chapter shows a method of extracting a measured $\mathbf{u}(\mathbf{x})$ from a pair of images, pre and post deformation images. The accuracy of this measurement is determined by the accuracy in which equation (3.1) is satisfied. Within the context of this algorithm there are three possible causes for which equation (3.1) would not be satisfied. The first is the imaging system accuracy as outlined in Section 3.2. The second is the error from the digitization of the images to 16 bit integers, which is internal to the ultrasound imaging system. The third is interpolation error from the inaccuracy of the Lagrange

polynomial interpolation. To a first approximation, it is expected that the image matching error can be represented in the following form:

$$\varepsilon_{tot} = \frac{\sqrt{\int_\Omega (I_1 - I_2(\mathbf{u}^{ex}))^2 \, d\Omega}}{\sqrt{\int_\Omega (I_1)^2 \, d\Omega}} = \varepsilon_{imgsys} + \varepsilon_{dgt} + \varepsilon_{interp}. \qquad (3.33)$$

Here, ε_{imgsys} is the imaging system error, ε_{dgt} is the digitization error, and ε_{interp} is the interpolation error. To demonstrate the relative magnitudes of each type of error in this equation, a one dimensional, analytical example was created to calculate the total error given two image lines created such that equation (3.1) is exactly satisfied with an appropriate value of u. The resulting image lines are then fed to a one dimensional version of the above algorithm, such that the interpolation scheme and the number of interpolation points is comparable to that of the three dimensional code, the value of u is exact and the resulting image error (ε_{tot}) is calculated at that value. This value is calculated for image lines with no noise and no digitization. The calculation is repeated such that the image lines have added white Gaussian noise at a SNR of ≈ 152 (see Section 3.2), but no digitization. Then again, the calculation is repeated with noise and digitization, and finally with digitization but no noise. This process is repeated over 10 representative image lines to show the variance in the calculation. The values of ε_{tot} are shown in Figure 3.5. This figure shows that the dominant source of error is the interpolation error.

Although the interpolation error is a consequence of this algorithm, any algorithm which seeks to find a displacement value which is not a multiple of a pixel value will suffer from interpolation error. Further, it can be shown that the interpolation error in this algorithm can be reduced by up sampling the image prior to measuring the displacement. To demonstrate this, consider again the one dimensional example created to quantify the total error. Using the image lines which satisfy exactly equation (3.1) (i.e. the Lagrange error is the only factor causing error in the image matching) the relative magnitude of the total error can be calculated as the image lines are up sampled. Figure 3.6 shows the plot of the total error (ε_{tot}) as a function of the distance between pixels, h, for one representative image line pair. This figure shows that the total error decreases roughly proportional to
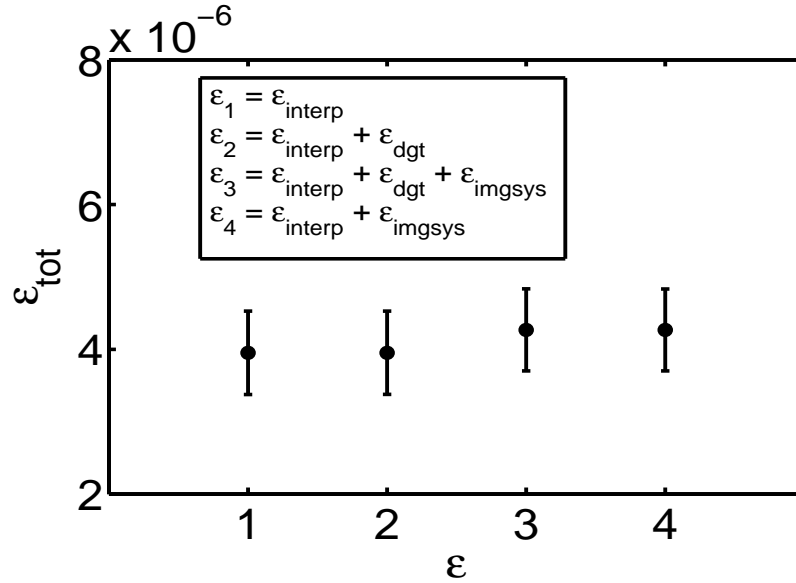
Figure 3.5: Image matching error contributions.

h^4, which corresponds to the rate of convergence for cubic Lagrange polynomials (Keys, 1981). It is also important to note, however, that the Lagrange interpolation is not an unbiased estimator and will depend on the location of an integration point relative to a pixel location (the error increases with distance from a pixel and is exact at a pixel). The consequence of this phenomenon is that the total error will not only depend on the locations of the integration points defined by $\mathbf{x}$ but will also depend largely on the local value of $\mathbf{u}$. However, if the interpolation error is considered as the only source of error, for any given local measurement, the value of $\mathbf{u}_{meas}$ should not deviate by more than a pixel magnitude from its correct value, $\mathbf{u}_{ex}$.

One other important concern when discussing global optimization problems in general, as well as the one described in this chapter, is that of local minimum. The highly oscillatory nature of these images results in the likelihood that, even from a reasonable initial guess of $\mathbf{u}$, it is possible that the algorithm will find a local minimum from which it cannot escape with iteration. Typically these minima are apparent when looking at some image
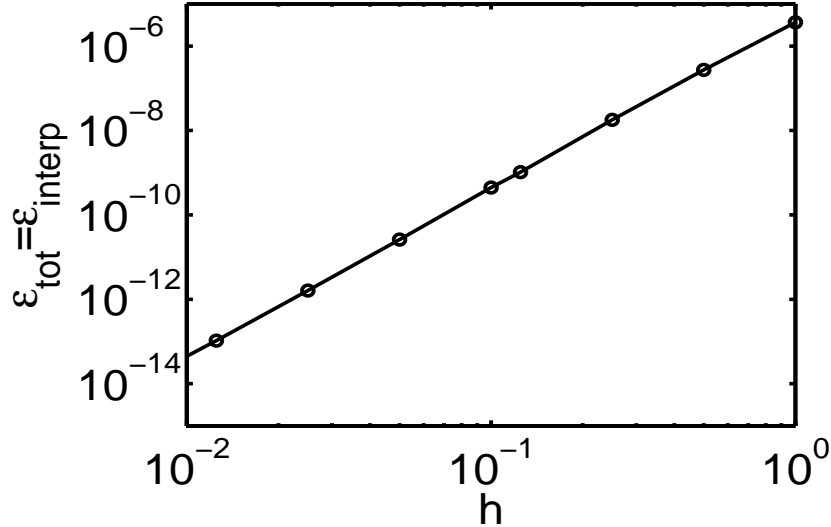
Figure 3.6: Image interpolation error as a function of the distance between pixels, h.

matching norm as a function of $\mathbf{x}$ over the matching domain, Ω. To avoid such minima, an initial guess of the displacement field is found by running the algorithm on enveloped data which is much less likely to suffer such problems.

The algorithm described in this chapter is a method to extract a measured displacement field from a set of images for any particular imaging modality, given that the images have certain characteristics. In the absence of noise, it is important that the images satisfy equation (3.1). In the case of ultrasound systems, this equation is approximately satisfied assuming minimal acoustic artifacts are present in the imaged field (e.g. reverberations). Given that equation (3.1) is approximately satisfied, this algorithm will measure a displacement field to within the accuracy it can match the images. The image matching accuracy is determined by the system noise and the noise introduced by the algorithm itself. It should be noted that if computational speed and size need not be considered, the limit of the error would be that of the imaging system alone. The amount of noise in the displacement images is going to depend on the image matching noise as well as the frequency
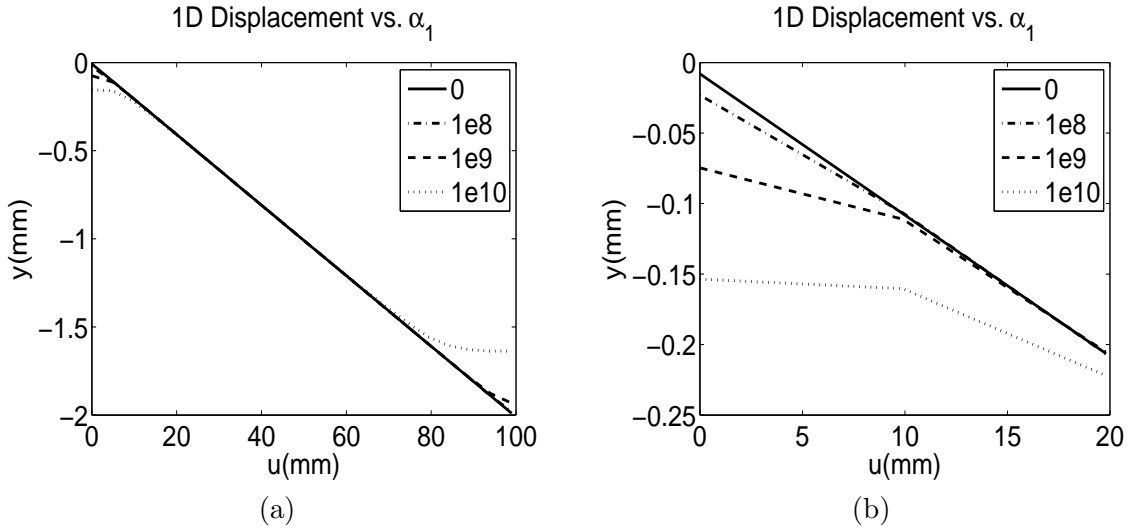
Figure 3.7: (a) A one dimensional example of displacement estimates as a function of the regularization estimates α_1. (b) A one dimensional example of displacement estimates as a function of the regularization estimates α_1, zoomed to the boundary of the estimate.

characteristics of the images themselves. To minimize the amount of noise realized in the displacement measurements, a priori knowledge of the displacement field is used in the form of regularization and incompressible terms to further constrain the measurements.

As alluded to earlier, one of the drawbacks of using regularization is the possible introduction of artifacts into the displacement estimates. To illustrate the effect these artifacts have on the displacements, a one dimensional, artificially generated example of pre and post deformation axial image lines were created. These images lines were then input to the one dimensional code, described above, to measure the displacement for varying values of the regularization parameter α_1. There is no noise in the images and the artificial displacement is linear (constant strain). There is no incompressibility term used in these measurements. Figures 3.7(a) and (b) show the resulting displacement measurements as the α_1 parameter is increased from 0 to 1×10^{10}. Figure 3.7(b) is a zoomed in plot of Figures 3.7(a) at the $y \approx 0mm$ boundary of the image line. The artifacts in the displacement estimates refer to the tendency of the boundary displacements toward a zero gradient or strain condition. These artifacts are due to the Euler-Lagrange equations of the H^1 semi-norm regularization

term. We get the Euler-Lagrange equations by taking the derivative of the regularization term, which gives:

$$D_{\mathbf{u}}\pi \cdot \mathbf{w} = \int_{\Omega} \alpha \nabla \mathbf{w} : \nabla \mathbf{u} \; d\Omega. \tag{3.34}$$

Integrating equation (3.34) by parts, and setting $D_{\mathbf{u}}\pi \cdot \mathbf{w} = 0$ for all $\mathbf{w}$ gives:

$$-\nabla \cdot (\alpha \nabla \mathbf{u}) = 0 \quad \text{in } \Omega \tag{3.35}$$

$$\text{and} \quad \alpha \frac{\partial \mathbf{u}}{\partial \mathbf{n}} = 0 \quad \text{on } \Gamma. \tag{3.36}$$

Here, n is the unit normal to the surface Γ. Equations (3.35) and (3.36) are the Euler-Lagrange equations that determine $\mathbf{u}(\mathbf{x})$. It is clear, from Figure 3.7, that equation (3.36) dominates the boundary displacement estimates for large α_1. It is recognized that these artifacts are a drawback to this algorithm and are left for future consideration.

Chapter 4

Elastic Modulus Inversions

4.1 Introduction

The last step in the process of elasticity imaging is to use the measured displacement fields as input to an inverse problem to determine the mechanical properties of the underlying material. A necessary assumption about the input to this inverse problem is that the tissue behavior can be accurately predicted by a mathematical model. In this case a linear elastic, incompressible model will be used to predict the tissue behavior. The underlying idea pursued here is that a modulus distribution is sought that is most consistent with the observed displacement field. To be precise, let $\mathbf{u}_p(\mathbf{x}; \mu)$ denote the displacement field predicted by the mathematical model (equations (2.2)-(2.4)) corresponding to a shear modulus distribution $\mu(\mathbf{x})$. Then $\mu(\mathbf{x})$ is desired such that:

$$\mathbf{u}_m(\mathbf{x}) = \mathbf{u}_p(\mathbf{x}; \mu(\mathbf{x})). \tag{4.1}$$

In order to define $\mathbf{u}_p(\mathbf{x}; \mu)$, the boundary conditions in addition to the modulus distribution need to be specified. The boundary conditions are specified in the following form:

$$\mathbf{u}(\mathbf{x}) = \mathbf{q}(\mathbf{x}) \quad \text{on} \quad \Gamma_q \tag{4.2}$$

$$\text{and} \quad (-p\mathbf{1} + \mu(\nabla\mathbf{u} + (\nabla\mathbf{u})^{\mathbf{T}})) \cdot \mathbf{n}(\mathbf{x}) = \mathbf{h}(\mathbf{x}) \quad \text{on} \quad \Gamma_h. \tag{4.3}$$

At each point on the boundaries either the traction ($\mathbf{h}(\mathbf{x})$) or the displacement ($\mathbf{q}(\mathbf{x})$) must be prescribed (i.e. $\Gamma = \Gamma_h \cup \Gamma_q$ and $\Gamma_h \cap \Gamma_q = \emptyset$). In general, equation (4.1) cannot be satisfied exactly. Therefore equation (4.1) is approximated as closely as possible within an optimization context as described in the following sections.

4.2 Optimization Formulation of the Inversion Problem

The optimization method discussed in this thesis is a gradient based, iterative optimization technique which minimizes the difference between the measured displacements $\mathbf{u}_m$ and the displacements predicted by the elasticity equations $\mathbf{u}_p$. The optimization functional is given by:

$$\pi[\mu] = \frac{1}{2} \int\limits_{\Omega} \left(T(\mathbf{u}_p(\mathbf{x}; \mu(\mathbf{x}))) - T(\mathbf{u}_m(\mathbf{x})) \right)^2 d\Omega. \tag{4.4}$$

Here T is a second order tensor whose diagonal entries represent a weighted contribution of each of the displacement components to the functional and whose off diagonal entries are zero. This allows for the inversion solution to account for the difference in the accuracy of the displacement estimates in each direction. This functional is the maximum likelihood estimator of μ if the noise in the problem (i.e. the difference in the measured displacements and the displacements predicted with the correct function for μ) has a Gaussian distribution (Press et al., 2002).

The optimization method chosen here utilizes the BFGS (Broyden Fletcher Goldfarb Shanno (Nocedal, 1980)) quasi-Newton method to minimize this difference in displacement fields. A quasi-Newton algorithm requires only the first derivative (i.e. the gradient) of the functional and its value be calculated explicitly at each iteration. Then the second derivative, or the Hessian, is approximated iteratively by calculations of the gradient at different values of the function $\mu(\mathbf{x})$. The adjoint method is used to efficiently calculate the gradient as proposed by Oberai and colleagues (Oberai et al., 2003; Oberai et al., 2004). As in the case of the image registration algorithm, using an optimization technique also allows for the implementation of regularization techniques to ensure that the inverse problem is well posed. Regularization of this problem will be discussed in Section 4.2.3. To begin the calculation of the gradient of equation (4.4) it is necessary to first consider the forward elasticity problem.

4.2.1 The Forward Elasticity Problem

The strong form of the forward elasticity problem is defined as: given the Lamé coefficients $\lambda(\mathbf{x})$ and $\mu(\mathbf{x})$ over the entire domain Ω and the boundary conditions defined by equations (4.2) and (4.3), find the displacement and pressure fields which satisfy the equations:

$$\nabla \cdot (-p\mathbf{1} + \mu(\nabla \mathbf{u} + (\nabla \mathbf{u})^{\mathbf{T}})) = \mathbf{0} \qquad \text{in} \quad \Omega \qquad (4.5)$$

$$\text{and} \qquad p = -\lambda(\nabla \cdot \mathbf{u}) \qquad \text{in} \quad \Omega \qquad (4.6)$$

In this work, $\lambda(\mathbf{x})$ is taken to be constant and large (i.e. $\lambda \gg \mu$). It is determined by specifying the Poisson's ratio ν, and evaluating $\lambda = ((2\nu)/(1 - 2\nu))\mu_{ref}$. The reference value of μ_{ref} is unity which is also the lower limit of $\mu(\mathbf{x})$ for a given reconstruction. The Poisson ratio is considered an input parameter and the accuracy of reconstructions will be considered for various values of ν close to that of incompressible materials. The pressure term will not be determined explicitly, but rather implicitly via equation (4.6). Note that for the following problem derivations, $\mathbf{u}_p(\mathbf{x})$ will be written as simply $\mathbf{u}$.

The weak form of the forward problem is defined as: find $\mathbf{u} \in \mathcal{S}$, such that

$$A(\mathbf{w}, \mathbf{u} ; \mu) = (\mathbf{w}, \mathbf{h})_{\Gamma_h} \qquad \forall \mathbf{w} \in \mathcal{V}. \qquad (4.7)$$

The bilinear forms $A(\cdot, \cdot ; \mu)$ and $(\cdot, \cdot)_{\Gamma_h}$ are defined as

$$A(\mathbf{w}, \mathbf{u} ; \mu) \equiv \int_{\Omega} (\mu \, \nabla \mathbf{w} : (\nabla \mathbf{u} + \nabla \mathbf{u}^{\mathbf{T}}) + \lambda(\nabla \cdot \mathbf{w})(\nabla \cdot \mathbf{u})) \, d\Omega \qquad \forall \mathbf{u}, \mathbf{w} \in \mathcal{V} \qquad (4.8)$$

$$(\mathbf{w}, \mathbf{h})_{\Gamma_h} \equiv \int_{\Gamma_h} \mathbf{w} \cdot \mathbf{h} \, d\Gamma. \qquad (4.9)$$

The function spaces $\mathcal{V}$ and $\mathcal{S}$ denote the set of weighting and trial solutions, respectively, defined as:

$$\mathcal{V} = \{\mathbf{w}|w_i \in H^1(\Omega), \mathbf{w} = \mathbf{0} \quad \text{on} \quad \Gamma_\mathbf{q}\} \tag{4.10}$$

$$\mathcal{S} = \{\mathbf{u}|u_i \in H^1(\Omega), \mathbf{u} = \mathbf{q} \quad \text{on} \quad \Gamma_\mathbf{q}\}. \tag{4.11}$$

To solve equation (4.7) it is necessary to discretize the functions $\mathbf{w}$, $\mathbf{u}$ and μ. These functions are approximated using the following finite element interpolation function expansions:

$$\mathbf{u}_v^h = \sum_{A=1}^{N}\sum_{i=1}^{nsd} N_A(\mathbf{x})\, d_{Ai}\, \mathbf{e}_i \tag{4.12}$$

$$\mathbf{w}^h = \sum_{A=1}^{N}\sum_{i=1}^{nsd} N_A(\mathbf{x})\, c_{Ai}\, \mathbf{e}_i \tag{4.13}$$

$$\mu^h = \sum_{B=1}^{N_\mu} \hat{N}_B(\mathbf{x})\, g_B. \tag{4.14}$$

Here N is the total number of displacement nodes in the discretization, N_μ is the total number of modulus nodes in the discretization and nsd is the number of spatial dimensions. The N_A's are finite element shape functions corresponding to node A and the d_{Ai}'s and c_{Ai}'s are the nodal values of the discretized vector functions $\mathbf{u}^h$ and $\mathbf{w}^h$, respectively. The $\hat{N}_B$'s are the finite element shape functions interpolating the modulus and the g_B's are the nodal coefficients. In these equations the h is used to denote the approximation of the functions $\mathbf{u}$, $\mathbf{w}$ and μ with functions in finite dimensional space (the Galerkin approximation). It is also important to note that the discretized function $\mathbf{u}^h$ can be separated into those nodal values and corresponding shape functions which represent the boundary conditions on Γ_q and those which fall in Ω (i.e. $\mathbf{u}^h = \mathbf{v}^h + \mathbf{q}^h$, where $\mathbf{q}^h$ lies on Γ_q). Thus equation (4.7) can be expressed as:

$$A(\mathbf{w}^h, \mathbf{v}^h; \mu^h) = (\mathbf{w}^h, \mathbf{h})_{\Gamma_h} - A(\mathbf{w}^h, \mathbf{q}^h; \mu^h) \qquad \forall \mathbf{w}^h \in \mathcal{V}^h. \tag{4.15}$$

Equation (4.15) can then be solved for $\mathbf{v}^h$. The desired displacement field is then $\mathbf{u}^h = \mathbf{v}^h + \mathbf{q}^h$. For a thorough review of the discrete forward elastostatics formulation see Hughes, 1999.

For the discretization here, the $N_A(\mathbf{x})$ is chosen to be a piecewise linear function, and the $\hat{N}_B(\mathbf{x})$ as piecewise constant over each element. Thus g_B represents the constant value of the modulus inside element B.

4.2.2 The Inverse Adjoint Elasticity Formulation

The quasi-Newton algorithm used for these inversions requires the value of the functional (4.4) and its gradient at each iteration. To calculate the gradient in a computationally efficient manner, the adjoint method is utilized. To do this, a discretized Lagrangian functional is introduced as follows:

$$\mathcal{L}[\mathbf{u}^h, \mathbf{w}^h, \mu^h] = \frac{1}{2} \int_\Omega \left(T(\mathbf{u}^h) - T(\mathbf{u}^h_m) \right)^2 d\Omega + A(\mathbf{w}^h, \mathbf{u}^h \, ; \mu^h) - (\mathbf{w}^h, \mathbf{h})_{\Gamma_h}. \qquad (4.16)$$

Here, $\mathbf{w}$ is acting as the Lagrange multiplier. The gradient of equation (4.16) is found by using the functional derivative defined in equations (3.11). Note that the functions $\mathbf{u}^h$, $\mathbf{w}^h$ and μ^h reside in the same discretized function space as their variations $\delta\mathbf{u}^h$, $\delta\mathbf{w}^h$ and $\delta\mu^h$. Thus the gradient of the Lagrangian can be expressed as:

$$\delta\mathcal{L} = D_{\mathbf{u}^h}\mathcal{L} \cdot \delta\mathbf{u}^h + D_{\mathbf{w}^h}\mathcal{L} \cdot \delta\mathbf{w}^h + D_{\mu^h}\mathcal{L} \cdot \delta\mu^h. \qquad (4.17)$$

The variations of the Lagrangian due to $\mathbf{w}$ are:

$$D_{\mathbf{w}^h}\mathcal{L} \cdot \delta\mathbf{w}^h = A(\delta\mathbf{w}^h, \mathbf{u}^h \, ; \mu^h) - (\delta\mathbf{w}^h, \mathbf{h})_{\Gamma_h}. \qquad (4.18)$$

Requiring this variation to be equal to zero (i.e. $D_{\mathbf{w}^h}\mathcal{L} \cdot \delta\mathbf{w}^h = 0 \, \forall \delta\mathbf{w}$) implies that $\mathbf{u}^h$ will satisfy the weak form of the equations of elasticity:

$$A(\delta\mathbf{w}^h, \mathbf{u}^h \, ; \mu^h) - (\delta\mathbf{w}^h, \mathbf{h})_{\Gamma_h} = A(\delta\mathbf{w}^h, \mathbf{v}^h \, ; \mu^h) + A(\delta\mathbf{w}^h, \mathbf{q}^h \, ; \mu^h) - (\delta\mathbf{w}^h, \mathbf{h})_{\Gamma_h} = 0. \quad (4.19)$$

On the constraint surface of equation (4.19), the Lagrangian equation (4.16) reduces to the original objective function of equation (4.4). Thus along the surface $\mathcal{L}[\mathbf{u}^h, \mathbf{w}^h, \mu^h] = \pi[\mu^h]$ and $\delta\pi = \delta\mathcal{L}$. Equation (4.17) can be further simplified if the Lagrange multiplier, $\mathbf{w}^h$, is chosen such that $D_{\mathbf{u}^h}\mathcal{L} \cdot \delta\mathbf{u}^h = 0 \; \forall \delta\mathbf{u}^h$. This yields:

$$A(\mathbf{w}^h, \delta\mathbf{u}^h \,; \mu^h) = -(T(\mathbf{u}^h - \mathbf{u}_m^h), T(\delta\mathbf{u})). \tag{4.20}$$

Since the elasticity operator is self-adjoint, A is symmetric (i.e. $A(\mathbf{v}_1, \mathbf{v}_2; \mu) = A(\mathbf{v}_2, \mathbf{v}_1; \mu)$ $\forall \mathbf{v}_1, \mathbf{v}_2 \in \mathcal{V}$). Therefore equation (4.20) can be rewritten as:

$$A(\delta\mathbf{u}^h, \mathbf{w}^h \,; \mu^h) = -(T(\mathbf{u}^h - \mathbf{u}_m^h), T(\delta\mathbf{u}^h)) \qquad \forall \delta\mathbf{u} \in \mathcal{V}. \tag{4.21}$$

This can then be solved for $\mathbf{w}^h$, given $\mathbf{u}^h$. Using $\mathbf{u}^h$ from the elasticity solve of equation (4.18) and the solution of $\mathbf{w}^h$ from the solution of equation (4.21), it is then possible to evaluate the remaining portions of the gradient. The final form of equation (4.17) becomes:

$$\delta\mathcal{L} = \delta\pi = D_{\mu^h}\mathcal{L} \cdot \delta\mu^h = D_\mu A(\mathbf{w}^h, \mathbf{u}^h; \mu^h) \cdot \delta\mu^h. \tag{4.22}$$

Alternatively, the discretized problem can written as:

$$\pi[\mu^h] \equiv \pi^h[g_1, g_2, ..., g_N]. \tag{4.23}$$

Then equation (4.22) and equation (4.19) may be used to show that the gradient vector is:

$$\mathbf{G}_B \equiv \frac{\partial \pi^h}{\partial g_B} = A(\mathbf{w}^h, \mathbf{u}^h; \hat{N}_B). \tag{4.24}$$

Thus calculating the gradient of equation (4.4) using the adjoint method requires only two solves of the forward elasticity matrix.

As in the image registration code, the element integration required to calculate the stiffness matrix and the right hand side vectors of the elasticity equations, as well as the gradient and function evaluations were parallelized to further improve the speed of each iteration. A parallelized linear solver (PARDISO) is also used to solve each forward problem.

4.2.3 Regularization

As is the case with displacement measurement, it is desirable to regularize the problem for the shear modulus distribution. To do this, two different types of regularization are considered and the effect on the resulting modulus reconstructions are discussed. The first regularization is the L^2 norm of the modulus distribution. The new functional π with this regularization becomes:

$$\pi[\mu] = \frac{1}{2} \int_\Omega \left(T(\mathbf{u}_p(\mathbf{x}; \mu(\mathbf{x}))) - T(\mathbf{u}_m(\mathbf{x})) \right)^2 d\Omega + \frac{\alpha_a}{2} \int_\Omega \mu^2 \, d\Omega. \tag{4.25}$$

The analysis outlined in Section 4.2.2 does not change with this new functional until the evaluation of the differential of π. Equation (4.22) is replaced by:

$$\delta\pi = D_\mu A(\mathbf{w}^h, \mathbf{u}^h, \mu^h) \cdot \delta\mu^h + \alpha_a \int_\Omega \mu^h \, \delta\mu^h \, d\Omega. \tag{4.26}$$

This type of regularization is a standard Tikhonov penalty which penalizes large values of the shear modulus within the domain Ω. It is tantamount to using a maximum a posteriori likelihood estimator with a zero-mean Gaussian prior on $\mu(\mathbf{x})$.

The second type of regularization is based on a total variation diminishing (TVD) type of penalty term. The standard TVD regularization functional term of a scalar function $\mu(\mathbf{x})$ is:

$$\pi^R[\mu] = \alpha_b \int_\Omega |\nabla\mu(\mathbf{x})| \, d\Omega. \tag{4.27}$$

In practice, the singularity in the absolute value function must be smoothed. The computational implementation of equation (4.27) chosen here is:

$$\pi^R[\mu] = \alpha_b \int_\Omega \sqrt{\nabla\mu(\mathbf{x}) \cdot \nabla\mu(\mathbf{x}) + \beta^2} \, d\Omega. \tag{4.28}$$

The constant β is user selected and "small" in an appropriate sense. The differential of this functional is:

$$\delta\pi^R = \alpha_b \int\limits_\Omega \frac{\nabla\mu \cdot \nabla\delta\mu}{\sqrt{\nabla\mu \cdot \nabla\mu + \beta^2}}\, d\Omega. \tag{4.29}$$

A further modification of this formulation is needed when applied to the discretization of μ used in this thesis. The piecewise constant, element based interpolation functions for μ have a zero gradient inside each element domain and an infinite gradient across element boundaries. Thus equation (4.27) must be treated with care.

The appropriate form of the TVD regularization to be used with piecewise continuous interpolations may be derived by considering the discontinuous limit of a continuous interpolation. To that end, a set of "temporary" nodes is introduced. Thus the finite element interpolation of $\mu(\mathbf{x})$ on this mesh is:

$$\mu^h = \sum_{A=1}^{Nt} N_A(\mathbf{x})\, g_A. \tag{4.30}$$

Here, Nt is the number of nodes on the temporary discretization of μ. If this mesh is then defined such that every two nodes in a given direction have equal values of μ, then every other element in this discretization has a constant value of μ. A simple $3 \times 3 \times 3$ element mesh with this discretization is shown in Figure 4.1. The shaded elements are those with constant values of μ. $\mu(\mathbf{x})$ changes continuously as $\mathbf{x}$ moves from one shaded element to the next, through an unshaded element. The limit in which the unshaded elements become vanishingly thin is considered next. This discretization leads to four different types of elements: those which have a constant value of μ, those which fall between two constant elements in a given direction (κ_1), those which share its corners with only four different constant μ elements in any two given directions (κ_2) and those which share all eight of its corners with eight different constant μ elements (κ_3). An 8 degree of freedom piecewise constant representation of μ can be recovered from equation (4.30) by considering the limit as Δx, Δy and Δz approach zero.

When the integral in equation (4.27), is considered for this discretization it is sufficient
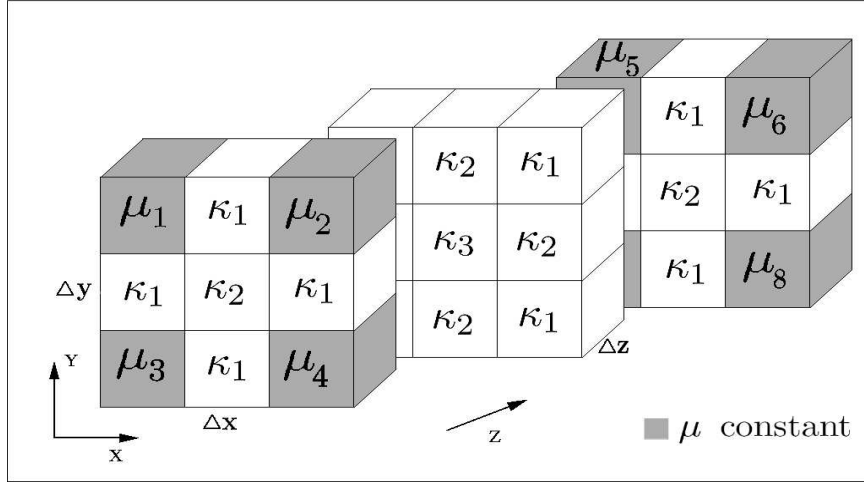
Figure 4.1: A $3 \times 3 \times 3$ element mesh used to derive the modified TVD regularization (the mesh is broken in the z direction for visual clarity).

to consider the integrals of each type of element individually. It is clear that the integral contribution from elements with a constant μ value will be contribute zero and therefore can be neglected. The integral contributions of the other element types will be considered as Δx, Δy and Δz (from Figure 4.1) go to zero (i.e. the volume of the κ elements vanish but the volume of the constant element types remain the same). In the limit as the κ elements vanish, this discretization recovers the original piecewise constant discretization.

Consider now a κ_1 type of element. Let μ_1 denote the constant value of μ on one face of the element and μ_2 denote the constant value of μ on the opposite face. Without loss of generality suppose that the x-axis is perpendicular to these faces. Then

$$|\nabla \mu| = \frac{\Delta \mu}{\Delta x} = \frac{|\mu_1 - \mu_2|}{\Delta x}. \tag{4.31}$$

Therefore:

$$\int_{\kappa_1} |\nabla \mu| d\Omega = \frac{|\mu_1 - \mu_2|}{\Delta x} \times \Delta x \times SA = |\mu_1 - \mu_2| SA. \tag{4.32}$$

Here SA represents the area of the two faces perpendicular to the x-axis. Similar calculations for the κ_2 and κ_3 element types show that their contributions to equation (4.27)

vanish as Δx, Δy and Δz go to zero.

Thus the formulation of the TVD regularization for the original piecewise constant discretization of μ can be represented by equation:

$$\pi^R = \alpha_b \sum_{i=1}^{N_S} \sqrt{[\mu]_i^2 + \beta^2} \times SA_i \qquad (4.33)$$

Here N_S is the number of element surfaces within a mesh which are shared by two elements, $[\mu]_i$ is the corresponding jump in μ across element surface i, and SA_i is the area of that element surface. A small positive β has been added to "regularize" the absolute value function. The equation for the corresponding gradient is:

$$G_B^R = \frac{\alpha_b}{2} \sum_{i=1}^{N_{SB}} \frac{SA_i \times (\mu_B - \mu_i)}{\sqrt{(\mu_B - \mu_i)^2 + \beta^2}} \qquad (4.34)$$

where N_{SB} is a number between 3 and 6, defining the number of surfaces which element B shares with neighboring elements. It is equations (4.33) and (4.34) which will define the modified TVD formulation to be added to displacement matching terms of equations (4.4) and (4.22) and used in the analysis and discussions of this thesis.

4.3 Reconstruction Parameters

The parameters involved in reconstructing the modulus images are more complicated and more numerous than in the case of the image registration algorithm. The modulus reconstructions require an optimal choice of the Poisson's ratio, appropriate boundary conditions for the forward problem, an optimal weighting of the displacements as well as a choice regularization term and a value for the regularization parameter, α. The expected resolution and accuracy of the modulus reconstruction is not expected to be any better than that of the displacement measurements, thus the mesh size for the reconstructions will be equivalent to that of the displacement mesh.

To investigate each of these reconstruction parameters an artificial displacement field

is created, from a prescribed modulus distribution, using a forward finite element analysis program. The modulus distribution is selected to model a typical ultrasound tissue mimicking phantom (see Section 6.2) in size, geometry and modulus contrast. The boundary conditions applied to this modulus distribution are made to approximate those of a typical experimental protocol, described in Sections 6.1.1 and 6.3. Only that portion of the displacement field which falls directly below the surface at the acoustic window, shown in Figure 6.3, is considered for the inverse problem. This displacement field corresponds to the imaging domain from which the displacement field would be measured in an actual phantom experiment. This displacement field is shown in Figure 4.2. The shear modulus of the inclusion and stand-off layer is three times that of the background material. The artificial phantom has dimensions of $60mm \times 60mm \times 60mm$; however, the reconstructed volume has dimensions of $30mm \times 60mm \times 30mm$ in length, height and width, respectively. The inclusion is cylindrical in shape with a diameter of $12mm$ and a height of $9mm$. A stand-off or calibration layer, of height $10.5mm$, is located at the bottom of the phantom. The motivation behind this stand-off layer is provide an area within a reconstructed modulus distribution in which the modulus is known. Without a calibration layer, the reconstructions could only be exact up to a multiplicative constant. The resulting artificial displacement field is then used as $\mathbf{u}_{meas}$ to reconstruct the shear modulus for several examples in the following sections.

The original displacement field was generated on a $40 \times 40 \times 40$ element mesh. The resulting displacement field was qualitatively compared to a field generated on a $32 \times 32 \times 32$ element mesh to ensure that the problem was well resolved.

4.3.1 Poisson's Ratio

The Poisson's ratio used in the reconstruction should ideally be the same Poisson's ratio of the material under investigation. According to Figure 2.1, the ratio of the bulk modulus to the shear modulus ($\frac{\kappa}{\mu}$) ranges from approximately 10^3-10^6 and thus the ratio
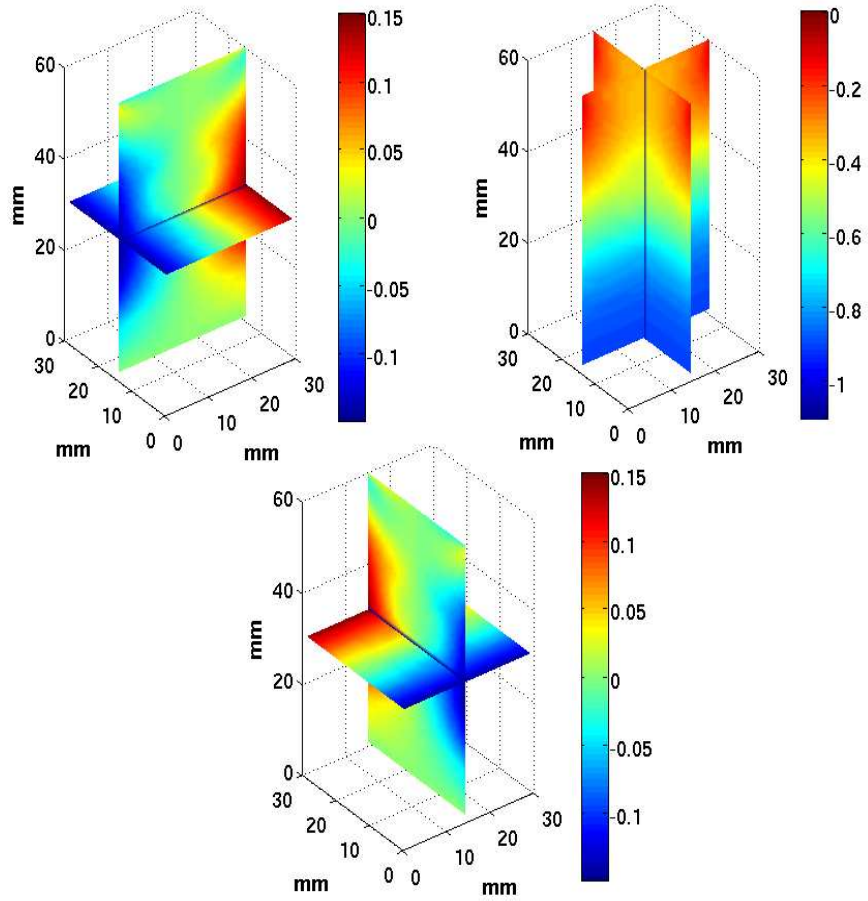
Figure 4.2: Artificial displacements from a finite element forward problem.

of the Lamé parameters ($\frac{\lambda}{\mu}$) ranges from approximately 10^3-10^6. This corresponds to a Poisson's ratio in the range 0.4995 to 0.4999995.

To illustrate the effect of changing both the Poisson's ratio of the material being tested and the Poisson's ratio used in the reconstructions, a series of artificial displacement fields was created using the mesh described in the previous section. The artificial displacement fields were constructed with varying values of the Poisson's ratio (ν_{fwd}) in the range of 0.4995 to 0.4999995. Then each of these displacement fields were used as the measured displacements in a series of reconstructions utilizing varying Poisson's ratios (ν_{inv}) in the same range. The initial guess for the modulus distribution is again a homogeneous field

ν_{inv} \ ν_{fwd}	0.4995	0.49995	0.499995	0.4999995
0.4995	$\varepsilon_\mu = 0.4872$	$\varepsilon_\mu = 0.4888$	$\varepsilon_\mu = 0.4895$	$\varepsilon_\mu = 0.4891$
0.49995	$\varepsilon_\mu = 0.4889$	$\varepsilon_\mu = 0.4823$	$\varepsilon_\mu = 0.4844$	$\varepsilon_\mu = 0.4839$
0.499995	$\varepsilon_\mu = 0.4889$	$\varepsilon_\mu = 0.4872$	$\varepsilon_\mu = 0.4863$	$\varepsilon_\mu = 0.4852$
0.4999995	$\varepsilon_\mu = 0.4896$	$\varepsilon_\mu = 0.4863$	$\varepsilon_\mu = 0.4848$	$\varepsilon_\mu = 0.4838$

Table 4.1: Reconstructed modulus error estimates as a function of the material's Poisson's ratio and the Poisson's ratio used for the reconstruction.

of value 1, which is the lower bound of the possible values of μ. For the reconstructions considered in this section, the optimization is terminated at first iteration n for which the value $(\pi(\mu^{n-5}) - \pi(\mu^n))/\pi(\mu^{n-5}) < 0.01$. That is, within the 5 iterations preceding the nth iteration, the functional does not change more than 1%. All the boundary conditions for these reconstructions were prescribed displacements. A measure of the accuracy of a reconstructions can be calculated in the form of the L^2 norm of the shear modulus shown by equation:

$$\varepsilon_\mu = \frac{\sqrt{\int_\Omega (\mu_{ex} - \mu_{rec})^2 \, d\Omega}}{\sqrt{\int_\Omega (\mu_{ex})^2 \, d\Omega}}. \tag{4.35}$$

Here μ_{ex} is the shear modulus distribution used to create the measured displacements (shown in Figure 4.3(a)), μ_{rec} is the reconstructed modulus distribution, and Ω is just that domain used to create the reconstruction. Table 4.1 shows the values of the error in the reconstructed μ distribution, calculated using equation (4.35).

The data in Table 4.1 suggests that the accuracy of the modulus reconstruction has little dependence on the choice of Poisson's ratio used in the reconstruction or the underlying material Poisson's ratio for the range of bulk and shear moduli suggested in Figure 2.1. It also shows that there is not an optimal choice of reconstructing Poisson's ratio for a given actual Poisson's ratio. Therefore, a Poisson's ratio of 0.4872 will be chosen for the reconstructions of this work. It should also be noted that the data in Table 4.1 suggests that using a constant λ in these reconstructions, rather than allowing it to vary with μ (i.e. $\lambda(\mathbf{x}) = \mu(\mathbf{x})\frac{2\nu}{1-2\nu}$), has little consequence on the resulting modulus reconstructions.

4.3.2 Boundary Conditions

The choice of boundary conditions can have a large impact on the reconstruction. This issue will be discussed in more detail in Chapter 5. For the purposes of this section, reconstructions with two types of boundary conditions will be investigated. Again, the forward problem will be created to generate the artificial displacements and the reconstructions will be done on a subsection of those displacements. The forward problem was created such that λ was fixed at 999. This corresponds to a Poisson's Ratio of 0.4995 for a homogeneous shear modulus distribution of 1. No regularization is used and the optimization is terminated at first iteration n for which the value $(\pi(\mu^{n-5}) - \pi(\mu^n))/\pi(\mu^{n-5}) < 0.01$.

The first type of reconstruction investigated is that utilizing all Dirichlet, or displacement, boundary conditions. Figure 4.3(b) shows a slice through the center of the reconstructed shear modulus and Figure 4.3(a) shows the same slice of the target modulus distribution used to produce the artificial displacement measurements. The slices are taken in the x-y plane. The value of ε_μ for this reconstruction is 0.4998. Figure 4.3 shows that reconstructions of this type accurately recover the inclusion, but fail to recover the stand-off layer.

It is also important to note that the recovered inclusion in Figure 4.3(b) does not exactly match the correct inclusion of Figure 4.3(a), even in this noiseless situation. The recovered modulus seems to be smoother, with a slightly higher peak modulus than the correct inclusion. This can be seen from the plot in Figure 4.5(b). This is a consequence of the relatively small difference in the two displacement fields resulting from the two inclusion modulus distributions, the discontinuous distribution of μ_{ex} and the continuous smooth distribution of the reconstruction. Thus the gradients of the functional, with respect to the local modulus values around the inclusion, are small. The modulus distribution is eventually expected to resolve the inclusion, in this case, if it is allowed to iterate well beyond the termination point. This can be seen in Figures 4.4(a) and (b). These figures
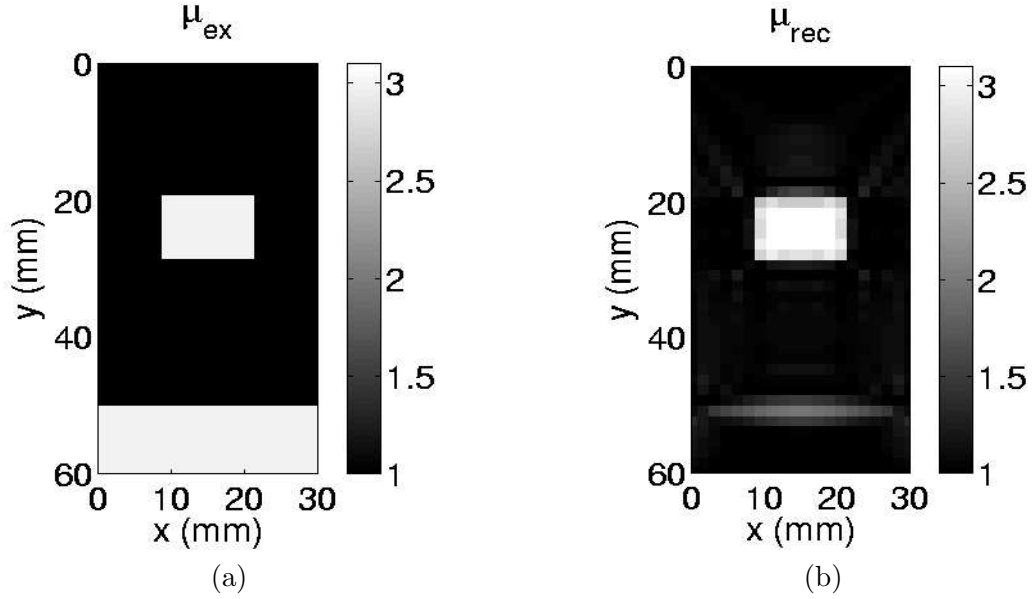
Figure 4.3: (a)The center x-y slice of μ_{ex}. (b) The center x-y slice of the reconstruction modulus, μ_{rec}.

show the functional drop and the drop in the value of ε_μ as the iterations progress beyond the termination point. The dotted line represents the iteration at which the functional has reached the termination point (i.e. $(\pi(\mu^{n-5}) - \pi(\mu^n))/\pi(\mu^{n-5}) < 0.01$). It is clear from these two plots that while the modulus error (ε_μ) continues to fall steadily after the termination point, the drop in the functional value is small relative to the decline seen prior to the termination point. This algorithm is expected to recover the inclusion exactly if allowed to iterate indefinitely. However, this is the expectation only in the absence of noise and regularization.

The second type of boundary condition investigated had a portion of its boundary assumed to be normal traction free. The sides of the reconstructed volume (i.e. the x-y and y-z boundary surfaces) are assumed to have zero normal traction ($h_n = 0$ on Γ_n^{xy} and Γ_n^{yz}). The remaining boundary conditions are Dirichlet conditions. Figure 4.5(a) shows the slice through the center of the reconstructed shear modulus in the x-y plane with these prescribed boundary conditions. The value of ε_μ for this reconstruction is 0.4588. It is clear that the inclusion and stand-off layer are clearly recovered with these boundary conditions,
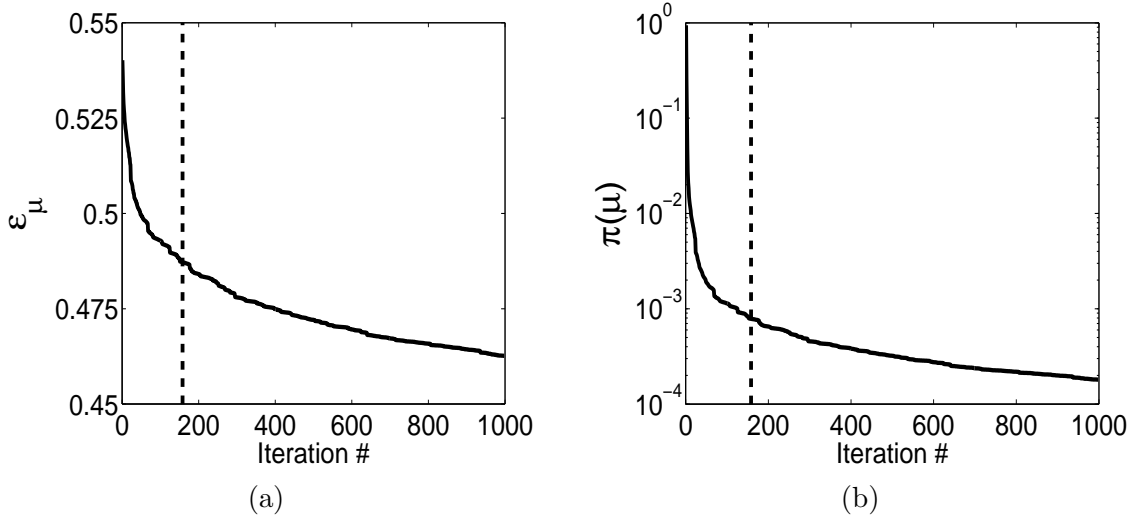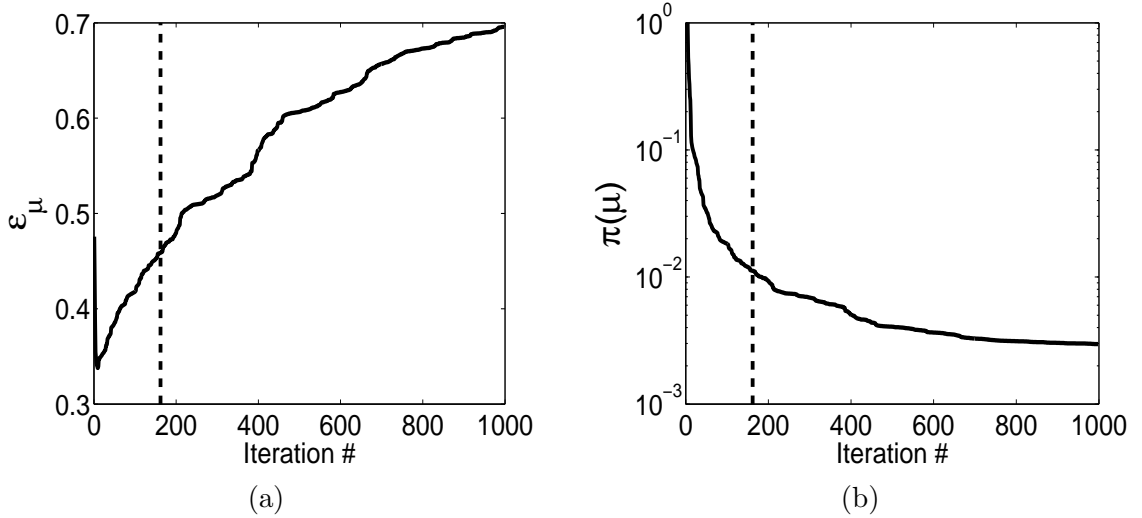
Figure 4.4: (a) Modulus error (ε_μ) as a function of iteration number for the reconstruction with all displacement boundary conditions. (b) Functional value $(\pi(\mu))$ as a function of iteration number for the reconstruction with all displacement boundary conditions.

leading to an overall improvement in the accuracy of the recovered modulus. Figure 4.5(b) shows the exact shear modulus as well as the reconstructions with both types of applied boundary conditions along the center line in the y direction.

Although prescribing these normal traction free boundaries yields a higher accuracy of the resulting modulus, it does introduce modulus artifacts to these reconstructions which can be seen in Figure 4.5. The value of the ε_μ for this reconstruction does not show as drastic an improvement in the reconstruction as the image slice of Figure 4.5(b) implies due primarily to the presence of these artifacts. The artifacts are typically areas of increased or decreased stiffness and exist mainly near the boundaries of the reconstruction. They result from the zero traction assumption. The presence of a regularization term in the reconstruction is expected to aid in minimizing the artifacts and with regularization the ε_μ is expected to be significantly lower than those values resulting from reconstructions with all displacement boundary conditions (see Section 4.3.3). Figures 4.6(a) and 4.6(b) show the functional drop and the drop in the value of ε_μ as a function of iteration number for these reconstructions. The initial drop in the value of ε_μ results from the algorithms initial
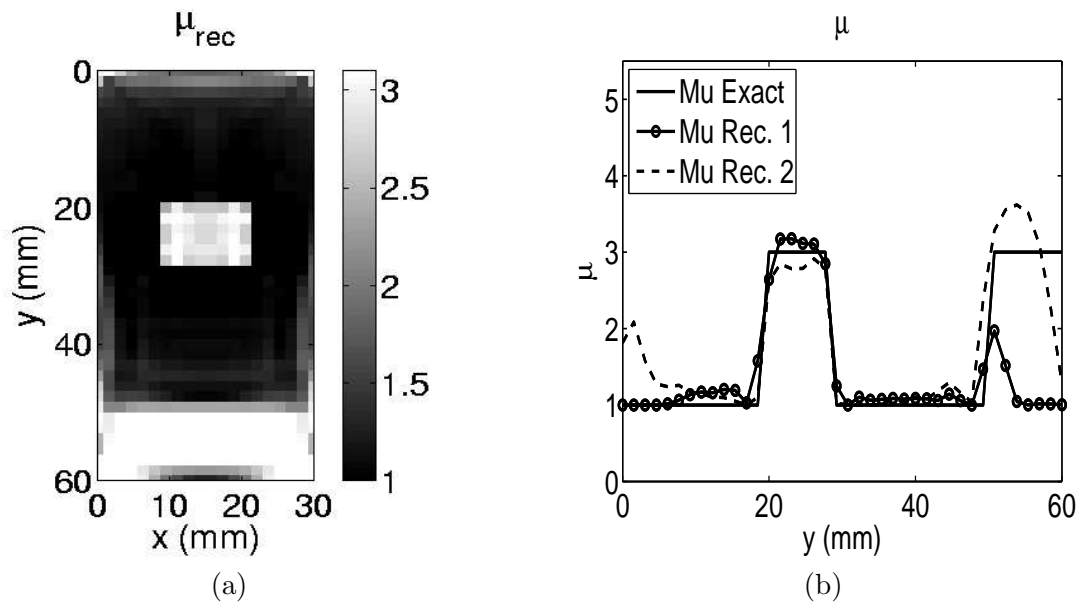
Figure 4.5: (a)The center x-y slice of μ_{rec} with mixed displacement and traction boundary conditions on the sides. (b) The exact modulus, the reconstruction with all displacement boundary conditions (Mu Rec.1) and the reconstruction with the mixed displacement and traction boundary conditions (Mu Rec.2) along a line in the y direction at the center of the artificial phantom.

Figure 4.6: (a) Modulus error (ε_μ) as a function of iteration number for the reconstruction with mixed displacement and traction boundary conditions. (b) Functional value $(\pi(\mu))$ as a function of iteration number for the reconstruction with mixed displacement and traction boundary conditions.

recovery of the inclusion and the stand-off layer and the subsequent increase in this value is due primarily to the steady increase in the magnitude of these modulus artifacts.

It should also be noted that the boundary conditions used for the second reconstruction were found to produce the best result from trials of many different combinations of $\mathbf{u} = \mathbf{u}_{meas}$ on Γ_q and $\mathbf{h} = \mathbf{0}$ on Γ_h. The zero normal traction force boundary condition resulted in the highest accuracy modulus distribution. It is these boundary conditions which will be used to run the reconstructions in Chapter 6.

4.3.3   Regularization

To determine the appropriate choice of the regularization and the regularization parameter (α) reconstructions will be performed on the artificial displacement fields with added white Gaussian noise. The noise was added such that the L^2 norm of the total error (see equation (3.30)) was approximately equal to those values shown in Table 3.7 for $\alpha_1 = 1e8$ and $\alpha_2 = 1e10$. Assuming that the dominant source of the noise in the

displacement estimates results from the interpolation error, it is reasonable to expect the values shown in Table 3.7 can closely approximate noise levels in the measurements from ultrasound images. Admittedly, the choice of adding white Gaussian noise is an approximation to the noise which would be realized in practice. The standard deviation of the noise added to these displacement fields, to create the appropriate L^2 norm, is such that $\frac{\sigma_{u_x}}{\sigma_{u_y}} \approx \frac{\sigma_{u_z}}{\sigma_{u_y}} \approx 10$. Therefore, the weighting tensor T is chosen such that the weights assigned to the u_y components of the displacements are 10 times that of u_x and u_z.

The initial guess for the modulus distribution is again a homogeneous field of value 1. For the reconstructions considered in this section, the optimization is terminated at first iteration n for which the value $(\pi(\mu^{n-5}) - \pi(\mu^n))/\pi(\mu^{n-5}) < 0.01$. The functional value used to determine the stopping criteria was the displacement matching term alone, without the regularization. Figure 4.7(a) shows the error in the reconstructed modulus distribution (ε_μ) for both the L^2 and TVD regularization types. In each case the value of α spans above and below the value found to minimize the ε_μ. Figure 4.7(b) shows a slice through the modulus distribution of the reconstruction with TVD regularization and an $\alpha = 0.001$, which was found to be the optimal value of α. To show how varying the magnitude of α affects the resulting reconstruction, center lines through reconstructed modulus distributions with several α values are plotted for the L^2 and TVD regularizations in Figures 4.8(a) and 4.8(b). Figures 4.9(a) and 4.9(b) show the reconstructed modulus error and the functional drop, respectively, for the TVD regularization with $\alpha = 0.001$ for iterations beyond the termination point, shown in the dotted line. Note that the error, ε_μ, remains at its minimum value showing the effectiveness of the regularization in minimizing the artifacts. The TVD regularization with a value of α in the range of 10^{-3}-10^{-4} will be used to reconstruct the modulus distribution from the measured displacements of the ultrasound phantoms described in Chapter 6 because it was found to yield the best result.
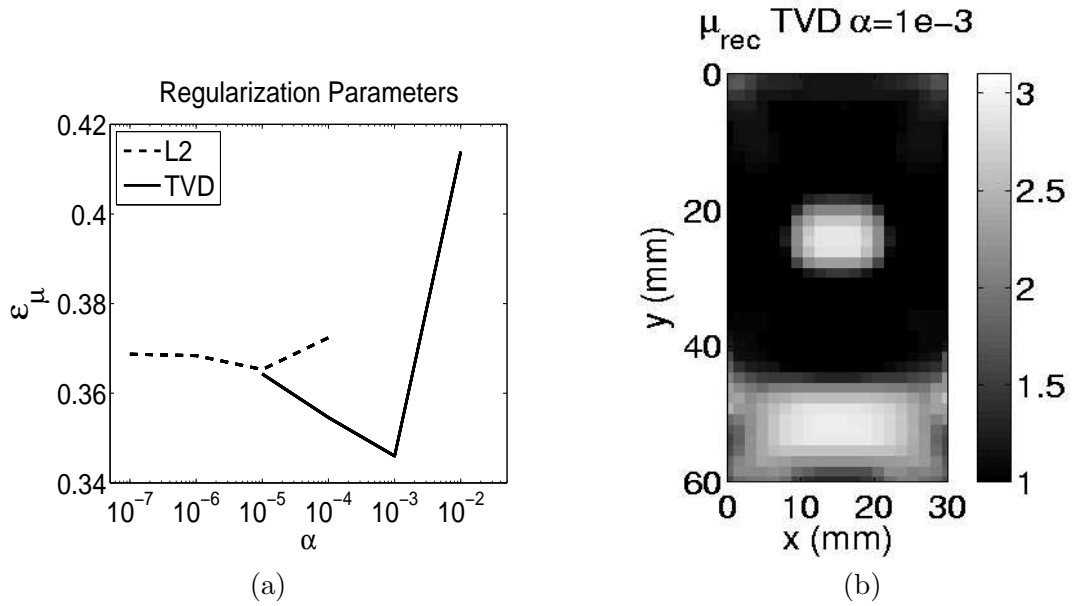
Figure 4.7: (a) Modulus error of the reconstructions with varying regularization (b) Reconstruction with TVD regularization and with $\alpha = 0.001$.
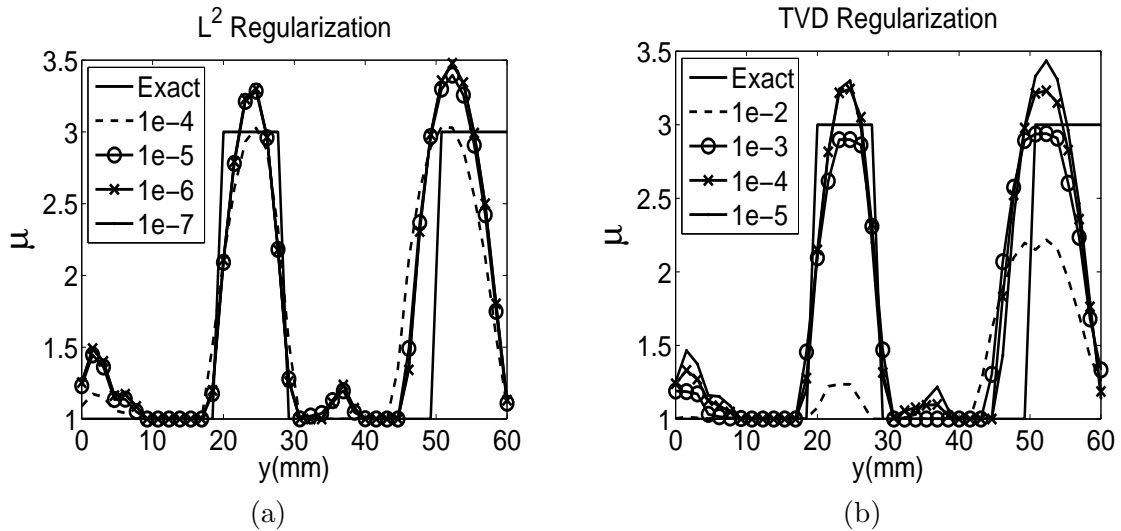

Figure 4.8: (a) The exact modulus value and several reconstructed modulus value with varying levels of L^2 regularization along the center l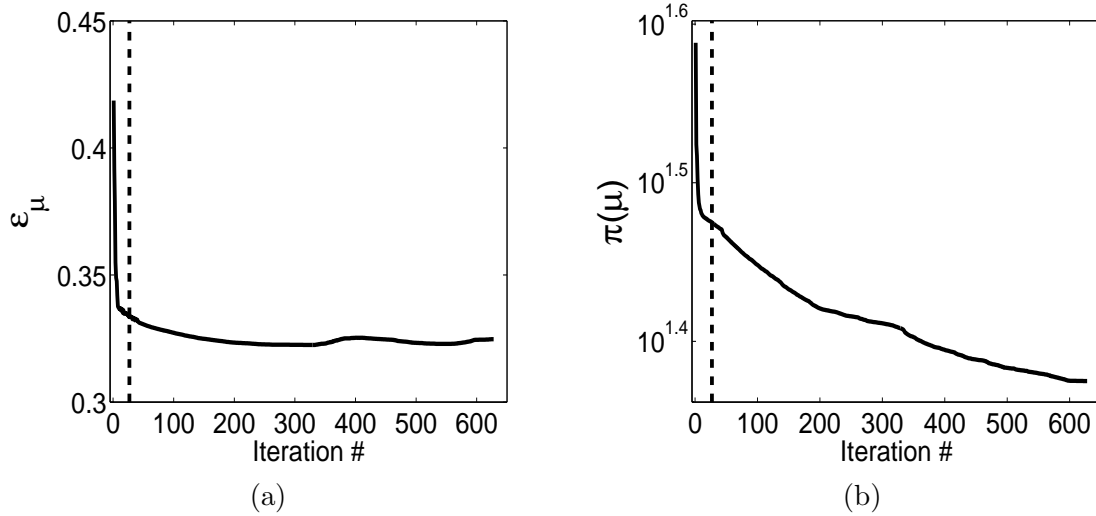ine of the artificial phantom in the y direction. (b) The exact modulus value and several reconstructed modulus value with varying levels of TVD regularization along the center line of the artificial phantom in the y direction.

Figure 4.9: (a) Modulus error (ε_μ) as a function of iteration number for the second reconstruction type with TVD regularization. (b) Functional value ($\pi(\mu)$) as a function of iteration number for the second reconstruction type with TVD regularization.

4.4   Discussion

The algorithm described in this chapter presents a method to reconstruct the shear elastic modulus from a measured displacement field, or fields, for a three dimensional linear elastic, incompressible material. It also discusses the justification of the choice of the Poisson's ratio used in the reconstructions. The boundary conditions which resulted in the most accurate solution utilized an approximation which is known to be inaccurate. In these inverse problems, the use of traction boundaries is necessary, due to the constraints which Dirichlet boundaries impose on the predicted displacements of the model. Introducing these approximations on the boundaries into the inverse problem does add inaccuracy to our reconstructions, resulting in localized modulus artifacts in areas of our reconstruction. Thus the regularization of our modulus distribution plays two important roles. It reduces the size and magnitude of these artifacts and acts to reduce the noise in the reconstructions resulting from noise in the measured displacements. With the displacement estimation technique described in Chapter 3 and the inversion method outlined here, it is now possible to implement these algorithms to measure the modulus distribution of tissue

mimicking phantoms. This experimental process will be outlined in Chapter 6.

Chapter 5

Solution Uniqueness and Sensitivity

5.1 Introduction

An important consideration in any inverse problem is the determination of how much data is required to confidently reconstruct the quantity of interest. In the case of the inverse elasticity problem studied here, this question is related to that of the uniqueness of the modulus distribution. That is, for every measured displacement field, is it the case that one and only one shear modulus distribution exists which will minimize the value of the functional? If many such solutions exist, further information (i.e. data) is required in the inverse problem in order to constrain the solution. In the case of elastic imaging, this information may be knowledge of some tractions on the boundary, known values of the elastic modulus in the imaged domain (e.g. a stand-off layer) or multiple measured displacement fields for a given imaged tissue volume.

A similar consideration, which is related to the solution's uniqueness, is the sensitivity of the displacement matching functional, or more specifically the predicted displacements, to the shear modulus distribution. This issue is of particular importance in areas of the domain which are close to boundaries with Dirichlet boundary conditions. By definition, $\mathbf{u}_p = \mathbf{u}_m$ on the Dirichlet boundaries and the value of the functional equation (4.4) is exactly zero on these boundaries. Although values of $\mathbf{u}_p^h$ on nodes close to a Dirichlet boundary are allowed to vary from $\mathbf{u}_m$, they do so to a diminishing degree as $\mathbf{x}$ approaches those boundaries. This is due, in part, to the fact that the displacement field must satisfy the equations of linear incompressible elasticity. This leads to an increasingly weak dependence of the functional on the values of μ as you approach the boundary.

This chapter will discuss some issues of uniqueness and sensitivity by studying model problems where these issues are important. It will also show the implications each issue has on the accuracy of the modulus reconstructions as well as some possible methods for addressing them. The discussion of the uniqueness of the three dimensional inverse elasticity problem presented below will somewhat parallel a similar discussion on the uniqueness of the two dimensional plane strain inverse elasticity problem presented in Barbone and Bamber, 2002 and Barbone and Gokhale, 2004.

5.2 Uniqueness: Model Problems

5.2.1 Uniaxial Stress

For some inverse problems, the dependence of the solution on the measured data can be found by rewriting the momentum equation as functions of μ or p, where the strain (ϵ) becomes the independent variable. However, the momentum equation for the three dimensional, incompressible linear elastic material (equation (2.5)) has no clear solution for μ or p. This equation can be further reduced, to eliminate the pressure variable, by taking the curl of equation (2.5) which gives:

$$\nabla \times \nabla(\mu\boldsymbol{\epsilon}) = 0. \tag{5.1}$$

While full general treatment of uniqueness in 3D remains unknown, significant insight into the question may be developed by studying model problems. It is appropriate to consider loading conditions which resemble the loading conditions a phantom would undergo in the experimental setup described in this thesis. To that end, consider the loading conditions of breast tissue in a mammogram.

The displacement field resulting from the uniform compression of the homogeneous

block of material is shown in Figure 5.1. The boundary conditions are:

$$u_x = \frac{1}{4}u_o \quad \text{on} \quad \Gamma^{a+}, \tag{5.2}$$

$$u_x = -\frac{1}{4}u_o \quad \text{on} \quad \Gamma^{a-}, \tag{5.3}$$

$$u_y = -u_o \quad \text{on} \quad \Gamma^{b+}, \tag{5.4}$$

$$u_y = 0 \quad \text{on} \quad \Gamma^{b-}, \tag{5.5}$$

$$u_z = \frac{1}{4}u_o \quad \text{on} \quad \Gamma^{c+}, \tag{5.6}$$

$$u_z = -\frac{1}{4}u_o \quad \text{on} \quad \Gamma^{c-}, \tag{5.7}$$

and zero shear stress on all the boundaries. For now, assume the block to be a cube with width L. The resulting strain field for this material with these boundary conditions is:

$$\epsilon_{yy} = -u_o/L, \tag{5.8}$$

$$\epsilon_{xx} = \epsilon_{zz} = \frac{u_o}{2L} \tag{5.9}$$

$$\text{and} \quad \epsilon_{ij} = 0 \quad \text{for} \quad i \neq j. \tag{5.10}$$

It may be easily verified that this strain distribution also satisfies traction free boundary conditions on all sides of the box, rather than prescribed displacements (i.e. $\mathbf{h} = 0$ on Γ^a and Γ^c). Now consider the question of uniqueness for this strain field. That is, can a modulus distribution, other than homogeneous, yield the same strain distribution with the same prescribed boundary conditions? Substituting this strain field into the curl of the momentum equations (2.5) leads to the following equations:

$$\partial_{xy}\mu = 0 \tag{5.11}$$

$$\text{and} \quad \partial_{yz}\mu = 0. \tag{5.12}$$

The general solution of these equations is

$$\mu(\mathbf{x}) = \mu_1(x, z) + \mu_2(y). \tag{5.13}$$

Here μ_1 and μ_2 are any arbitrary function of their arguments. It is clear that any modulus distribution which satisfies (5.13) will also yield an equivalent strain field. Thus the inverse problem for this strain field and boundary conditions has multiple solutions. The result does imply, however, that prior knowledge of the modulus distribution on an x-z surface and along a line in the y direction would ensure a unique solution for this strain field.
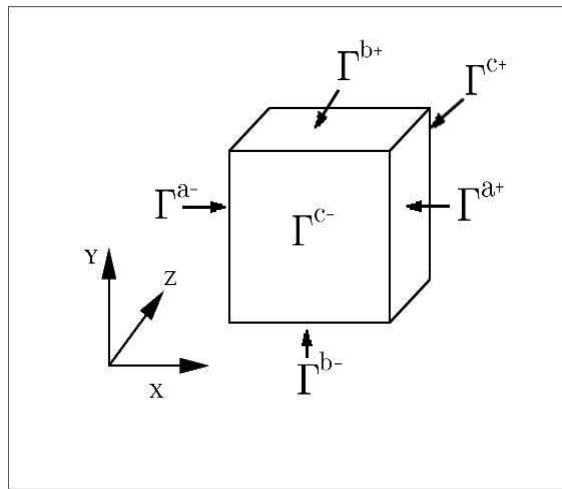
Figure 5.1: Block of incompressible elastic material with x boundaries: Γ^{a-} and Γ^{a+}, y boundaries: Γ^{b-} and Γ^{b+} and z boundaries: Γ^{c-} and Γ^{c+}.

5.2.2 Biaxial Stress

Now consider deforming the same cube of homogeneous material with boundary conditions:

$$u_x = \frac{1}{8}u_o \quad \text{on} \quad \Gamma^{\text{a}+}, \tag{5.14}$$

$$u_x = -\frac{1}{8}u_o \quad \text{on} \quad \Gamma^{\text{a}-}, \tag{5.15}$$

$$u_y = -u_o \quad \text{on} \quad \Gamma^{\text{b}+}, \tag{5.16}$$

$$u_y = 0 \quad \text{on} \quad \Gamma^{\text{b}-}, \tag{5.17}$$

$$u_z = \frac{3}{8}u_o \quad \text{on} \quad \Gamma^{\text{c}+}, \tag{5.18}$$

$$\text{and} \quad u_z = -\frac{3}{8}u_o \quad \text{on} \quad \Gamma^{\text{c}-}. \tag{5.19}$$

Again we apply zero shear stress on all the boundaries. The resulting strain field would be:

$$\epsilon_{xx} = \frac{u_o}{4L} \tag{5.20}$$

$$\epsilon_{yy} = -u_o/L, \tag{5.21}$$

$$\epsilon_{zz} = \frac{3u_o}{4L} \tag{5.22}$$

$$\text{and} \quad \epsilon_{ij} = 0 \quad \text{for} \quad i \neq j. \tag{5.23}$$

In the previous case, the stress was isotropic in the x-z plane. Here it is not. Again it can be verified that this strain distribution is consistent with traction free boundary conditions on two parallel sides of the box rather than prescribed displacements (i.e. $\mathbf{h} = 0$ on Γ^a or Γ^c). This strain field and the momentum equation imply:

$$\partial_{xz}\mu = 0 \tag{5.24}$$

$$\partial_{xy}\mu = 0 \tag{5.25}$$

$$\text{and} \quad \partial_{yz}\mu = 0. \tag{5.26}$$

These have the general solution:

$$\mu(\mathbf{x}) = \mu_1(x) + \mu_2(y) + \mu_3(z). \tag{5.27}$$

This shows that in addition to the homogeneous distribution which was used to create this strain field, any function μ which satisfies equation (5.27) would also yield the same strain field. This inverse problem, although still non-unique, demonstrates that application of applied deformations that avoid directional symmetries in $\boldsymbol{\epsilon}$ may help ensure the uniqueness of the solution.

5.2.3 Known Traction Boundary Conditions

A priori knowledge of applied traction boundary conditions can also help ensure the uniqueness of the solution. Suppose on some plane surface (e.g. Γ^c) it is known that $\mathbf{h} = \boldsymbol{\sigma} \cdot \mathbf{n} = \mathbf{0}$. The zero tractions on this surface implies:

$$\sigma_{xz} = \sigma_{yz} = \sigma_{zz} = 0 \quad \text{on} \quad \Gamma^c. \tag{5.28}$$

Using equation (5.28) in equation (2.2), just on the surface Γ^{c+}, yields:

$$p = 2\mu\epsilon_{zz}, \tag{5.29}$$

$$\epsilon_{xz} = \frac{\sigma_{xz}}{2\mu} = 0 \tag{5.30}$$

$$\text{and} \quad \epsilon_{yz} = \frac{\sigma_{yz}}{2\mu} = 0. \tag{5.31}$$

Substituting equations (5.29)-(5.31) into equation (2.5) to yield the equations:

$$-\partial_x(\mu\epsilon_{zz}) + \partial_x(\mu\epsilon_{xx}) + \partial_y(\mu\epsilon_{xy}) + \mu\partial_z\epsilon_{xz} = 0 \tag{5.32}$$

$$\text{and} \quad -\partial_y(\mu\epsilon_{zz}) + \partial_x(\mu\epsilon_{xy}) + \partial_y(\mu\epsilon_{yy}) + \mu\partial_z\epsilon_{yz} = 0. \tag{5.33}$$

These equations can be rewritten as the following partial differential equation for μ:

$$\hat{\nabla} \cdot (\mu \hat{\boldsymbol{\epsilon}}) + \mu \bar{\boldsymbol{\epsilon}} = \mathbf{0} \quad \text{on} \quad \Gamma^{c+} \tag{5.34}$$

$$\text{where} \quad \hat{\nabla} = \partial_x \mathbf{e}_x + \partial_y \mathbf{e}_y, \tag{5.35}$$

$$\hat{\boldsymbol{\epsilon}} = \begin{bmatrix} 2\epsilon_{xx} + \epsilon_{yy} & \epsilon_{xy} \\ \\ \epsilon_{xy} & \epsilon_{xx} + 2\epsilon_{yy} \end{bmatrix} \tag{5.36}$$

$$\text{and} \quad \bar{\boldsymbol{\epsilon}} = \begin{bmatrix} \partial_z \epsilon_{xz} \\ \\ \partial_z \epsilon_{yz} \end{bmatrix}. \tag{5.37}$$

Here the incompressibility constraint ($\epsilon_{ij} = 0$) was used to simplify the forms of $\hat{\boldsymbol{\epsilon}}$. Equation (5.34) may be solved by introducing the scaler function $q = \log \mu$ ($\hat{\nabla} q = \hat{\nabla} \mu / \mu$). The resulting equation for q can be integrated directly to give:

$$q = \int_{\hat{\mathbf{x}}_0}^{\hat{\mathbf{x}}} \mathbf{f} \; d\Gamma^{c+} + q(\hat{\mathbf{x}}_0) \tag{5.38}$$

$$\text{where} \quad \mathbf{f} = \hat{\nabla} q = \hat{\boldsymbol{\epsilon}}^{-1} \left[\hat{\nabla} \cdot \hat{\boldsymbol{\epsilon}} + \bar{\boldsymbol{\epsilon}} \right] \tag{5.39}$$

$$\text{and} \quad \hat{\mathbf{x}} = x \, \mathbf{e}_x + y \, \mathbf{e}_y. \tag{5.40}$$

Here $\hat{\mathbf{x}}$ denotes the x and y location on the surface Γ^{c+}. Thus the equation for μ on this surface takes the form:

$$\mu(\hat{\mathbf{x}}) = \mu_o \exp \int_{\hat{\mathbf{x}}_0}^{\hat{\mathbf{x}}} \mathbf{f} \; d\Gamma^{c+} \quad \text{on} \quad \Gamma^{c+}. \tag{5.41}$$

Equation (5.41) implies that the modulus distribution on a traction free plane of this cube can be determined, uniquely, up to a multiplicative constant. Of course, to do so one must know in advance that the surface is traction free. Thus advance knowledge of the traction applied to any boundary of the object adds substantially to the information available to reconstruct the modulus distribution.

5.3 Sensitivity

Typically, uniqueness is examined using the original constitutive equations or the momentum equations, as in the previous section, and the concern is whether there are multiple problem solutions which could exist to yield the measured data in its entirety. However, the formulation of the inverse problem in this work leads to another, slightly different concern. The issue of sensitivity is examined separately from the issue of uniqueness in this work because it is an issue which arises from the discretized, variational iterative formulation of the problem. This issue of sensitivity can best be illustrated in the calculation of the gradient ($\mathbf{G}_B$). The relative magnitude of the gradient in a specific location within the domain, given a current guess of the modulus distribution, defines how strongly a change in the modulus in that area would affect the value of the functional. Ideally, the gradient calculations should be low for areas of the domain where the modulus closely matches that of the actual modulus values and high in magnitude in areas where there is a mismatch. In practice there are other reasons which can result in low magnitude gradients.

One such reason is the use of Dirichlet boundary conditions. On the surfaces of a reconstructed volume which necessitate prescribed displacements, or Dirichlet conditions, the value of the functional is exactly zero, regardless of the modulus distribution near those surfaces. Thus the resulting gradient calculations for the modulus values near those surfaces are relatively low. The discretization used in this thesis results in a gradient calculation for every element and no elements in these meshes contain nodes which all lie on a boundary surface. Therefore, even in the case where all boundaries of a reconstructed mesh require prescribed displacements, each gradient calculation will affect the functional through at least one nodal value of the predicted displacement. However, the sensitivity issue plays an increasing role as $\mathbf{x}$ approaches surfaces, edges and corners of the domain, respectively.

Additionally, the application of prescribed displacements to certain modulus distributions can result in a decreased sensitivity which propagates to the interior of a reconstructed

domain. This issue is of particular concern when the modulus distributions and the pre-scribed displacements result in spatial symmetries similar to those discussed in Section 5.2. This sensitivity issue can best be seen in the use of the stand-off layer, described in the examples of Chapter 4. Consider the modulus distribution of a stand-off layer and background material, neglecting the inclusion, with a contrast of 3 to 1 shown in Figure 5.2(a). The modulus distribution can be written in the form:

$$\mu(\mathbf{x}) = \mu(y). \tag{5.42}$$

This modulus distribution was used to create an artificial displacement field, as described in Chapter 4, and the "imaged" portion of this displacement field was used as input to an inverse problem with all Dirichlet Boundary conditions. The initial guess to these inverse problems is typically a homogeneous modulus distribution (i.e. $\mu(\mathbf{x}) = 1$). At this initial guess the displacement field generated by the forward problem ($\mathbf{u}_{hom}$) was compared to the displacement field generated when the stand-off layer is present ($\mathbf{u}_{so}$). Figure 5.2(b) shows the value of $(\mathbf{u}_{so} - \mathbf{u}_{hom})^2$ for a slice of the "imaged" volume. This figure illustrates that, although a difference in the resulting displacement field is seen on a portion of the volume, the difference quickly disappears in areas closest to the boundaries. The fact that this value is small leads to a relatively low sensitivity in most of the areas around the stand-off layer. The gradient of the functional at this initial guess was also calculated and its magnitude is shown in Figure 5.3.

To put Figures 5.2 and 5.3 in perspective, consider these same calculations, at the initial guess, for the reconstructions from a displacement field generated with a modulus dis-tribution which has an inclusion. Figures 5.5(a) and 5.5(b) show the value of $(\mathbf{u}_{ex} - \mathbf{u}_{hom})^2$ and the magnitude of the gradient, respectively, for this inverse problem. The function $\mathbf{u}_{ex}$ is the displacement field generated from the modulus distribution shown in Figure 4.3(a). In Figure 5.5(a) it is clear that the difference in the displacements is much larger in the areas around the inclusion than it is in and around the stand-off layer. As a result, the magnitude of the gradient is also larger near the inclusion. Note that the values of the
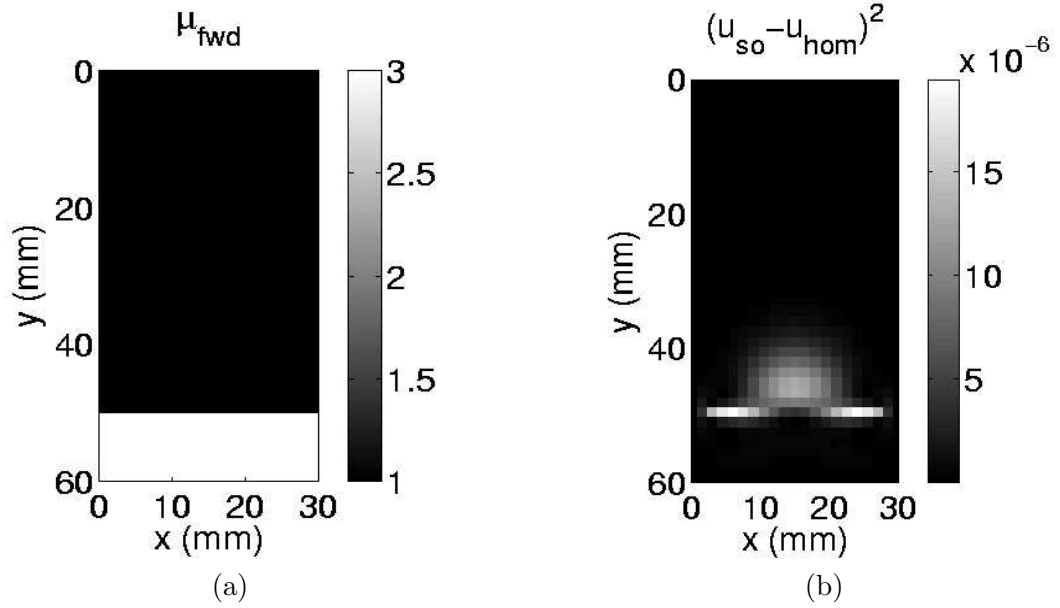
Figure 5.2: (a) The center x-y slice of the modulus distribution with a stand-off but no inclusion (μ_{fwd}). The area shown is the subset of the forward domain which lies in the reconstructed domain (Ω). (b) The center x-y slice of $(\mathbf{u}_{so} - \mathbf{u}_{hom})^2$ (in mm^2) at the initial guess.
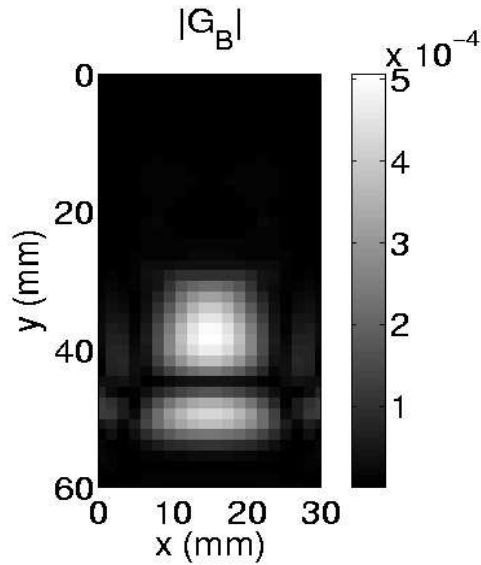

Figure 5.3: The center x-y slice of the magnitude of the gradient for the stand-off layer example at the initial guess.
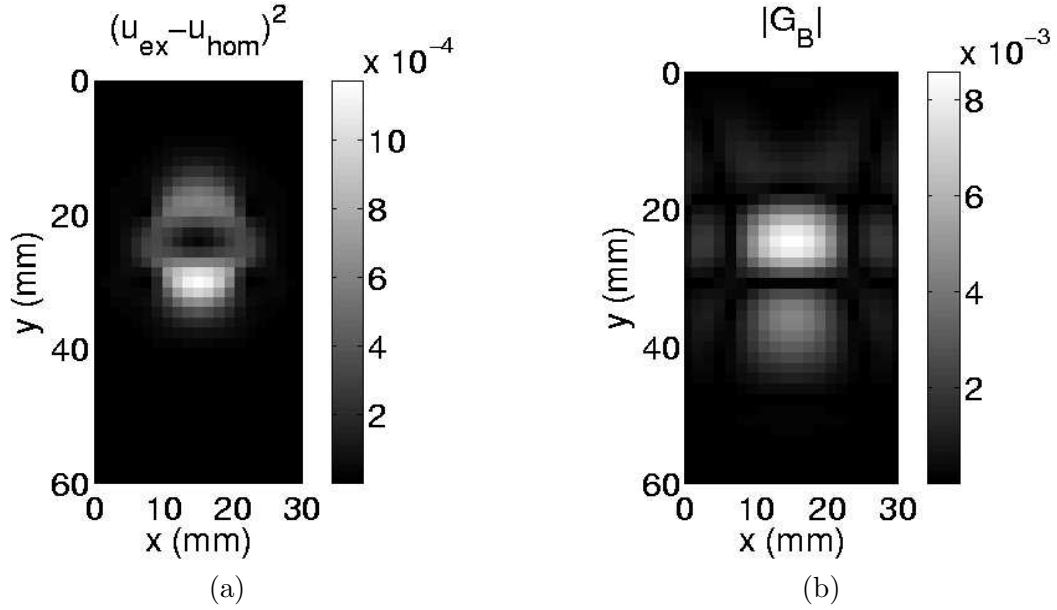
Figure 5.4: (a) The center x-y slice of $(\mathbf{u}_{ex} - \mathbf{u}_{hom})^2$ (in mm^2) at the initial guess. (b) The center x-y slice of the magnitude of the gradient for the inclusion and stand-off layer example at the initial guess.

displacement difference and the gradients differ by orders of magnitude in the case with the inclusion as compared to the case without.

It is also important to show how the zero traction assumption described for the second reconstruction of Section 4.3.2 improves the sensitivity in the stand-off layer. To that end, the value of $(\mathbf{u}_{ex} - \mathbf{u}_{hom})^2$ and the magnitude of the gradient are also calculated at a homogeneous initial guess for a reconstruction with the boundary conditions described in Section 4.3.2. Figures 5.5(a) and 5.5(b) show these values. Note that the overall magnitude of the functional value increases from the previous example and the magnitude of the gradient improves around the inclusion and in the stand-off layer.

The issue of sensitivity can also be seen in the plots of Figures 4.4(a), 4.4(b), 4.6(a) and 4.6(b). It is clear in both reconstructions types that, after the value of the reconstructed modulus distribution reaches a certain iteration, relatively large changes in the modulus have little effect in the resulting functional value. In all of these examples there was no noise in the reconstructions. In Section 4.3.3 noise was added to the displacements. At these
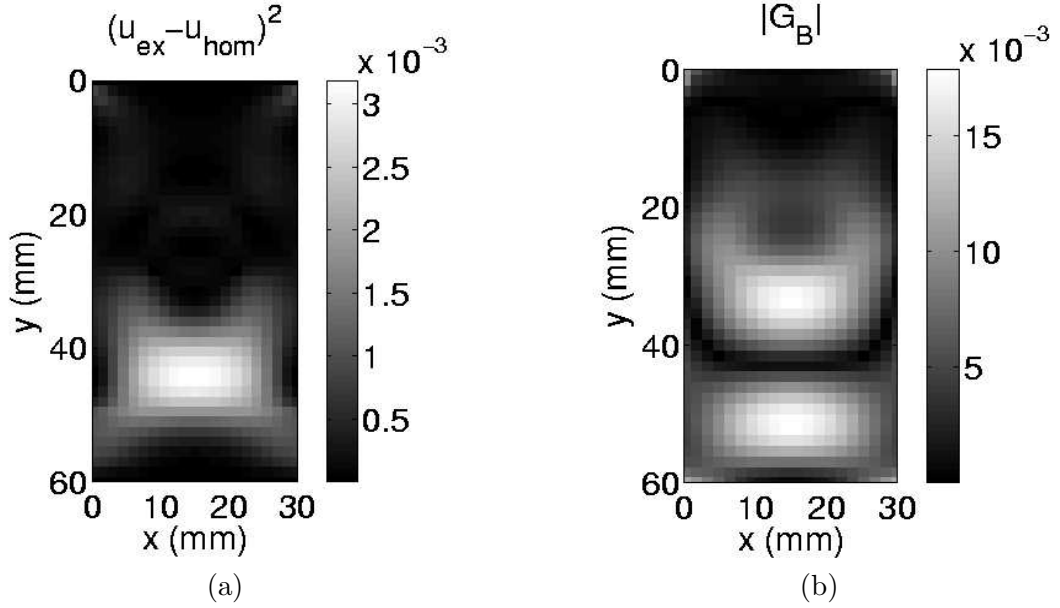
Figure 5.5: (a) The center x-y slice of $(\mathbf{u}_{ex} - \mathbf{u}_{hom})^2$ (in mm^2) at the initial guess for the second reconstruction type. (b) The center x-y slice of the magnitude of the gradient for the inclusion and stand-off layer example at the initial guess for the second reconstruction type.

noise levels the magnitude of $(displacement\,noise)^2$ would be approximately $10^{-5}mm^2$ for a given location in the reconstructed domain. Thus the gradient calculation would also include a noise component as well as a regularization contribution.

Finally, it is also worth investigating how the issues of sensitivity, for all displacement boundary conditions could affect the reconstructions of geometries other than that of the stand-off layer. To that end, another artificial phantom and simulated displacements were created. The inclusion geometry of this phantom was such that the boundary of the reconstructed domain passed through the inclusion. That is some of the inclusion falls in the domain Ω and some does not. Figure 5.6 shows a central slice through the modulus distribution of used to create the artificial displacements. The contrast of the inclusion and stand-off layer relative to the background is 3 to 1 everywhere in this distribution. The darker region of this figure indicates the domain of the reconstruction. The displacements within this domain were then input to the reconstruction algorithm to recover the modulus distribution. There was no noise or regularization in this study. The boundary conditions
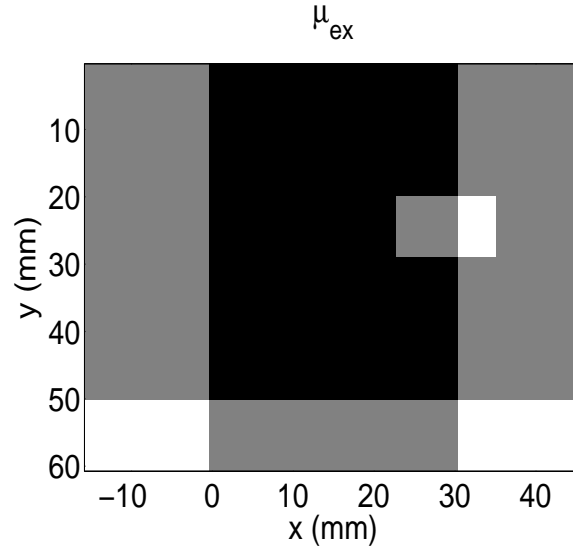
Figure 5.6: An x-y slice of the forward modulus distribution, μ_{ex}, created to investigate the impact of sensitivity on inclusion geometries. The contrast of the inclusion and stand-off layer relative to the background is 3 to 1 everywhere in this distribution (The darker region signifies the reconstruction domain Ω).

in this example were all Dirichlet. All other relevant parameters were consistent with the example reconstructions in Chapter 4. Figure 5.7(a) shows a slice of the reconstructed modulus distribution. Notice the decreased modulus value at the edge of the reconstructed domain. This can also be seen in Figure 5.7(b), which shows a line of the reconstruction through the center of the inclusion in the x direction. It should be noted that, although the reconstructed modulus does decrease near the boundary of the reconstruction, the overall effect is far less prominent than in the case of the stand-off layer geometry.
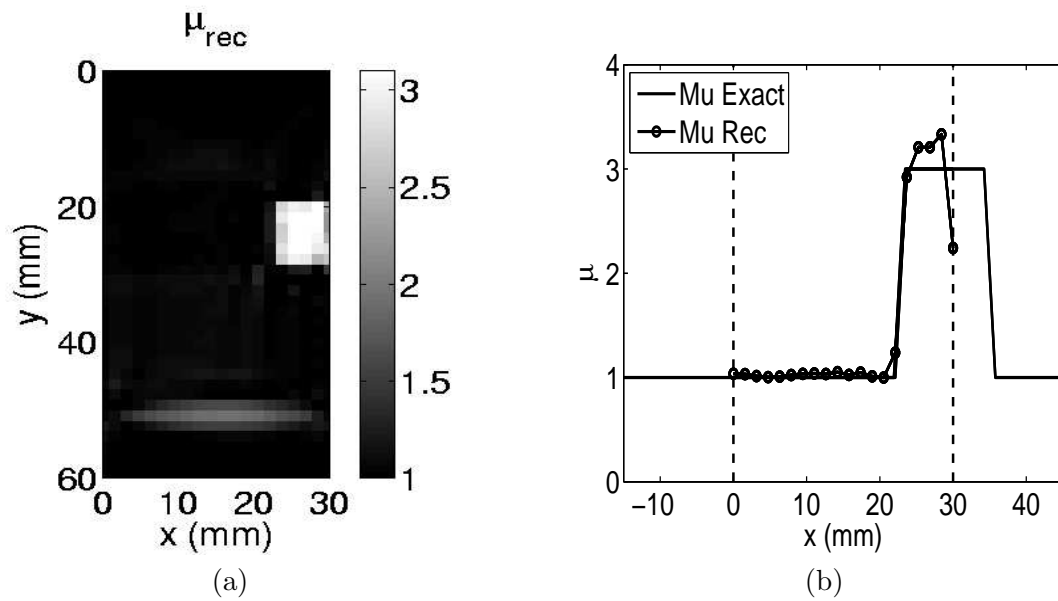
Figure 5.7: (a) An x-y slice of the reconstructed modulus image through the center of the inclusion. (b) Lines of the reconstructed (μ_{rec}) and exact (μ_{ex}) modulus distributions from the inclusion sensitivity study through the inclusion in the x direction (the dotted lines represent the boundaries of the reconstructed domain.

Chapter 6

Ultrasound Elasticity Imaging: Accuracy Study

6.1 Introduction

In the previous two sections, methods to measure displacements from image pairs and subsequently use the measured displacements to reconstruct a shear elastic modulus were presented. Additionally the sources of noise for the ultrasound imaging system were identified and, where possible, quantified. The accuracy of the resulting modulus reconstruction cannot be quantified unless a study with actual images, similar to those seen in a clinical setting, is performed. To that end, ultrasound phantoms were created which mimic the acoustic properties of real tissue. The phantom elastic modulus can be locally and independently controlled. This chapter will give a brief introduction of US imaging, discuss the creation of these phantoms and the protocol used to image them. Section 6.4 presents the results of a study designed to quantify the accuracy and limitations of these algorithms using ultrasound images of the tissue mimicking phantoms. The last section of this chapter is the discussion.

6.1.1 Ultrasound Imaging: Background

Ultrasound is an inexpensive, non ionizing imaging modality commonly used in diagnostic investigations. Ultrasound radiation is high frequency sound pulses which are transmitted through the body. The image information is contained in the scattered and reflected sound field measured at the tissue boundaries. Typically, for clinical ultrasound scanners, the transmitted and received sound field are created and measured in the same location on the tissue's surface. Knowing that the sound speed in soft tissue is approxi-

mately constant ($\approx 1540.0\,m/s$) (Goss et al., 1978), the time at which the pulse echo is recorded relative to the time at which it was sent can be used to find the distance the reflected wave traveled. The intensity of the recorded sound echo wave at any point in time is directly related to the tissue's reflectivity. Sound is reflected by impedance discontinuities in the imaged media (e.g. tissue boundaries, tissue micro structure, bubbles, etc.). Thus, the echos received from a single pulse can be used to create a spatial mapping of the reflectivity of the tissue in the area permeated by that wave.

Some important advantages of ultrasound are its high signal to noise ratio and its high resolution in the direction of sound propagation. All biological media attenuates ultrasound. The attenuation depends largely on the frequency of the ultrasound, increasing as the frequency increases (the frequencies used for diagnostic ultrasound are typically in the 1-15 MHz range). As a result of this, the wave signal intensity decreases exponentially from the source and can lead to heating of the tissue. The resolution of the system is also related to the ultrasound frequency. A system with a relatively high frequency transducer would have a high resolution. The magnitude of the resolution is approximately the same as the speed of sound in water divided by the center frequency used to create the image. Thus, there is a tradeoff between image penetration depth and resolution.

Figure 6.1(a) shows the ultrasound system and transducer used in this work for imaging tissue and tissue phantoms. Most clinical ultrasound machines will perform filtering and signal enveloping prior to displaying the image (B-mode). The system used in this thesis allows access to the unaltered radio frequency (RF) data. Figure 6.1 shows a B-mode image taken from an automated sonographic examination of a breast with a benign cyst (Bassett and Kimme-Smith, 1991). In this image the cystic tissue appears darker than the rest of the breast tissue, but often tumors will show no contrast to the surrounding tissue (Bassett and Kimme-Smith, 1991). The spotted nature of the ultrasound image is known as speckle. Speckle results from the collective interference and coherence of the waves reflecting from small, densely populated sound scatterers characteristic of soft tissue. It is the speckle in the ultrasound images that will be the defining influence on the ability to
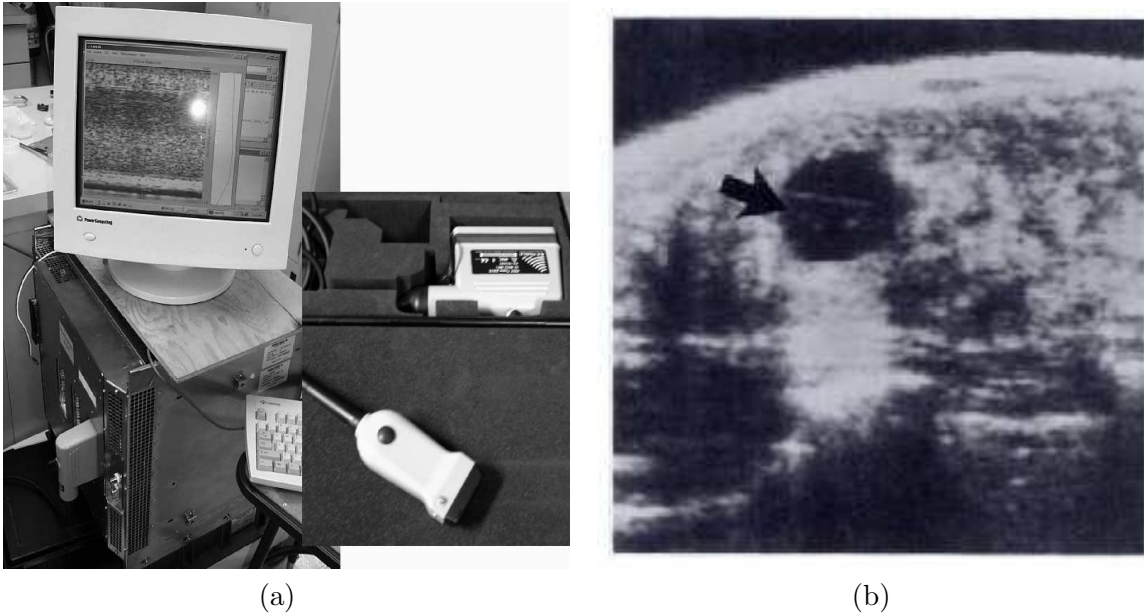
Figure 6.1: (a) Ultrasound system and transducer. (b) Ultrasound image of breast cyst (Adapted from Bassett and Kimme-Smith, 1991).

measure the displacements.

6.2 Phantom Construction

One of the important tools that researchers use in medical imaging is a tissue mimicking phantom. A phantom is usually an object or substance whose relevant physical parameters closely match those of the tissue of interest. Most of the experimental validations of the algorithms discussed in this thesis will be done using tissue phantoms. Currently, there is an abundance of research investigating optimal methods for creating ultrasound imaging phantoms (Homolka et al., 2002; Polletti et al., 2002; Rownd et al., 1997). There is little work published, however, regarding tissue phantoms made specifically for elasticity imaging (Hall et al., 1996). The first consideration when developing a tissue mimicking phantom recipe is to allow the tailoring of both the elastic properties and the modality specific properties. This was achieved by using a gelatin base because its elastic properties closely resemble those of soft tissues. The gelatin stiffness can also be modified by varying

Figure 6.2: Ultrasound tissue mimicking phantom.

the concentration of the solution. Much like soft tissue, gelatin phantoms contain a high percentage of water. Thus the sound speed and acoustic attenuation closely match that of breast tissue.

The ultrasound phantoms were a mixture of gelatin and silica. The silica particles were suspended in the gelatin as scatterers to reproduce the full speckle image normally seen when imaging soft tissue. The phantoms were cuboid in shape with a base of $60mm \times 60mm$ and a height of $40mm$. In the center of the phantom, cylindrical inclusions were made to mimic the relative stiffness of tumors compared to healthy tissue. Prior to letting any phantom material set, all ingredients were degassed as a mixture so that no air bubbles were present. This was done to avoid any mechanical or acoustic inconsistencies. A stiff stand-off layer was created on top or bottom of the phantom with a gelatin concentration matching that of the inclusion. It may be necessary, when establishing an imaging protocol, to include a stand-off layer with known mechanical properties in the images to provide a calibration for the underlying tissue properties. A picture of the phantom is shown in figure 6.2.
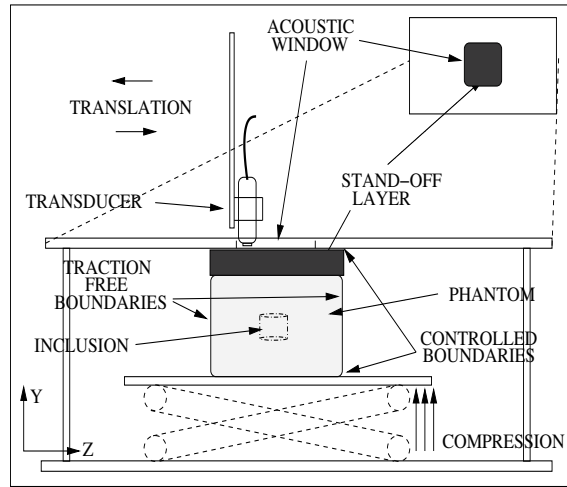
Figure 6.3: Three dimensional ultrasound imaging setup.

6.3 Imaging Protocol

The experimental setup for the three dimensional ultrasound experiments was developed using a two dimensional ultrasound scanner (Analogic AN2300). The transducer is a $12\,MHz$ linear array with 192 piezoelectric elements in the lateral (x) direction. The phantom and stand-off layer were held in place by two plates on the bottom and top. The top plate has a square window where the transducer is scanned and the phantom is imaged. A schematic of the ultrasound setup is shown in Figure 6.3(a). The transducer was scanned in the elevation (z) direction such that the resolution was approximately the same as in the lateral direction. The transducer was scanned using a Newport stepper motor with micrometer accuracy. Water was used as an acoustic coupling medium between the transducer and the phantom. The resulting ultrasound images have a voxel size of about $19.2\mu m \times 158\mu m \times 140\mu m$ and image dimensions of about $3000 \times 192 \times 192$ pixels in the axial (y), lateral and elevation directions, respectively.

In a typical imaging experiment, the phantom is first placed between the plates and a slight compression is applied to hold it in place. The coupling medium is placed in the acoustic window and then a pre deformation image is taken. Image acquisition typ-

ically takes several minutes, however, the process has not yet been optimized for time. After the first image is taken, a small compressive strain is applied (typically $\sim$ 1-2%), and then a second post deformation image is taken. The setup described in figure 6.3(a) also allows for shear deformations, if additional images or displacement fields are necessary.

6.4   Accuracy Study

In order to evaluate the accuracy and limitations of the algorithms outlined in this thesis, phantoms were created with various sizes and contrasts. The phantoms were created and imaged using the protocol described in the previous sections of this chapter. The sizes of the inclusions were varied by changing the size of the mold used to pour the gelatin. The contrast was varied by varying the gelatin concentration used to create the inclusions (lower gelatin concentration yields lower shear modulus). A stand-off layer was included in each case and is typically made to approximately match the modulus value of the inclusion.

For each batch of gelatin used in each phantom, separate calibration samples were made to test the modulus value independently from the imaging measurements. The calibration samples created were cylindrical with a height of $10mm$ and a diameter of $15mm$. Typically 5 calibration samples were made of each gelatin batch for each phantom made. The stiffness of the calibration samples was measured using a TA Instruments Q800 Dynamic Mechanical Analysis machine. To determine the elastic modulus, a compression test was used to measure the force/displacement relationship of each sample in the range of 1-10% strain. The compression test necessitated the use of no slip boundary conditions on the top and bottom of each sample tested. These boundary conditions resulted in a nonuniform stress field in the gelatin samples. Therefore, the Young's modulus taken to be the slope of the linear stress/strain relation times some compensatory factor which relates the slope of the stress/strain relation for a compression test with no slip boundaries and the actual Young's modulus of the material. This factor was found using a finite element analysis program (FlexPDE), for the sample geometry described above, by comparing the

resulting slopes of the stress/strain curve of a material with a given modulus undergoing a compression test. The ratio of the true Young's modulus to the slope of the stress/strain curve gives this compensatory factor. Its value was found to be:

$$\frac{E_{apparent}}{E_{true}} = 1.34 \pm 0.01 \qquad (6.1)$$

Here, $E_{apparent} = F/(area * strain)$ is the apparent Young's modulus (as if the sample had slip boundary conditions). E_{true} is the actual Young's modulus for the material. For an incompressible material the shear modulus is $\mu = \frac{1}{3}E$. For each set of samples tested the mean and standard deviation of the compensated Young's modulus is reported (E_{true}).

To review, for each reconstructed modulus image, the pre and post images of a compression experiment with approximately 1-2% applied strain were used to measure the tissue displacements in the imaged volume. For each phantom image the displacement was measured with a finite element size of approximately $1mm$ in the y direction and $0.6mm$ in the x and z directions, resulting in 40x60x40 elements in the x, y and z directions, respectively. The regularization and incompressibility parameters used were $\alpha_1 = 1 \times 10^8$ and $\alpha_2 = 1 \times 10^{10}$, respectively. To determine the termination point of the displacement matching iterations, the normalized L^2 norm of the images $\left(\int (I_1 - I_2)^2 \, d\Omega_e / \sqrt{\int (I_1)^2 \, d\Omega_e \int (I_2)^2 \, d\Omega_e} \right)$ was calculated for each element at each iteration. When this value was found to be relatively homogeneous in $\mathbf{x}$ and less than 0.2, the algorithm was allowed to iterate 26 additional times to ensure that it had converged. The L^2 norm value of 0.2 would correspond to a peak cross correlation value of approximately 0.9. Experience has shown that values higher than 0.2 typically indicate regions which are stuck in local minima. The measured displacements were then input to the inverse algorithm with approximated traction free boundary conditions discussed in Chapter 4 and a Poisson's ratio of 0.4995. A TVD regularization for all inversion reconstructions was used with a parameter $\alpha = 10^{-4}$. The initial guess of μ was homogeneous with value 1 and the iterations were terminated at first iteration n for which the value $(\pi(\mu^{n-5}) - \pi(\mu^n))/\pi(\mu^{n-5}) < 0.01$. The functional value used to determine the stopping criterion was the displacement matching term alone, without the

regularization.

In each of the following reconstructions, three dimensional slices of the modulus distribution are shown in the x-y plane and the x-z plane through the center of the inclusion. In addition, the x-y slice of the recovered modulus image is shown next to an image of the axial strain (ϵ_{yy}). The axial strain image is created from a finite difference differentiation of the axial displacement. The axial displacement is smoothed prior to differentiation with a box convolution kernel of size 3^3 finite element voxels to smooth the resulting strain image.

6.4.1   Inclusion One

The first inclusion imaged was created to approximate the size of a typical tumor diagnosed by palpation or screening mammography. The inclusion size was $12.77mm$ in diameter and $10mm$ in height. The background was made with an 8% by mass concentration of gelatin and the inclusion and stand-off layer were made with a 16% by mass concentration of gelatin. The stand-off was positioned at the top of the phantom when imaged for this reconstruction. The independently measured values of the Young's modulus were $0.020 \pm 0.0013\,MPa$ for the background and $0.0648 \pm 0.0037\,MPa$ for the inclusion and stand-off layer. To evaluate the recovered contrast and size in the reconstructions, the half maximum of the inclusion modulus was determined by inspection. The average modulus in those elements above the half maximum is then considered to be the recovered inclusion modulus value. It is noted that this averaging systematically lowers the estimate of the inclusion stiffness. Similarly, the modulus contrast in the stand-off is calculated as the average above the half maximum of the stand-off region. The background modulus value was determined by averaging a relatively homogeneous portion of the background adjacent to the inclusion. For this reconstruction the recovered inclusion modulus value is 2.2441 ± 0.2262 to a background modulus value of 1.0046 ± 0.0145. The average stand-off modulus value is 1.7457 ± 0.2190. The volume of the inclusion is found by counting the number of voxel elements which have modulus values greater than the half maximum and
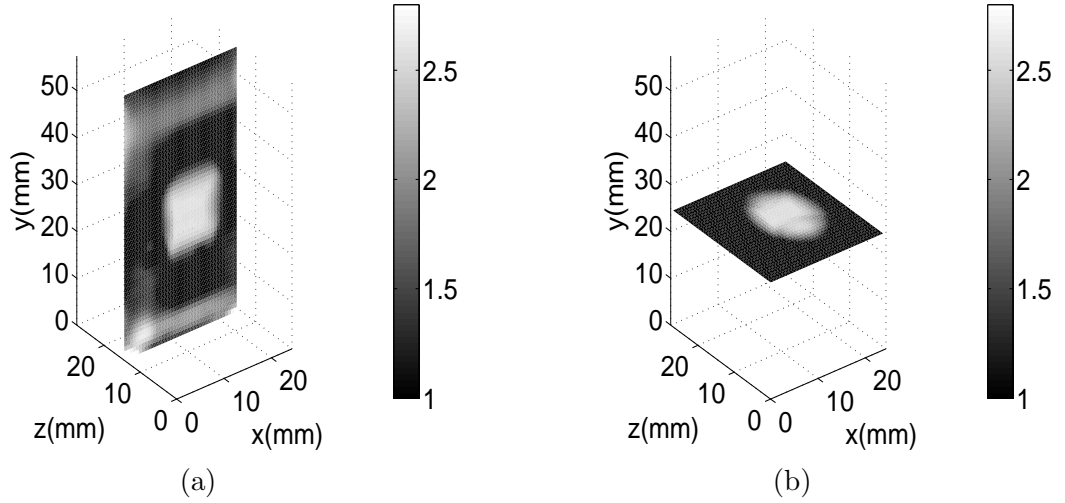
Figure 6.4: (a) x-y slice of 3D modulus reconstruction for a large inclusion with a 16% by mass gelatin concentration through the center of the inclusion. (b) x-z slice of 3D modulus reconstruction for this same inclusion through the center of the inclusion.

multiplying by the volume of the voxel. The size of the reconstructed stand-off layer is not reported due to the artifacts obstructing its proper reconstruction. For this reconstruction, the inclusion volume was $1.6879cm^3$ compared to the reference volume of $1.2808cm^3$.

Using the axial strain field, created from the measured displacements, a value of the average strain in the inclusion and in a homogeneous portion of the background were also calculated. For this reconstruction the strain in the inclusion and in the background were -0.0129 ± 0.0010 and -0.0202 ± 0.0003, respectively. Figures 6.4(a) and (b) show the 3D reconstructed modulus images in the x-y plane and the x-z plane sliced through the center of the inclusion. Figures 6.5(a) and (b) show the x-y slice of the reconstructed modulus image next to the same slice of the axial strain image (ϵ_{yy}). Figure 6.6 shows an axial line of the modulus distribution through the center of the inclusion.
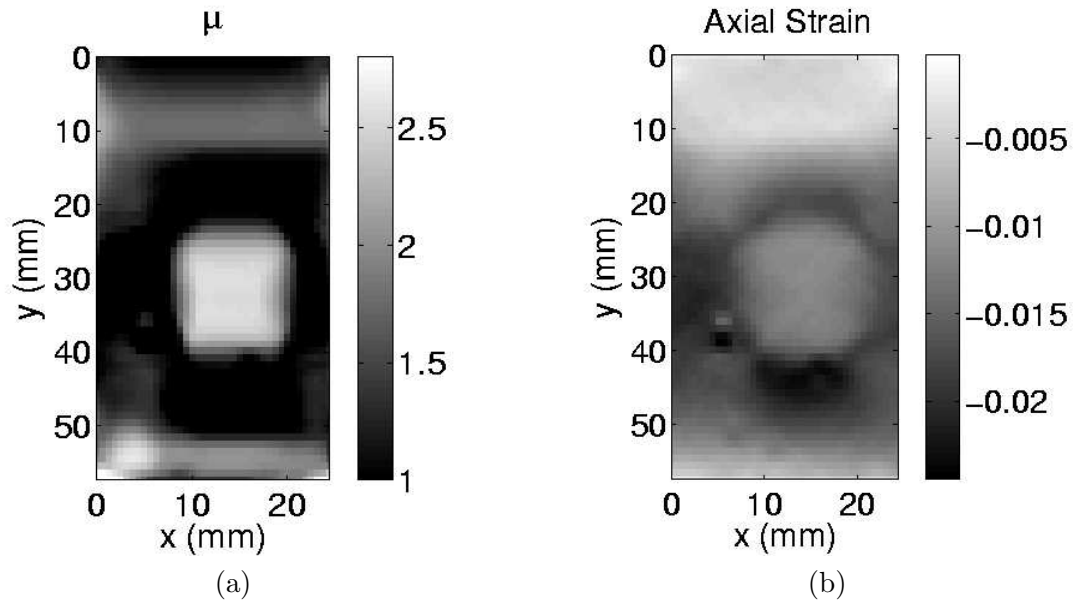
Figure 6.5: (a) x-y slice of modulus reconstruction for a large inclusion with a 16% by mass gelatin concentration. (b) x-y slice of the axial strain (ϵ_{yy}) for this same inclusion.
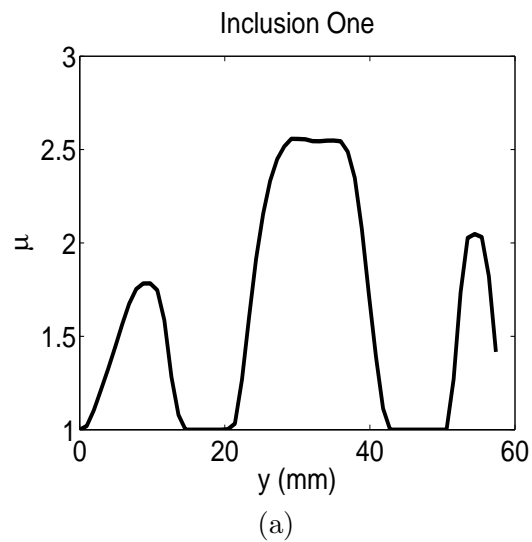
Figure 6.6: Axial line of the modulus distribution for a large inclusion with a 16% by mass gelatin concentration.

6.4.2 Inclusion Two

The second inclusion imaged was created to investigate the algorithm's accuracy as the inclusion size decreases. The inclusion size was $7.94mm$ in diameter and $7.94mm$ in height. The background was made with an 8% by mass concentration of gelatin and the inclusion and stand-off layer were made with a 16% by mass concentration of gelatin. The stand-off was positioned at the top of the phantom when imaged for this reconstruction. The independently measured values of the Young's modulus were $0.0200 \pm 0.0013 \, MPa$ for the background and $0.0648 \pm 0.0037 \, MPa$ for the inclusion and stand-off layer. For this reconstruction the recovered inclusion modulus value is 2.0892 ± 0.2029 to a background modulus value of 1.0001 ± 0.0003. The average stand-off modulus value is 1.6967 ± 0.1388. For this reconstruction the inclusion volume was $0.4573 cm^3$ compared to a reference volume of $0.3931 cm^3$. The average strain in the inclusion and in the background was -0.0134 ± 0.0013 and -0.0172 ± 0.0017, respectively. Figures 6.7(a) and (b) show the 3D reconstructed modulus images in the x-y plane and the x-z plane sliced through the center of this inclusion. Figures 6.8(a) and (b) show the x-y slice of the reconstructed modulus image next to the same slice of the axial strain image (ϵ_{yy}). Figure 6.9 shows an axial line of the modulus distribution through the center of the inclusion.

6.4.3 Inclusion Three

The third inclusion imaged was created to further investigate the algorithm's accuracy as the inclusion size decreases. The inclusion size was made to be $4.80mm$ in diameter and $4.80mm$ in height. The background was made with an 8% by mass concentration of gelatin and the inclusion and stand-off layer were made with a 16% by mass concentration of gelatin. The stand-off was positioned at the bottom of the phantom when imaged for this reconstruction. The independently measured values of the Young's modulus were $0.0228 \pm 0.0011 \, MPa$ for the background and $0.0584 \pm 0.0027 \, MPa$ for the inclusion and stand-off layer. For this reconstruction the recovered inclusion modulus value is 2.1005 ± 0.2096 to
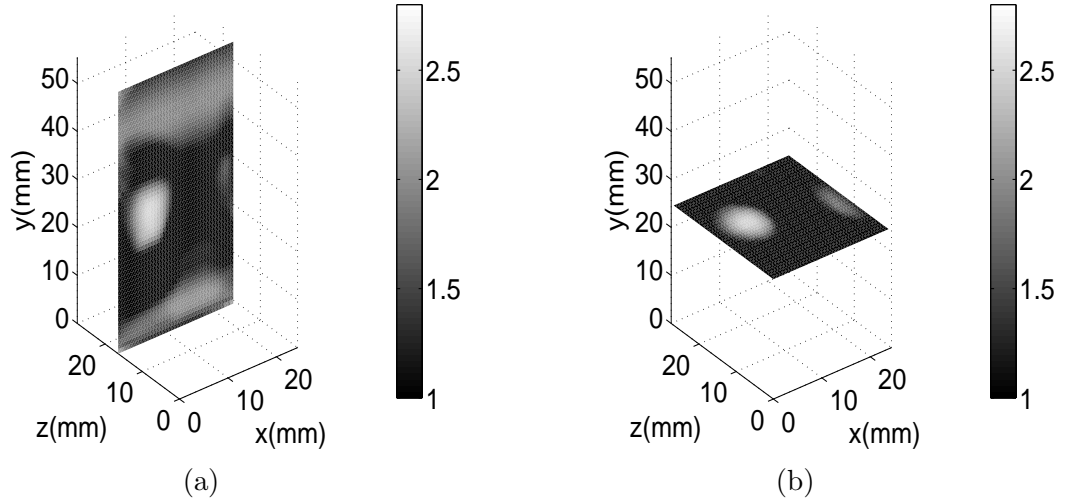
Figure 6.7: (a) *x-y* slice of 3D modulus reconstruction for a medium sized inclusion with a 16% by mass gelatin concentration through the center of the inclusion. (b) *x-z* slice of 3D modulus reconstruction for this same inclusion through the center of the inclusion.
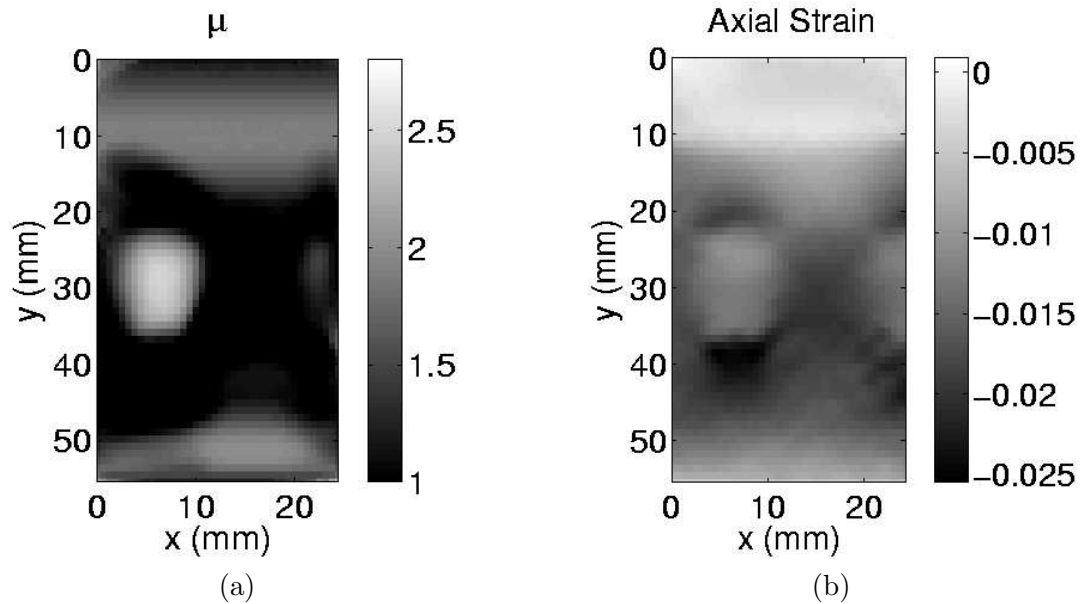

Figure 6.8: (a) *x-y* slice of modulus reconstruction for a medium sized inclusion with a 16% by mass gelatin concentration. (b) *x-y* slice of the axial strain (ϵ_{yy}) for this same inclusion.
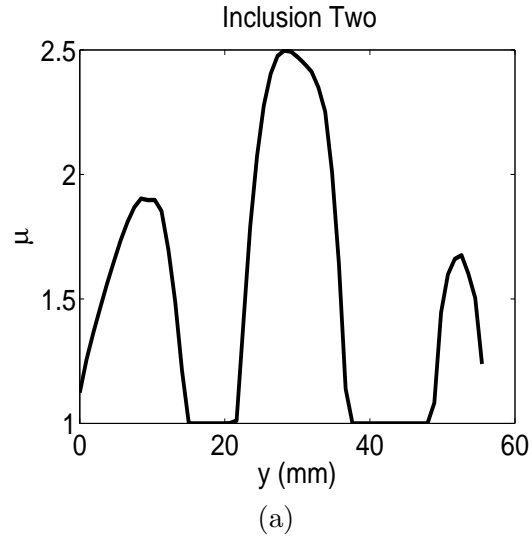
Figure 6.9: Axial line of the modulus distribution for a medium sized inclusion with a 16% by mass gelatin concentration.

a background modulus value of 1.0045 ± 0.0148. The average stand-off modulus value is 2.7908 ± 0.3761. For this reconstruction the inclusion volume was $0.0960 cm^3$ compared to a reference volume of $0.0869 cm^3$. The average strain in the inclusion and in the background was -0.0153 ± 0.0017 and -0.0193 ± 0.0020, respectively. Figures 6.10(a) and (b) show the 3D reconstructed modulus images in the x-y plane and the x-z plane sliced through the center of the inclusion. Figures 6.11(a) and (b) show the x-y slice of the reconstructed modulus image next to the same slice of the axial strain image (ϵ_{yy}). Figure 6.12 shows an axial line of the modulus distribution through the center of the inclusion.

6.4.4 Inclusion Four

The fourth inclusion imaged was created to investigate the algorithm's accuracy as the inclusion contrast relative to the background decreases. The inclusion size was $7.94mm$ in diameter and $7.94mm$ in height. The background was made with an 8% by mass concentration of gelatin and the inclusion and stand-off layer were made with a 12% by mass concentration of gelatin. The stand-off was positioned at the bottom of the phantom
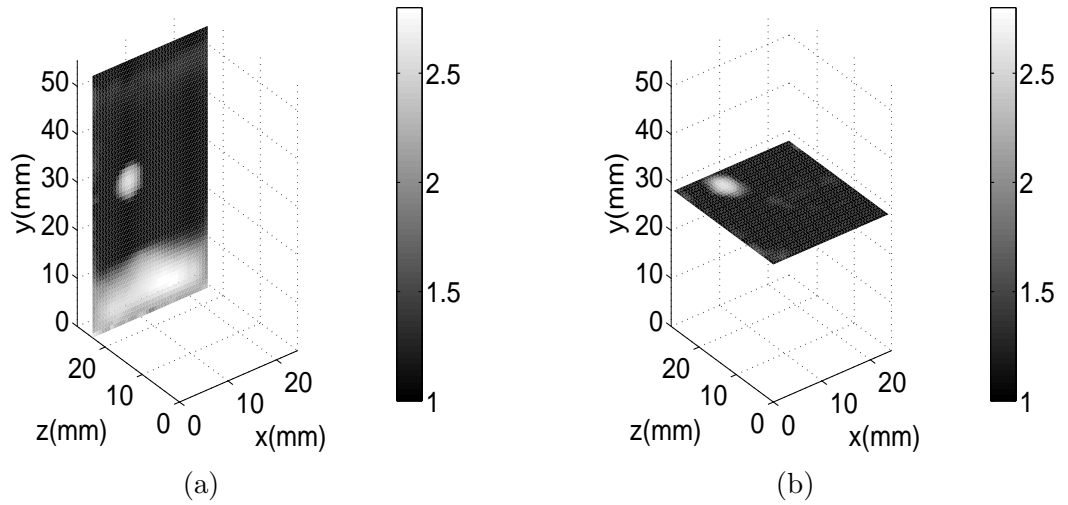
Figure 6.10: (a) x-y slice of 3D modulus reconstruction for a small inclusion with a 16% by mass gelatin concentration through the center of the inclusion. (b) x-z slice of 3D modulus reconstruction for this same inclusion through the center of the inclusion.
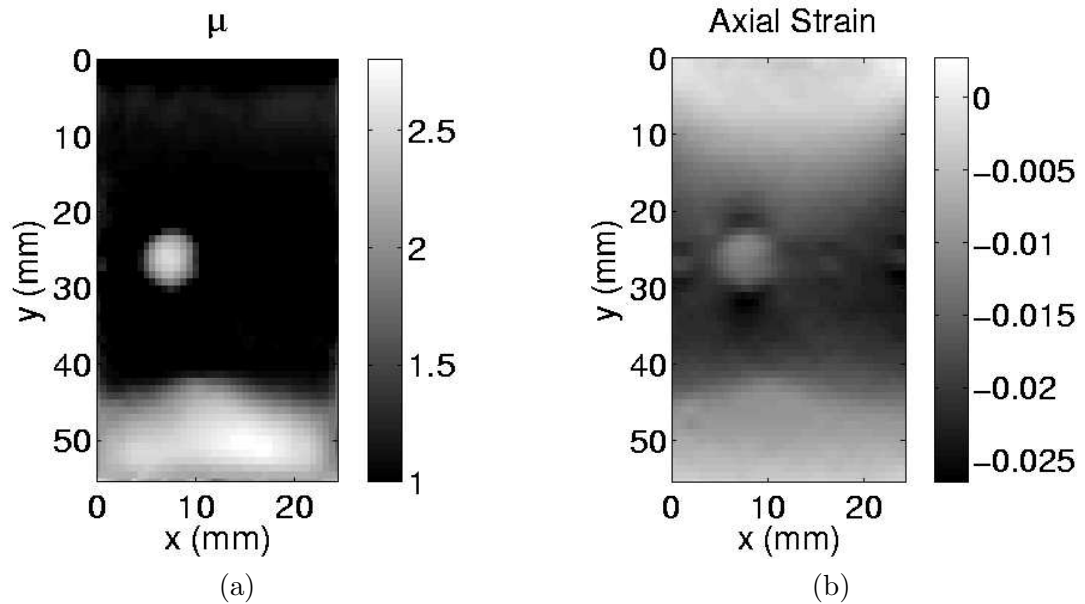

Figure 6.11: (a) x-y slice of modulus reconstruction for a small inclusion with a 16% by mass gelatin concentration. (b) x-y slice of the axial strain (ϵ_{yy}) for this same inclusion.
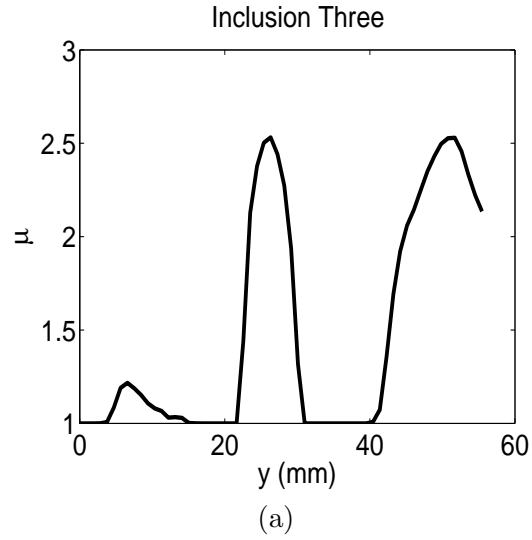
Inclusion Three

(a)

Figure 6.12: Axial line of the modulus distribution for a small inclusion with a 16% by mass gelatin concentration.

when imaged for this reconstruction. The independently measured values of the Young's modulus were $0.0193 \pm 0.0018\,MPa$ for the background and $0.0387 \pm 0.0020\,MPa$ for the inclusion and stand-off layer. For this reconstruction the recovered inclusion modulus value is 1.6145 ± 0.1214 to a background modulus value of 1.0022 ± 0.0083. The average stand-off modulus value is 1.9597 ± 0.2660. For this reconstruction the inclusion volume was $0.3271cm^3$ compared to a reference volume of $0.3931cm^3$. The average strain in the inclusion and in the background was -0.0104 ± 0.0008 and -0.0136 ± 0.0015, respectively. Figures 6.13(a) and (b) show the 3D reconstructed modulus images in the x-y plane and the x-z plane sliced through the center of the inclusion. Figures 6.14(a) and (b) show the x-y slice of the reconstructed modulus image next to the same slice of the axial strain image (ϵ_{yy}). Figure 6.15 shows an axial line of the modulus distribution through the center of the inclusion.
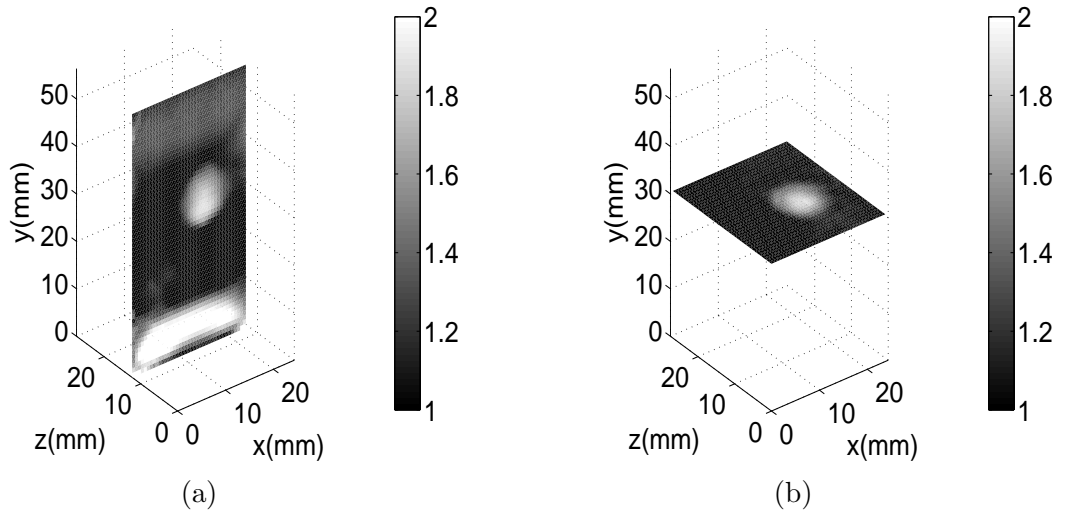
Figure 6.13: (a) *x-y* slice of 3D modulus reconstruction for a large inclusion with a 12% by mass gelatin concentration through the center of the inclusion. (b) *x-z* slice of 3D modulus reconstruction for this same inclusion through the center of the inclusion.
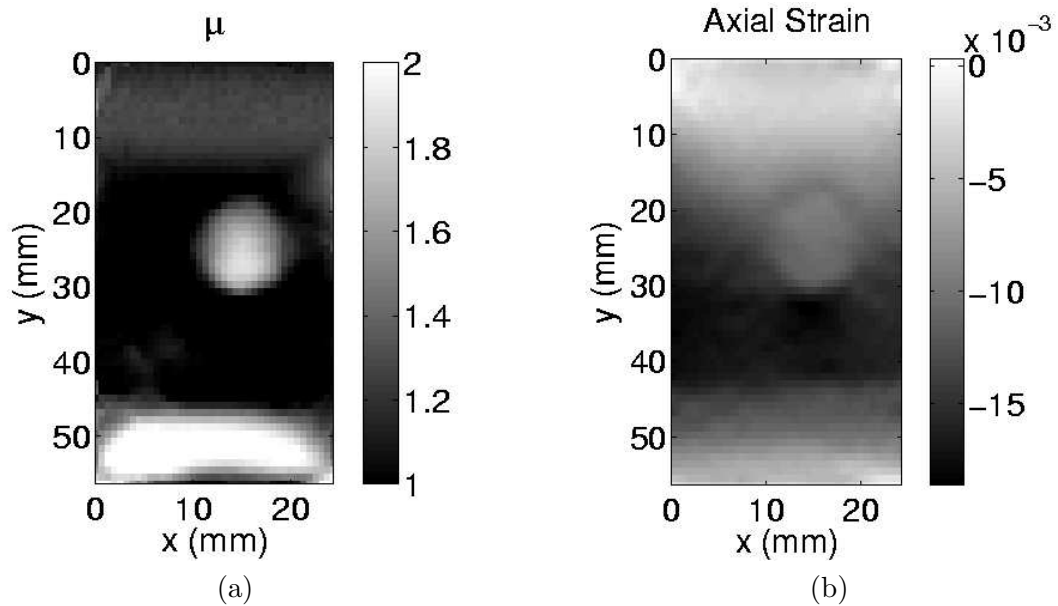

Figure 6.14: (a) *x-y* slice of modulus reconstruction for a medium sized inclusion with a 12% by mass gelatin concentration. (b) *x-y* slice of the axial strain (ϵ_{yy}) for this same inclusion.
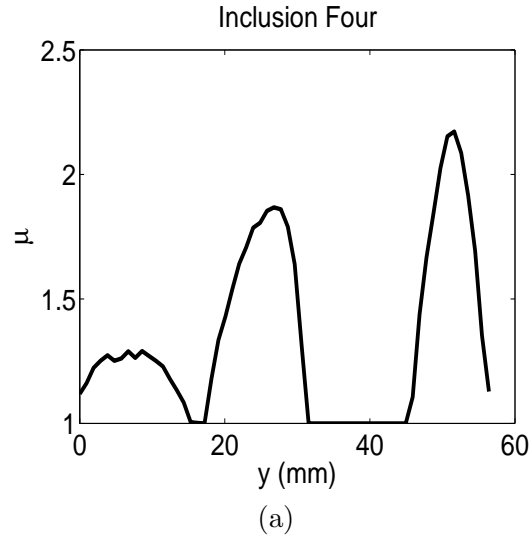
Inclusion Four

(a)

Figure 6.15: Axial line of the modulus distribution for a medium sized inclusion with a 12% by mass gelatin concentration.

6.4.5   Inclusion Five

The fifth inclusion imaged was a smaller inclusion than in the previous section, but at the same contrast. The inclusion size was made to be $4.80mm$ in diameter and $4.80mm$ in height. The background was made with an 8% by mass concentration of gelatin and the inclusion was made with a 12% by mass concentration of gelatin. The stand-off in this phantom was made with a 16% by mass concentration of gelatin and was positioned at the bottom of the phantom when imaged for this reconstruction. The independently measured values of the Young's modulus were $0.0228 \pm 0.0011\,MPa$ for the background, $0.0431\pm0.0012\,MPa$ for the inclusion and $0.0584\pm0.0027\,MPa$ for the stand-off layer. For this reconstruction the recovered inclusion modulus value is 1.5461 ± 0.0959 to a background modulus value of 1.000 ± 0.0002. The average stand-off modulus value is 2.6169 ± 0.3353. For this reconstruction the inclusion volume was $0.1047cm^3$ compared to a reference volume of $0.0869cm^3$. The average strain in the inclusion and in the background was -0.0122 ± 0.0004 and -0.0177 ± 0.0012, respectively. Figures 6.16(a) and (b) show the 3D reconstructed modulus images in the x-y plane and the x-z plane sliced through the center of the inclusion. Figures 6.17(a) and (b) show the x-y slice of the reconstructed modulus image next to the
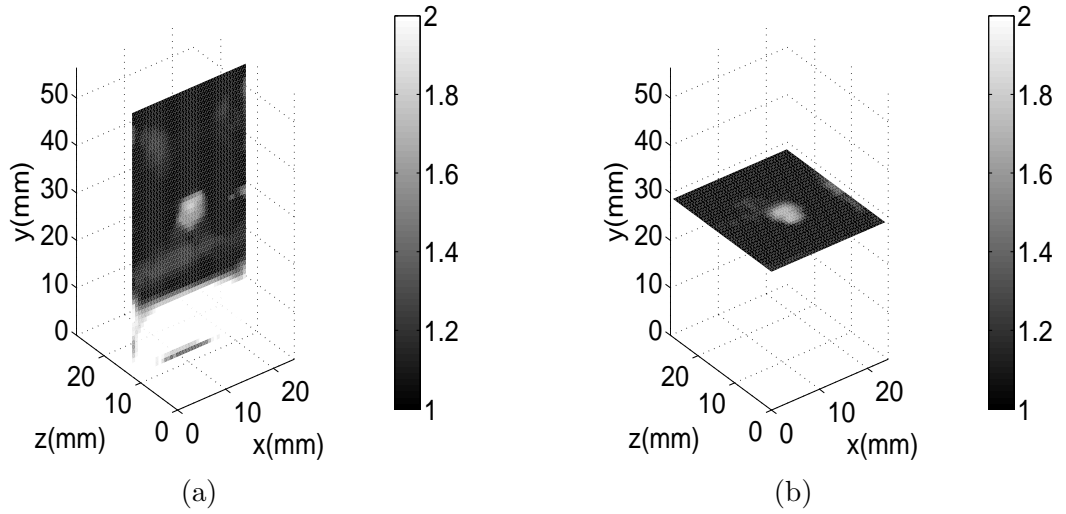
Figure 6.16: (a) x-y slice of 3D modulus reconstruction for a small inclusion with a 12% by mass gelatin concentration through the center of the inclusion. (b) x-z slice of 3D modulus reconstruction for this same inclusion through the center of the inclusion.

same slice of the axial strain image (ϵ_{yy}). Figure 6.18 shows an axial line of the modulus distribution through the center of the inclusion.

6.4.6   Inclusion Six

The sixth inclusion imaged was made such that the contrast with the background was even lower than that of the previous two phantoms. The inclusion size was made to be $7.94mm$ in diameter and $7.94mm$ in height. The background was made with an 8% by mass concentration of gelatin and the inclusion and stand-off layer were made with a 10% by mass concentration of gelatin. The stand-off in this phantom was positioned at the bottom of the phantom when imaged for this reconstruction. The independent mechanical test showed no significant difference in the measured Young's moduli between the inclusion and background. The values were $0.0184 \pm 0.00062\, MPa$ for the background and $0.0187 \pm 0.0041\, MPa$ for the inclusion and stand-off layer. For this reconstruction the recovered inclusion modulus value is 1.2771 ± 0.0557 to a background modulus value
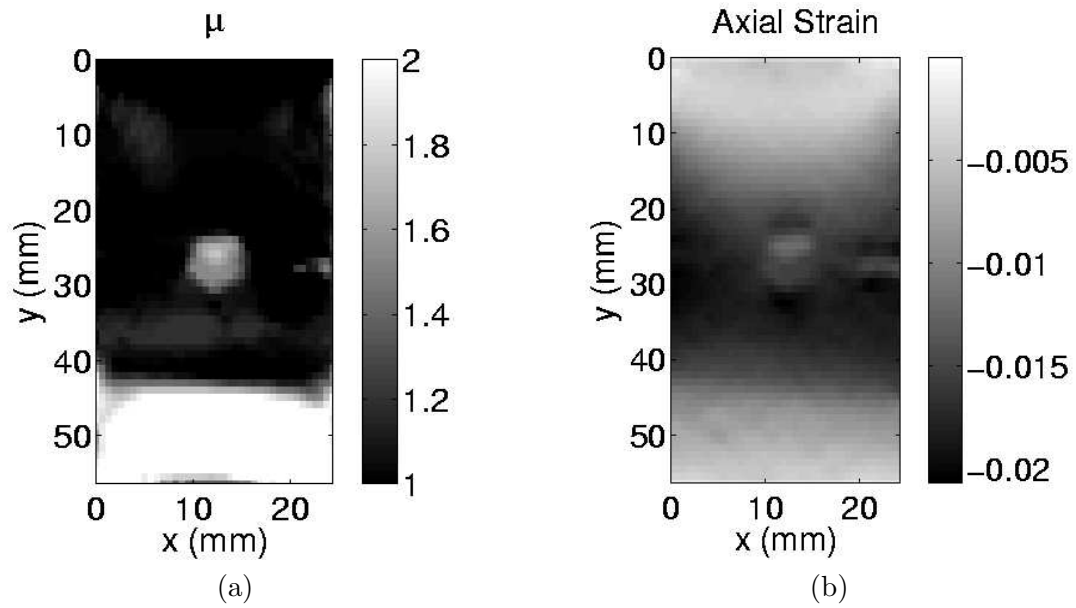
Figure 6.17: (a) x-y slice of modulus reconstruction for a small inclusion with a 12% by mass gelatin concentration. (b) x-y slice of the axial strain (ϵ_{yy}) for this same inclusion.
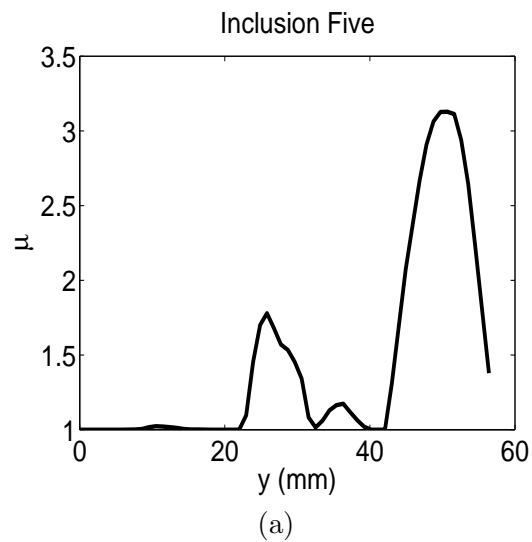

Figure 6.18: Axial line of the modulus distribution for a small inclusion with a 12% by mass gelatin concentration.
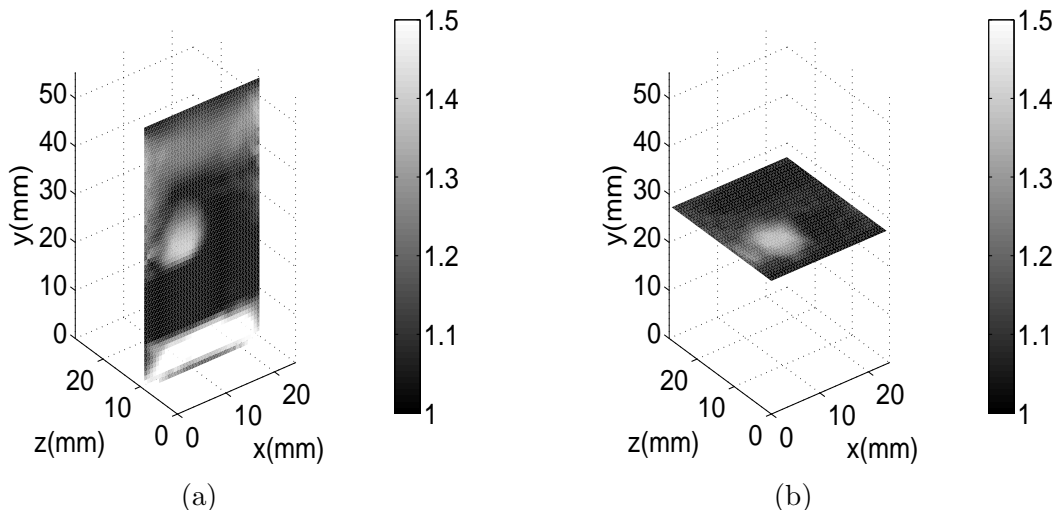
Figure 6.19: (a) x-y slice of 3D modulus reconstruction for a medium sized inclusion with a 10% by mass gelatin concentration through the center of the inclusion. (b) x-z slice of 3D modulus reconstruction for this same inclusion through the center of the inclusion.

of 1.0021 ± 0.0053. The average stand-off modulus value is 1.5695 ± 0.1049. For this reconstruction the inclusion volume was $0.3810 cm^3$ compared to a reference volume of $0.3931 cm^3$. The average strain in the inclusion and in the background was -0.0155 ± 0.0009 and -0.0184 ± 0.0015, respectively. Figures 6.19(a) and (b) show the 3D reconstructed modulus images in the x-y plane and the x-z plane sliced through the center of the inclusion. Figures 6.20(a) and (b) show the x-y slice of the reconstructed modulus image next to the same slice of the axial strain image (ϵ_{yy}). Figure 6.21 shows an axial line of the modulus distribution through the center of the inclusion.

6.4.7 Inclusion Seven

The seventh and last inclusion imaged was made such that the contrast with the background as low as the previous phantom but a smaller smaller size. The inclusion size was made to be $4.80 mm$ in diameter and $4.80 mm$ in height. The background was made with an 8% by mass concentration of gelatin and the inclusion and stand-off layer were made with
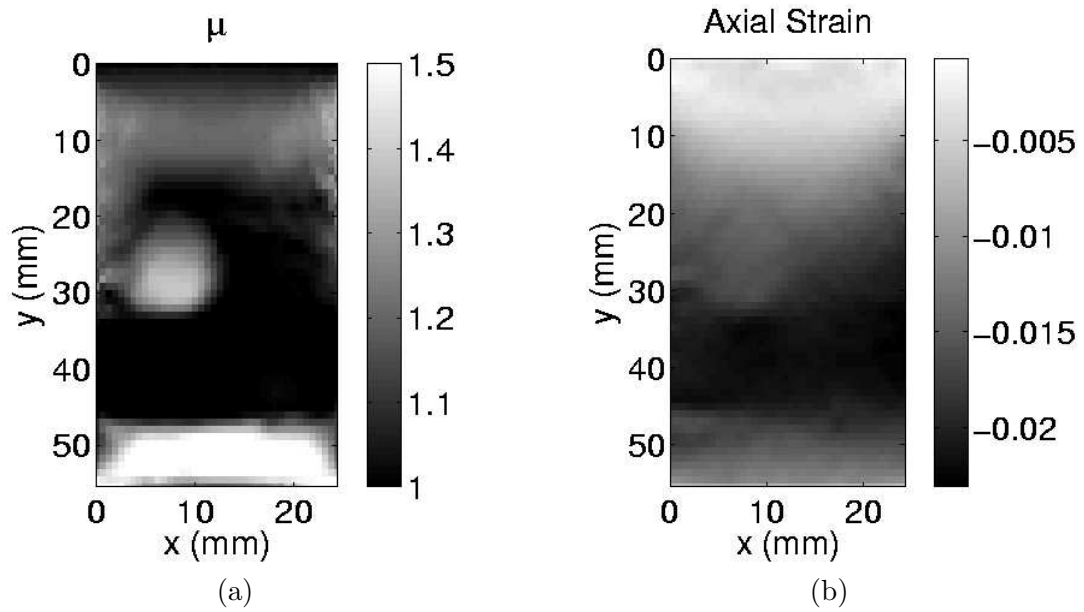
Figure 6.20: (a) x-y slice of modulus reconstruction for a medium sized inclusion with a 10% by mass gelatin concentration. (b) x-y slice of the axial strain (ϵ_{yy}) for this same inclusion.
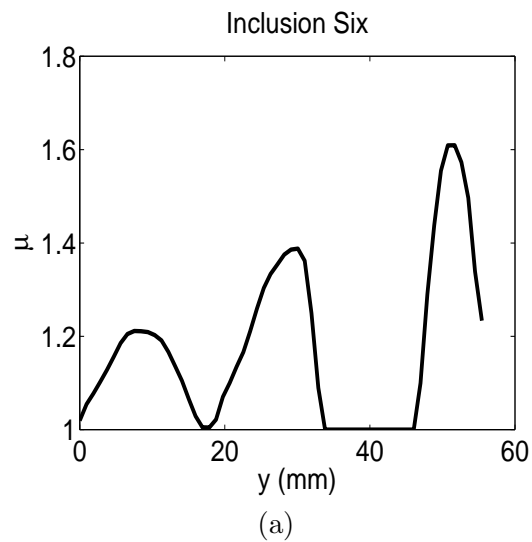

Figure 6.21: Axial line of the modulus distribution for a medium sized inclusion with a 10% by mass gelatin concentration.
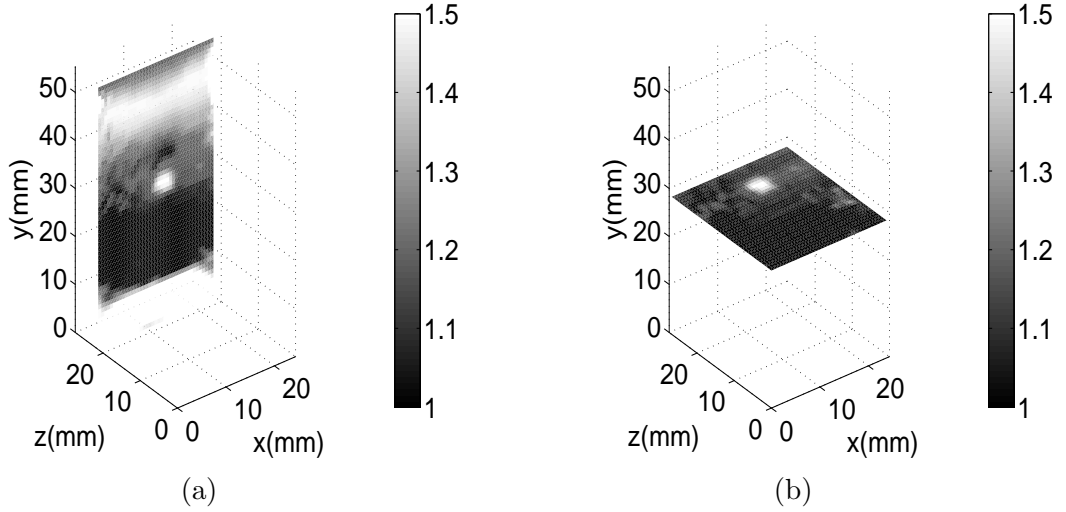
Figure 6.22: (a) x-y slice of 3D modulus reconstruction for a small inclusion with a 10% by mass gelatin concentration through the center of the inclusion. (b) x-z slice of 3D modulus reconstruction for this same inclusion through the center of the inclusion.

a 10% by mass concentration of gelatin. The stand-off in this phantom was positioned at the bottom of the phantom when imaged for this reconstruction. Again, the independent mechanical test showed no significant difference in the measured Young's moduli. The values were $0.0184 \pm 0.00062\,MPa$ for the background and $0.0187 \pm 0.0041\,MPa$ for the inclusion and stand-off layer. For this reconstruction the recovered inclusion modulus value is 1.3624 ± 0.0714 to a background modulus value of 1.0010 ± 0.0047. The average stand-off modulus value is 2.0528 ± 0.2291. For this reconstruction the inclusion volume was $0.0499cm^3$ compared to a reference volume of $0.0869cm^3$. The average strain in the inclusion and in the background was -0.0145 ± 0.0002 and -0.0186 ± 0.0019, respectively. Figures 6.22(a) and (b) show the 3D reconstructed modulus images in the x-y plane and the x-z plane sliced through the center of the inclusion. Figures 6.23(a) and (b) show the x-y slice of the reconstructed modulus image next to the same slice of the axial strain image (ϵ_{yy}). Figure 6.24 shows an axial line of the modulus distribution through the center of the inclusion.
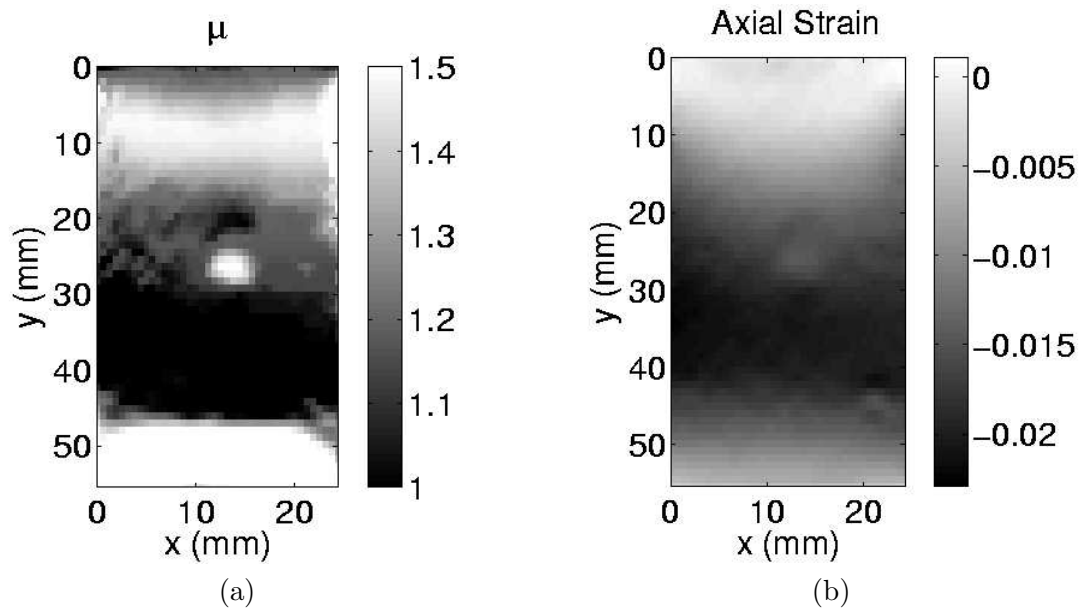
Figure 6.23: (a) x-y slice of modulus reconstruction for a small inclusion with a 10% by mass gelatin concentration. (b) x-y slice of the axial strain (ϵ_{yy}) for this same inclusion.
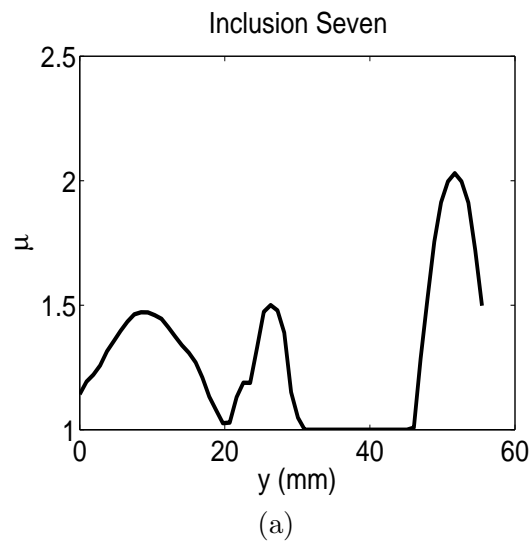

Figure 6.24: Axial line of the modulus distribution for a small inclusion with a 10% by mass gelatin concentration.

	Inclusion Size		
Inclusion Gel Concentration	Large ($1.28cm^3$)	Medium ($0.393cm^3$)	Small ($0.0869cm^3$)
16% by mass	$C_{ref} = 3.241 \pm 0.280$ $C_{rec} = 2.234 \pm 0.228$ $C_{str} = 1.566 \pm 0.124$ $\gamma_{sz} = 1.18$	$C_{ref} = 3.241 \pm 0.280$ $C_{rec} = 2.087 \pm 0.203$ $C_{str} = 1.284 \pm 0.138$ $\gamma_{sz} = 1.163$	$C_{ref} = 2.561 \pm 0.171$ $C_{rec} = 2.041 \pm 0.211$ $C_{str} = 1.261 \pm 0.192$ $\gamma_{sz} = 1.10$
12% by mass	NA	$C_{ref} = 2.005 \pm 0.215$ $C_{rec} = 1.611 \pm 0.122$ $C_{str} = 1.308 \pm 0.176$ $\gamma_{sz} = 0.832$	$C_{ref} = 1.890 \pm 0.105$ $C_{rec} = 1.546 \pm 0.096$ $C_{str} = 1.451 \pm 0.109$ $\gamma_{sz} = 1.205$
10% by mass	NA	$C_{ref} = 1.016 \pm 0.225$ $C_{rec} = 1.251 \pm 0.055$ $C_{str} = 1.187 \pm 0.119$ $\gamma_{sz} = 0.969$	$C_{ref} = 1.016 \pm 0.225$ $C_{rec} = 1.361 \pm 0.072$ $C_{str} = 1.283 \pm 0.132$ $\gamma_{sz} = 0.574$

Table 6.1: Reconstructed modulus contrast accuracy reported for the inclusion sizes and gelatin concentrations.

6.5 Discussion

In this study, three different inclusion sizes and modulus contrasts were investigated and reconstructed. They were selected to identify the spacial and contrast resolution of these techniques. The modulus contrasts used lie at the low extreme of clinical interest. The smallest inclusion used is at the limit of the manufacturing capabilities and at the lower limit of current clinical interest. The values of the recovered contrasts in the inclusion and the expected values for each inclusion type are shown in Table 6.1. Also shown is the ratio of the reconstructed inclusion volume to the actual inclusion volume. In Table 6.1, C_{ref} is the reference modulus contrast of the independently measured gelatin samples for the inclusion relative to the background, C_{rec} is the recovered or reconstructed contrast reported for the inclusion relative to the background, C_{str} is the strain contrast measured in the background relative to the inclusion and γ_{sz} is the ratio of the reconstructed inclusion volume relative to the reference volume of the inclusion when it was made.

The reconstructed inclusion contrasts tend to be lower than the contrasts reported

by independent mechanical testing, except for those at the lowest contrast. The apparent systematic contrast reduction is due, at least in part, to the averaging of the modulus value in the volume calculated from the half maximum. Furthermore, the role of the regularization in the displacement estimation and the inversion would cause the reconstructions to under-predict the actual modulus value of the underlying material. For the lowest contrast inclusions the discrepancy between the reference contrast and the reconstructed contrast is likely due to error in the reference contrast. The independent mechanical tests suggest that no contrast should be seen in these inclusions. This is counter to the design of the experiment, in which the concentrations are approximately 8% and 10%. Gelatin stiffness is known to have a high variabililty depending on the length of time between setting and testing as well as the temperature at which it was tested (Hall et al., 1996). This fact, in conjunction with the variability in the mechanical testing itself, is likely to have caused the lack of measurable contrast in the independent tests. The fact that the inclusions were resolved in the reconstructed modulus images is highly suggestive that some contrast does exist between these gelatin concentrations.

The volume of the reconstructed inclusion relative to its actual volume seems to vary unpredictably, but in nearly all cases is within $\pm\frac{1}{2}$voxel size in the linear dimensions of the sample. It seems to be most accurate for the medium sized inclusions and highest contrast. Certainly the volume of the reconstructed inclusion will depend on the somewhat arbitrary selection of the inclusion boundary. Here the inclusion perimeter was chosen at the half maximum of the inclusion modulus value. Additionally, regularization plays a role in both the resolved contrast of an inclusion and the shape of the boundaries of the inclusion. The "strength" of the regularization term in the functional is determined not only by the magnitude of the α parameter but also the size and contrast of the underlying modulus distribution. Thus, regularization will tend to play a larger role in modulus distributions with higher contrasts and larger sizes. Since the underlying modulus distribution is unknown in practice, this remains a challenge for this type of reconstruction. It should also be noted that the presence of the surrounding artifacts is more obvious for smaller inclusion

	Inclusion Size		
Inclusion Gel Concentration	Large ($1.28cm^3$)	Medium ($0.393cm^3$)	Small ($0.0869cm^3$)
16% by mass	$C_{ref} = 3.241 \pm 0.280$ $C_{rec} = 2.087 \pm 0.156$	$C_{ref} = 3.241 \pm 0.280$ $C_{rec} = 1.825 \pm 0.055$	$C_{ref} = 2.412 \pm 0.237$ $C_{rec} = 2.852 \pm 0.349$
12% by mass	NA	$C_{ref} = 2.005 \pm 0.215$ $C_{rec} = 2.484 \pm 0.224$	$C_{ref} = 2.412 \pm 0.237$ $C_{rec} = 2.950 \pm 0.186$
10% by mass	NA	$C_{ref} = 1.016 \pm 0.225$ $C_{rec} = 1.626 \pm 0.076$	$C_{ref} = 1.016 \pm 0.225$ $C_{rec} = 1.282 \pm 0.088$

Table 6.2: Reconstructed modulus contrast accuracy, using mixed boundary conditions, and reference contrast for the stand-off layer reported for the inclusion sizes and gelatin concentrations.

contrasts. It is possible that increasing the regularization in these cases, to try and further minimize the artifacts, may cause the low contrast inclusion to be lost.

Table 6.2 shows the reference contrast values C_{ref} and recovered modulus contrast C_{rec} in the stand-off defined by those values above its half maximum. The accuracy of the stand-off layer seems to depend on the location when imaged (most likely a consequence of the acoustic window) as well as the size and contrast of the modulus distribution as a whole. The assumed zero normal traction boundary conditions are more accurate near the bottom of the phantom then near the top. Thus when the stand-off layer is on the bottom, its contrast is systematically increased.

From a purely imaging standpoint, it is promising that each reconstruction clearly resolves the inclusion. In each case, the location and size of the inclusion are clear. It should be noted that the contrasts and sizes of the inclusions created in this study are in the lower limit of what can be expected in a clinical setting. In comparison to strain images shown, which are the images typically used in common elastography practice, the modulus images show a much clearer boundary and contrast of the inclusion and have a much lower presence of artifacts in the images.

Chapter 7

Tomosynthesis Elasticity Imaging

7.1 Introduction

Although the elasticity imaging methodology is well suited for use in conjunction with US image, it is not limited to US systems. The ultrasound imaging protocol proposed in this thesis provides a method of obtaining elasticity images, using an ultrasound scanner, within the confinement setup of a tomosynthesis, x-ray mammography system. In this way one is able to create ultrasound images, elasticity images and tomosynthesis which are aligned and coregistered. It may also be possible, however, to create elasticity images directly from sets of the three dimensional tomosynthesis images. In the following section, the feasibility of such a technique is discussed as well as the advantages and disadvantages of using the tomosynthesis images for elastic inversions over the ultrasound system.

7.1.1 Tomosynthesis Imaging: Background

Conventional x-ray mammography techniques involve passing x-ray beams through breast tissue and detecting the intensity of the beams exiting the tissue with either screen-film detectors or digital detectors (See Figures 1.1 and 7.1). Mathematically, the resulting transmission intensity of the image is known to be a fraction of the initial x-ray intensity which is related to the integral of the attenuation of the material through which the x-ray beam passed. For a given pixel, the governing equation for the image intensity is:

$$I(x,y) = I_0 \, \exp \int_{Source}^{Receiver} -\mu(x,y,z) \, ds, \qquad (7.1)$$

where I_0 is the initial beam intensity, $\mu(x, y, z)$ is the three dimensional function of x-ray attenuation and s is the propagation distance of the x-ray beam through the attenuating material and normal to the imaging detector (Chen and Ning, 2003). The attenuation of the tissue is a quantity describing its intrinsic ability to scatter and absorb x-rays as they pass through it. It is highly dependent on its molecular composition and density (Macowski, 1983). The breast is typically compressed to reduce the x-ray exposure level necessary to obtain detectable intensities and to limit the variability of materials in a given beam path length. The resulting image created by the detector is a two dimensional projection of a three dimensional breast. This can lead to feature overlap and areas of blurred resolution.

Tomographic techniques result in a three dimensional image of x-ray attenuation and partially alleviate feature overlap problems. They also add the distinct advantage of depth localization and single slice evaluation (Dobbins and Godfrey, 2003). The idea of tomography is to take several low dose projection images of the subject, each at a different angle and orientation relative to the subject. The images are acquired using a digital detector and a computer algorithm reconstructs a three-dimensional image based on the projections. Computerized tomography (CT) is a popular example of this technology. CT images are constructed from sequential projections of a beam through a subject that is rotated or scanned over a plane of interest. The resulting projection intensities are inverted to create an image slice of the x-ray attenuation.

Tomosynthesis imaging is a similar technique, which acquires a limited number of two-dimensional projections taken at orientations confined in proximity. As a result, the reconstructed images have a lower spatial resolution in the average direction of the x-ray beam but are still able to eliminate overlap and blurred structure. A graphical representation of conventional mammography and tomosynthesis can be found in Figures 1.1 and 7.1(b). The collaborators of this work at Massachusetts General Hospital (MGH) use a tomosynthesis mammography system and investigate its potential for incorporating it into standard mammography protocols. Although many different computer algorithms exist for
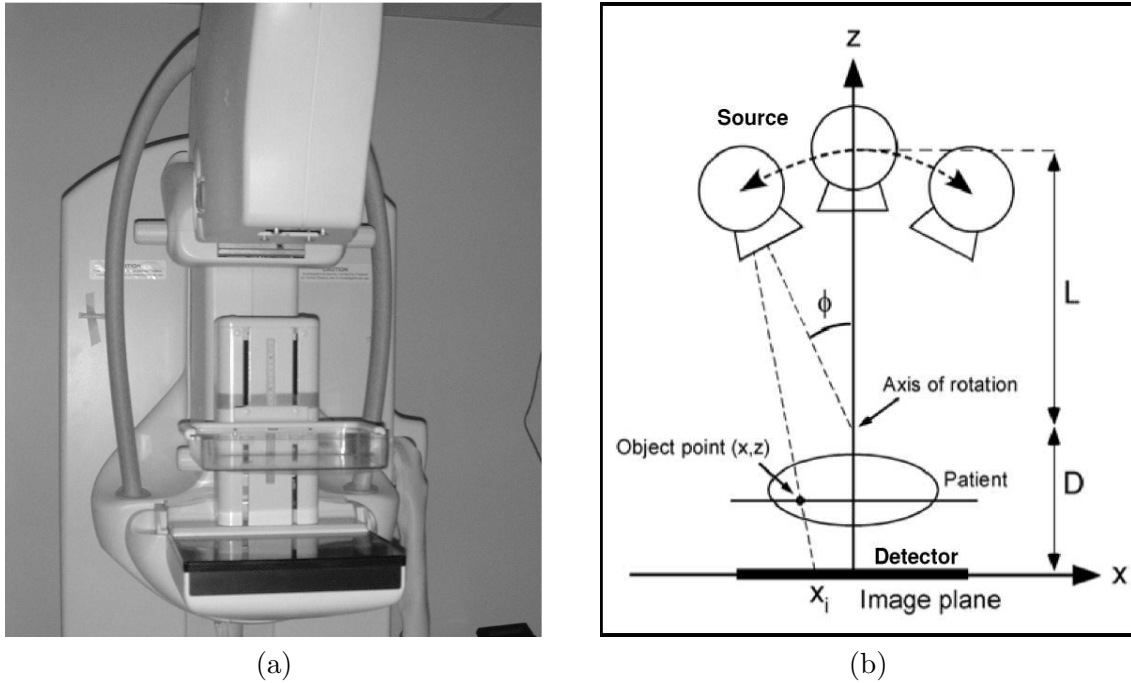
Figure 7.1: (a) Tomosynthesis imaging system. (b) Tomosynthesis schematic (Adapted from Dobbins and Godfrey, 2003).

reconstructing three dimensional image volumes from projections, the group at MGH has developed a maximum likelihood expectation maximum algorithm for their reconstructions (Wu et al., 2003). This is an iterative algorithm based on the probability of producing the acquired projections from a particular image volume. There are 15 distinct projections taken over a 50° range relative to the subject and detector. The center of the image angles is exactly perpendicular to the plane of the detector as shown in Figure 7.1(b).

The reconstructed image resolution will depend not only on the detector resolution but will be limited by the 15 images and the 50° angle span. The direction perpendicular to the detector (z) will have the lowest resolution of the three dimensional reconstruction. The resolution of the other directions (x and y) is dependent mainly on the detector resolution.

For tomosynthesis imaging, the breast is still held in compression. This not only reduces the beam path length but also acts to stabilize the patient, minimizing movement during
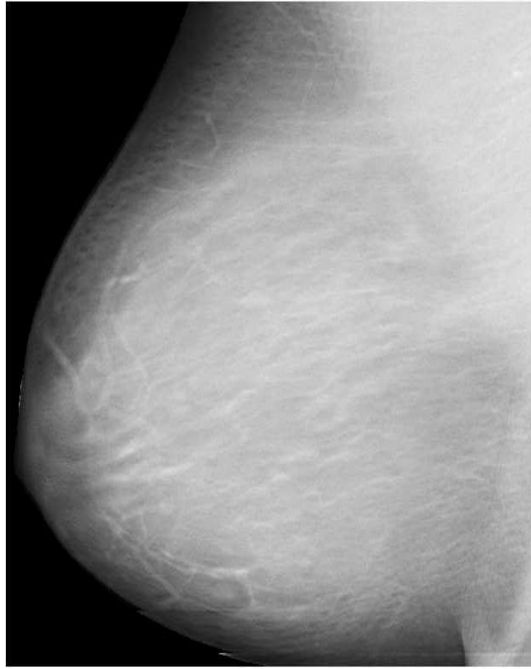
Figure 7.2: Typical tomosynthesis image slice.

image acquisition. The dose of each of the 15 projections is lowered such that the total x-ray dose is equivalent to that of two typical mammography images, which is the current minimum number of images taken for clinical breast screening examinations (Wu et al., 2003). Figure 7.2 shows a typical image slice taken from a reconstruction produced by the group at MGH. The density of glands, blood vessels and small scale tissue structure which make up the features of the image will determine the ability to measure the displacements from these reconstructions.

7.2 Phantom Construction

As in ultrasound imaging, it is important to develop x-ray phantoms which can be used to test the techniques used for elasticity imaging. For these tomosynthesis phantoms, x-ray absorption is spatially modulated by adding chalk particles. Chalk ($CaCO_3$) was

chosen because it is a strong absorber of x-rays, due to calcium's high molecular weight. The particles are suspended in the gelatin to introduce features to the phantom, mimicking attenuation differences found between blood vessels, glandular tissue, calcium deposits and the background tissues of the breast. The size and density of the chalk particles were made to qualitatively mimic feature size and density found in typical breast images. Chalk concentration was adjusted to approximate overall x-ray attenuation in breast tissue, 2% by mass (Homolka et al., 2002; Polletti et al., 2002). These phantoms were cuboid or brick shaped, but larger than the ultrasound phantom, typically 6-12cm in length to 8cm in height. Inclusions were also added to these phantoms by altering gelatin concentration in discrete areas of the phantom. The inclusions were typically cylindrical. Figure 7.3 shows the top view of a sliced tomosynthesis phantom with an inclusion. A step by step protocol for making elastic tomosynthesis phantoms can be found in Appendix A.
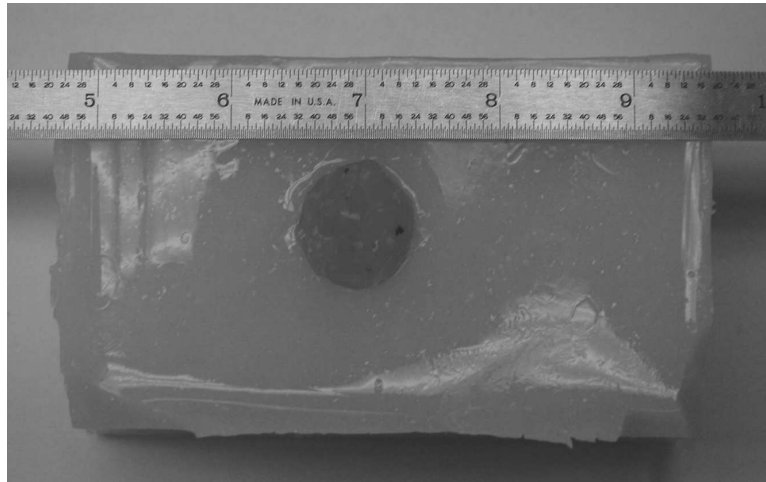

Figure 7.3: Tomosynthesis phantom sliced through the cylindrical inclusion.
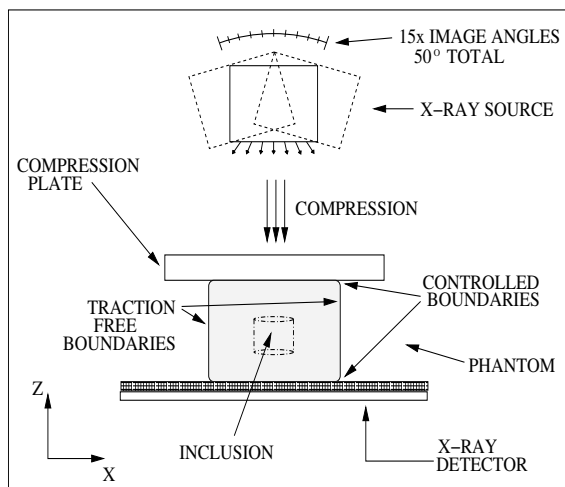
Figure 7.4: Tomosynthesis imaging setup.

7.3   Imaging Protocol

The phantom used in the tomosynthesis experiments is held at the top by a compression plate, which is transparent to x-rays, and at the bottom by the x-ray detector. A schematic of the experimental setup is shown in Figure 7.4. The phantom is held in compression while the first set of 15 images is acquired. Then a compressive strain is applied by the top plate ($\sim$ 10-15%) and a second set of images is acquired. A larger strain is required for the tomosynthesis imaging, compared with the ultrasound, due to characteristics of the tomosynthesis images (see Section 3.2). The reconstructed images have a voxel size of $1000\mu m \times 100\mu m \times 100\mu m$. The high resolution directions are in the plane of the detector (x and y). The resulting image dimensions are about $40 \times 1000 \times 1000$ pixels in the z, x and y directions, respectively. In some experiments the top or bottom of the phantom was lubricated with a water based gel (e.g. ultrasound coupling gel) to facilitate slipping at the boundaries. Figure 7.5 shows a slice of a reconstructed x-ray image through the middle of the phantom and parallel to the detector plate.
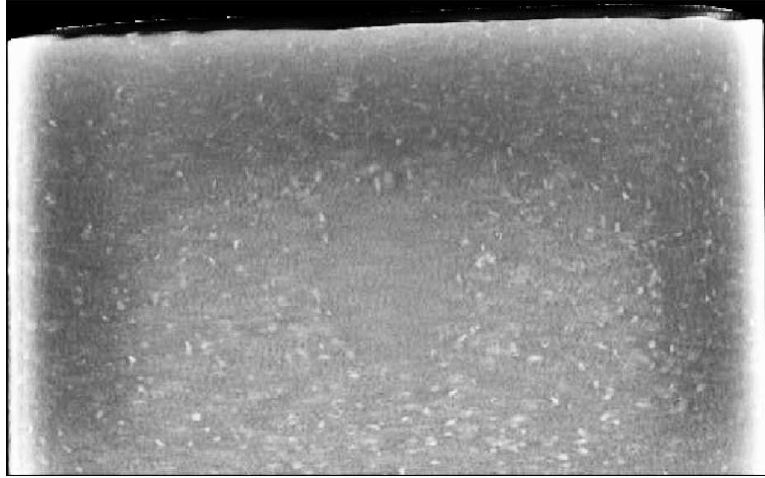
Figure 7.5: Tomosynthesis phantom image slice through the cylindrical inclusion.

7.4 Simultaneous Registration And Reconstruction

As one would expect, the characteristics of the tomosynthesis images are very different from those of the ultrasound images. It is clear from Figure 3.2 that the frequency distribution of signal in the reconstructed tomosynthesis images is much lower than that of ultrasound images. The signal to noise ratio of these images is much lower as well. Additionally, the tomosynthesis images tend to have artifacts in them which are characteristic of the imaging system itself and relatively independent of the tissue being imaged. However, the tomosynthesis system can image tissue, or phantoms, all the way to the tissue's boundaries. In the case of the cuboidal phantoms, the tomosynthesis system images all six borders of the phantom, including the four sides which are known to be traction free. In actual breast tissue, the images capture the breast surfaces adjacent to the compression plate and detector, the traction free borders on the exterior of the breast, and interior breast at the chest wall.

Due to the high noise considerations of processing the tomosynthesis data, a third algorithm was developed. This algorithm is called simultaneous image registration and elastic

modulus reconstruction (SRR). It is an image registration code which constrains the set of possible displacements by the equations of linear, incompressible elasticity with an unknown shear modulus distribution. The optimization seeks a shear modulus distribution for the underlying tissue. This algorithm is closely related to the two algorithms used for the ultrasound image reconstructions except the step of measuring a displacement field becomes implicit to the code. The three dimensional version of this algorithm written for this work is based on a two dimensional algorithm developed by Gokhale et al., 2004.

The optimization functional is of the following form:

$$\pi(\mu) = \frac{1}{2} \int_\Omega (I_1 - I_2(\mathbf{u})))^2 \, d\Omega + A(\mathbf{w}, \mathbf{u} \, ; \mu) - (\mathbf{w}, \mathbf{h})_{\Gamma_h} + R[\mu]. \tag{7.2}$$

Here, $R[\mu]$ denotes a regularization term, which can be either the L^2 norm or the TVD norm described in Section 4.2.3. $A(\cdot, \cdot ; \cdot)$ denotes the bilinear form of the linear, incompressible elasticity equations defined in equations (4.8) and (4.9). This functional is minimized using the same quasi-Newton algorithm described in Section 4.2. To calculate the gradient, the functions of $\mathbf{u}$, μ and their variants are discretized with the finite element interpolation functions defined in equations (4.12)-(4.14). The adjoint method is again utilized to efficiently calculate the gradient. In this formulation the discretized gradient vector is still equivalent to equation (4.24)(prior to the addition of the regularization), however, the $\mathbf{w}^h$ is now found by solving the following equation:

$$A(\delta\mathbf{u}^h, \mathbf{w}^h \, ; \mu^h) = \int_\Omega (I_1 - I_2(\mathbf{u}^h))\nabla I_2(\mathbf{u}^h) \cdot \delta\mathbf{u}^h \, d\Omega \qquad \forall \delta\mathbf{u} \in \mathcal{V}. \tag{7.3}$$

All other relevant computational methods (e.g. image interpolation, pressure integration, parallelization, solver, etc.) are equivalent to those methods outlined in Chapters 3 and 4.

Given the choice of model and reconstruction parameters, the only other information needed prior to running this algorithm is the knowledge of the boundary conditions. In the case of the tomosynthesis system, it is fortuitous that much of the image boundary conditions are traction free because traction free boundaries require no prior measurement.

Additionally, the boundary conditions of those surfaces parallel to the detector plate and the compression plate may be known, without image measurement, in certain instances. For example, if those surfaces were designed to be non slip, the displacement at the compression plate surface would be zero in the shear directions and a constant number equal to the applied compressive displacement. The displacement at the detector plate surface would be zero everywhere. Otherwise, if the tissue or phantom displaces at the boundaries and it cannot be assumed traction free, the displacements must be measured via some other image registration method, prior to running this algorithm.

7.5   Initial Results

To determine whether reconstructed shear modulus reconstructions were feasible using the tomosynthesis images, a phantom was constructed (see Section 7.2). This phantom was approximately $12cm$ in length (y), $6cm$ in depth (x) and $8cm$ in height (z). The phantom was created with an inclusion, in the center of this phantom, which was $1.9cm$ in diameter and $1.9cm$ height with a gelatin concentration such that the contrast to the background was approximately equal to 3.5

The boundary conditions on the phantom surfaces parallel to the detector and the compression plate were not fixed. The in-plane displacements on these boundaries were measured using the image registration algorithm discussed in Section 3.4. The parameters used for the registration were chosen as those which resulted in a, qualitatively perceived, smooth result. The choice of α_2 for this measurement was zero. The remaining boundaries were prescribed Neumann conditions with $\mathbf{h} = \mathbf{0}$.

These boundary conditions were then used as input to the SRR algorithm to reconstruct the elastic modulus. It should be noted that the images themselves were high pass filtered prior to being registered to eliminate some of the image artifacts inherent in the tomosynthesis images. The images were then squared to amplify the magnitude of the chalk induced features. The resolution of the resulting reconstruction was chosen to be

approximately $1.7mm \times 3mm \times 8mm$ in the y, x and z directions, respectively. The regularization of μ was chosen to be the L^2 norm and the magnitude of α_a was chosen as the value which resulted in a, qualitatively perceived, smooth reconstruction. Figure 7.6 shows the reconstructed modulus distribution sliced through the inclusion in the x-y and z-y planes (the reconstructions were up sampled for presentation).
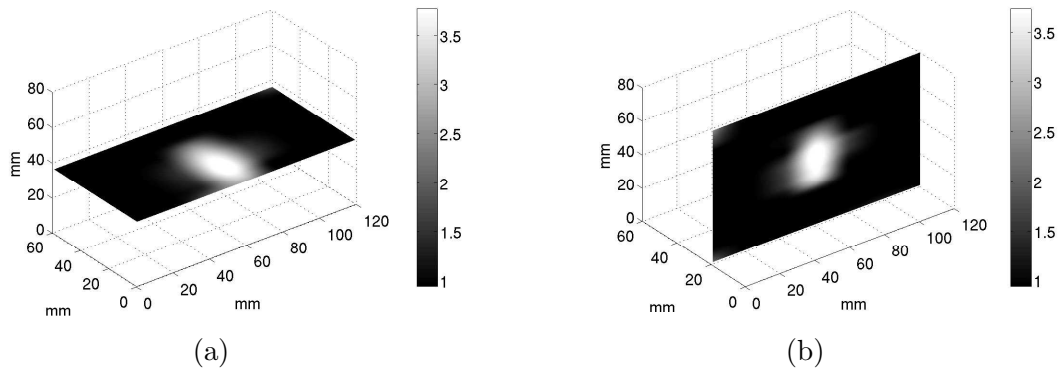

(a)   (b)

Figure 7.6: (a) Tomosynthesis modulus reconstruction sliced through the inclusion in the x-y plane. (b) Reconstruction sliced through the inclusion in the z-y plane.

7.6   Discussion

The results presented in Figure 7.6 represent the only reasonable reconstruction resulting from several tomosynthesis phantoms. While investigating the feasibility of this technique, it was found that creating phantoms which resulted in a homogeneous and high "enough" feature density proved extremely difficult. Therefore, only a limited number of phantoms created resulted in reasonable tomosynthesis images. Additionally, the variability in the tomosynthesis images for a given phantom under varying compression levels combined with the limited knowledge of the noise contributions to the tomosynthesis images in general led to the poor success rate in these reconstructions. However, prior to investigating reconstructions, it was found that the tomosynthesis images do have a high enough signal to noise ratio to expect reasonable displacement measurements for the phan-

tom as a whole, at least for a relative large resolution and applied strain level (see Section 3.2). This evidence, combined with the initial result shown here, suggests that further investigation into the noise sources in the tomosynthesis images and an improved phantom making protocol could result in consistent tomosynthesis elastic modulus images.

Chapter 8

Discussions

8.1 Summary

This thesis has motivated the use of three dimensional elasticity imaging as a possible method to improve the current practices in breast cancer management. Elasticity imaging is a novel technique which takes advantage of a tissue's altered mechanical properties, indicative of certain pathologies, as a method to identify and diagnose breast tumors. The elastic imaging methodology proposed in this work is an inexpensive adjunct to imaging technologies already commonly used in mammography. In particular, elasticity imaging can be added as an adjunct to ultrasound imaging to produce images of a tissue's mechanical properties. The images created with this technique can reveal information about the underlying tissue which is distinct from the information extracted from ultrasound alone.

In order to infer or quantify a tissue's mechanical properties, an appropriate mathematical model must be chosen. In this work, a three dimensional, single phase, linear elastic, incompressible model was proposed to quantify the shear elastic modulus of breast tissue. The assumptions of this model were presented and justified in Chapter 2. Once an appropriate model is chosen, there are two necessary components to the process of elasticity imaging. The first is a method to measure tissue deformation from a set of images. The second is a method to use the measured displacement and the mathematical model to infer the relevant mechanical properties of the underlying tissue.

Chapter 3 presents and validates a novel method to measure the displacement from sets of ultrasound images of breast tissue or breast tissue mimicking materials at two different deformation states. The novel features of this method include the use of finite element

interpolation, the use of global information for each nodal estimation and the systematic incorporation of prior knowledge to stabilize the estimated displacements.

Chapter 4 presents a method to measure the underlying shear modulus of that tissue from the measured displacements up to a multiplicative constant. The novel features of this method include the use of an iterative quasi-Newton method to quantify mechanical properties from a measured displacement field, the use of the adjoint method to efficiently calculate the gradient, and the use of a stand-off layer for calibration purposes.

Chapter 5 discusses issues concerning the uniqueness of the measured tissue properties, and the sensitivity/insensitivity of the displacements to the modulus distribution.

The algorithms and methodologies presented here were then evaluated in a study to create shear modulus images from tissue mimicking phantoms created to specifically mimic acoustic and mechanical behavior of tissue. The phantom properties were calibrated by independent mechanical tests. Inclusions mimicking breast tumors from $4mm$-$12mm$ in size were evaluated. These had stiffness contrasts close to one to about three. The resulting modulus images of these phantoms were presented alongside strain images for comparison of the current techniques used in elastography.

Finally, in Chapter 7, a proposed methodology is presented, utilizing the same model and similar techniques, to quantify mechanical properties for tissue imaged with x-ray tomosynthesis. The advantages and disadvantages of this technique compared to the use of ultrasound images are discussed.

8.2 Discussion

The displacement estimation technique presented here is a three dimensional, iterative Gauss-Newton intensity matching algorithm which tracks feature motion between image pairs. The method uses a finite element interpolation, which allows for distorted elements and nonuniform meshes. This is in contrast to typical feature tracking algorithms common in elastography, utilizing rigid block matching methods which tend to result in noisy dis-

placement measurements. The finite element interpolation allows for the implementation of regularization, to minimize noise in the measurements, as well as an incompressibility constraint to penalize non-volume conserving deformations. The results of Chapter 3 indicate that incompressibility constraint helps to decrease the noise in the solution in all directions. As the incompressibility parameter is increased, the noise decreases up to a point, after which there appears to be no benefit from further increasing the α_2 value. Increasing the regularization parameter (α_1), on the other hand, improves the displacement estimates to a point after which the accuracy of the estimate begins to decline.

One complication arising from regularization is the introduction of systematic artifacts in the displacements, which become increasingly prevalent with increasing α_1. These artifacts are restricted to boundaries, however, and the interior of the measurement domain remains relatively accurate. Suggested future improvements to this algorithm are a regularization scheme which will minimize or eliminate the presence of these artifacts. Some possible directions, in that vain, are to allow the regularization parameter α to vary spatially. Alternatively one could determine an alternate norm to use for the regularization, however, this may necessitate higher order interpolation functions for the displacement estimates.

Chapter 3 also shows that image interpolation accuracy is the primary limitation of the displacement accuracy. As technological progress diminishes concerns of computational cost, however, the displacement estimation can improve with higher order interpolation schemes and more finely sampled images. The image integration is the limiting factor in terms of computational speed of this algorithm.

The shear modulus inversion algorithm, presented in Chapter 4, is a three dimensional quasi-Newton algorithm which minimizes the difference between a measured displacement field and a displacement field predicted by a linear elastic, incompressible solid model. The algorithm seeks to find the shear modulus distribution which minimizes this difference. The choice of Poisson's ratio used in this model was found to have little effect on the resulting modulus reconstruction, for materials with bulk and shear moduli in the range of

soft tissue.

Chapters 4 and 5 also discuss the complications which arise from the choice of boundary conditions in the optimization problem. For now, this remains as one of the most important issues affecting the accuracy of the result. Imposing all displacement boundary conditions leads to insensitivity at the boundaries, and an inability to resolve particular modulus distributions like the stand-off layer. The mixed boundary conditions, in which the normal tractions on the vertical surfaces of the phantom are assumed to be zero, can resolve the modulus geometries such as a stand-off. Any inaccuracy in the assumed mixed boundary conditions, however, introduces modulus artifacts into the resulting images. These artifacts can be controlled by regularization, to a certain extent, but clearly this solution is unsatisfactory.

The idea of using a stand-off layer for calibration purposes is untenable at this stage until the issue of the boundary conditions is resolved. Future directions for this algorithm will be to further understand the relationship between the boundary conditions and the accuracy of the reconstruction. In particular, the use of traction boundary conditions shows promise, but as yet there exists no method to measure the tractions on the boundaries. The addition of a second measured displacement field should be considered.

The US phantom study shows the ability of these algorithms to recover modulus images, using the ultrasound images and experimental protocol outlined in Chapter 6. The accuracy of the size and contrast of the reconstructed inclusion seems to vary depending on the size and contrast of the actual inclusion. The reconstructed modulus value tends to underestimate the reference. The types of artifacts seen in the reconstructed modulus images closely resemble those seen in the simulated perfect data from Chapter 4. These include an artificial stiffening at the top or bottom of the reconstruction opposite the stand-off layer, and a drop in the expected modulus value between the stand-off and the boundaries surrounding it. These artifacts are due to the zero normal traction assumption, and the drop in the modulus value is expected to be caused by insensitivity near those surfaces. These observations again point to the critical role of the assumed boundary conditions in

the reconstruction.

The choice of regularization used in the phantom study was lower than the optimal value found in the artificial study. The reason for this was that the magnitude of noise in the simulated study was chosen according to the noise estimations made in Chapter 3. A large portion of the error in the measurements of Chapter 3 are due to the boundary artifacts, which only effect the periphery of domain. Therefore interior noise in the simulated data is expected to be significantly larger than in the real data. Additionally, the strength of the reconstruction is affected by the size and contrast of the actual modulus distribution. For the phantom experiments, the actual modulus distributions had large variations in size and shape relative to each other. As is clear in Figure 4.7, the decay in modulus accuracy is less for a lower choice of α. Thus a lower α was chosen at 1×10^{-4} in an effort to accurately reconstruct all phantom inclusions.

The modulus images of Chapter 6 show a clear advantage over strain images in the ability to recover the inclusion contrast and size. In addition, the modulus images do not suffer from the strain artifacts seen in these experiments. Of course, there are modulus artifacts present in the reconstructions, however their magnitude and size do not occlude the inclusion in any reconstruction.

The ability of this technique to resolve inclusions in these phantom studies is strong evidence supporting the continued evaluation of the use of shear modulus images in a clinical setting. To that end, a future direction of this project will be the implementation of three dimensional ultrasound elasticity imaging in the context of an x-ray tomosynthesis mammography regime. Figure 8.1 suggests a possible clinical setup which can facilitate this study. Here the ultrasound is scanned through the paddle used to compress the breast during a clinical x-ray exam. This paddle provides a method to apply a deformation to the tissue. The resulting ultrasound and hence elasticity images could be easily registered with the x-ray images if the position of the ultrasound transducer is known relative to the x-ray detector (i.e. scanned from a fixed position on the imaging system).

The feasibility of using x-ray tomosynthesis images to measure mechanical proper-
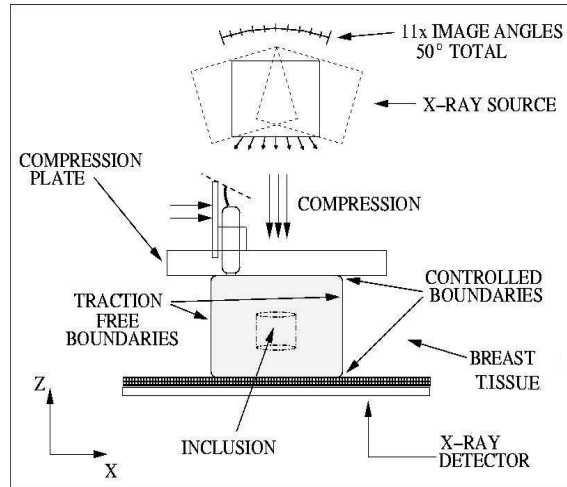
Figure 8.1: Three dimensional ultrasound imaging setup for clinical elasticity imaging.

ties of breast tissue has also been presented. Using tomosynthesis has the advantages of imaging the entire breast, including the boundaries which are known to be traction free. Additionally, using elasticity imaging as an adjunct to tomosynthesis would result in modulus images which are inherently registered with the tomosynthesis images themselves. While the result presented in Chapter 7 appears promising, further understanding of the noise and image artifacts of the tomosynthesis system is recommended before proceeding with a clinical investigation. Finally, processing tomosynthesis images of a breast would likely benefit from an irregular finite element mesh, with element sizes that vary with local image feature density. The finite element based algorithms developed here can, by design, accommodate such meshes.

8.3 Conclusions

The elasticity imaging methodology proposed in this thesis is a viable method to measure the mechanical properties of inclusions in tissue phantoms and potentially the mechanical properties of breast lesions *in vivo*. It warrants clinical evaluation and further research into the relationship between tissue properties and diseased states.

Appendix A

Phantom Making Protocol

A.1 Ultrasound

The following steps are for each part of the phantom. That is if there are multiple layers to the phantom, depending on the mold and location of the inclusions, each layer can be creating as follows. Layers will adhere to each other well, however, to avoid mechanical discontinuities slightly melt hardened layers with warm water before pouring an adjacent layer.

1. Material Concentrations by Mass:

   8-16% Gelatin (Porcine, ~ 300 or ~ 175 bloom)

   0.2% Methyl Paraben (Methyl 4-Hydroxybenzoate, Preservative)

   2.0% Silica

   89.8-82.8% Distilled, Deionized Water

   +10% Extra Distilled, Deionized Water (To account for losses)

   ——————————————————————————

   110% Total

   As a rule, make approximately 50-100 grams more phantom mixture than required at each step.

2. Measure out desired amounts of materials. Place silica in a glass petri dish and add about $10ml$ of measured water. Place dish in a degassing chamber and degas until the addition to the gelatin.

3. Put remaining water in a degassing flask with a magnetic stirrer and simultaneously degas and heat the beaker. Degas for $\sim$ 5 minutes and bring to a temperature of approximately 70 degrees Celsius. Once the water is at the maximum temperature, begin stirring the water rapidly and add the methyl paraben. After the methyl paraben has dissolved, continue stirring rapidly and add the gelatin. Begin to degas the mixture as the gelatin is dissolving, being careful not to aspirate the foam which is created.

4. Once the gelatin has dissolved, turn off the heat and slow the stirring but continue to degas the mixture. As the mixture is cooling add the degassed silica/water mixture and continue to degas the entire mixture. The degassing may need to be done in several steps. After the mixture is degassed and cooled such that water is no longer evaporating from the mixture, transfer mixture from degassing flask to a beaker and continue to stir.

5. Place the beaker in a cool water bath and continue to stir. Gradually bring down the temperature of the water bath while stirring the mixture. The minimum temperature required before the mixture is ready to pour depends on the gelatin concentration and the silica concentration. Typically, a few degrees above room temperature is enough to ensure minimal settling of the silica particles to the bottom of the mold. When the mixture has sufficiently cooled, pour it into the desired mold.

6. After the phantom has been poured, place the mold into the fridge and refrigerate for several hours.

A.2   Tomosynthesis

The following steps are for each part of the phantom. That is if there are multiple layers to the phantom, depending on the mold and location of the inclusions, each layer can be creating as follows. Layers will adhere to each other well, however, to avoid mechanical discontinuities slightly melt hardened layers with warm water before pouring an adjacent layer.

1. Material Concentrations by Mass:

   8-16% Gelatin (Porcine, ~ 300 or ~ 175 bloom)

   0.2% Methyl Paraben (Methyl 4-Hydroxybenzoate, Preservative)

   2.0% Chalk Particles (~ 0.6-$1.2 mm$ in diameter)

   89.8-82.8% Distilled, Deionized Water

   +10% Extra Distilled, Deionized Water (To account for losses)

   _____

   110% Total

   As a rule, make approximately 50-100 grams more phantom mixture than required at each step.

2. Crush chalk with a mortar and pestle such that largest chalk pieces are just bigger than upper limit of the diameter. Use appropriate sieve sizes to sort out chalk pieces. Continue process until desired amount of particles are collected. Measure desired amount of other materials.

3. Put water in a degassing flask with a magnetic stirrer and simultaneously degas and heat the beaker. Degas for ~ 5 minutes and bring to a temperature of approximately 70 degrees Celsius. Once the water is at the maximum temperature, begin stirring the water rapidly and add the methyl paraben. After the methyl paraben has dissolved,

continue stirring rapidly and add the gelatin. Begin to degas the mixture as the gelatin is dissolving, being careful not to aspirate the foam which is created. Although air bubbles will largely not effect the out come of the x-ray images, the degassing process helps to speed the dissolving of the gelatin.

4. Once the gelatin has dissolved, turn off the heat and slow the stirring. After the mixture is cooled such that water is no longer evaporating from the mixture, transfer mixture from degassing flask to a beaker. Place the beaker in a cool water bath and continue to stir. When the solution has cooled to about ten degrees above room temperature, add the chalk particles and stir them into the mixture by hand. Continue to stir the mixture by hand while cooling it in in the water bath.

5. At the point when the chalk particles no longer settle to the bottom of the beaker, quickly pour the mixture into the mold. Careful attention must be paid in this step because the point at which the chalk stops settling and the point at which the gelatin is too viscous to pour are very close.

6. After the phantom has been poured, place the mold into the fridge and refrigerate for several hours.

References

American Cancer Society (2006a). Detailed guide: Breast cancer. www.cancer.org.

American Cancer Society (2006b). Detailed guide: Cancer (general information). www.cancer.org.

American Cancer Society (2006c). Mammograms and other breast imaging procedures. www.cancer.org.

American Cancer Society (2006d). Overview: Breast cancer. www.cancer.org.

Anderson, W. A. D., editor (1977). *Pathology*. Mosby, St. Louis.

Bamber, J. C., Barbone, P. E., Bush, N. L., Cosgrove, D. O., Doyley, M. M., Fueschel, F. G., Meaney, P. M., Miller, N. R., Shiina, T., and Tranquart, F. (2002). Progress in freehand elastography of the breast. *The Insitute of Electronics, Information and Communication Engineers Transactions on Information and Systems*, E85-D:5–15.

Barbone, P. E. and Bamber, J. C. (2002). Quantitative elasticity imaging: What can and what cannot be inferred from strain images. *Physics in Medicine and Biology*, 47:2147–2164.

Barbone, P. E. and Gokhale, N. H. (2004). On the uniqueness and nonuniqueness of the elastography inverse problem in two dimensions. *Inverse Problems*, 20:283–296.

Bassett, L. W. and Kimme-Smith, C. (1991). Breast sonography. *American Journal of Roentgenology*, 156:449–455.

Bercoff, J., Tanter, M., and Fink, M. (2004). Supersonic shear imaging: A new technique for soft tissue elasticity mapping. *IEEE Transactions on Ultrasonics, Ferroelectrics, and Frequency Control*, 51:396–409.

Boverman, G., Miller, E., Li, A., Zhang, Q., Chaves, T., Brooks, D. H., and Boas, D. A. (2005). Quantative spectroscopic diffuse optical tomography of the breast guided by imperfect a priori structural information. *Physics in Medicine and Biology*, 50:3941–3956.

Chaturvedi, P., Insana, M., and Hall, T. (1998). Testing the limitations of 2-d companding for strain imaging using phantoms. *IEEE Transactions on Ultrasonics, Ferroelectrics, and Frequency Control*, 45:1022–1031.

Chen, S., Fatemi, M., and Greenleaf, J. F. (1996). Quantifying elasticity and viscosity from measurement of shear wave speed dispersion. *Journal of the Acoustical Society of America*, 2:1185–1188.

Chen, Z. and Ning, R. (2003). Why should breast tumour detection go three dimensional? *Physics in Medicine and Biology*, 48:2217–2228.

de Korte, C. L. (1999). *Intravascular Ultrasound Elastography.* PhD thesis, Erasmus University Rotterdam.

Dobbins, J. T. and Godfrey, D. J. (2003). Digital x-ray tomosynthesis: Current state of the art and clinical potential. *Physics in Medicine and Biology*, 48:R65–R106.

Doyley, M. M., Meaney, P. M., and Bamber, J. C. (2000). Evaluation of an iterative reconstruction method for quantitative elastography. *Physics in Medicine and Biology*, 45.

Elmore, J. G., Barton, M. B., Moceri, V. M., Polk, S., Arena, P. J., and Fletcher, S. W. (1998). Ten-year risk of false positive screening mammograms and clinical breast examinations. *The New England Journal of Medicine*, 338:1089–1096.

Fatemi, M. and Greenleaf, J. F. (1998). Ultrasound-stimulated vibro-acoustic spectrography. *Science*, 280:82–85.

Fatemi, M., Wold, L. E., Alizad, A., and Greenleaf, J. F. (2002). Vibro-acoustic tissue mammography. *IEEE Transactions on Medical Imaging*, 21:1–8.

Fletcher, S. W. and Elmore, J. G. (2003). Mammographic screening for breast cancer. *The New England Journal of Medicine*, 348:1672–1680.

Fung, Y. C. (1993). *Mechanical Properties of Living Tissues.* Springer, New York.

Gao, L., Parker, K. J., Lerner, R. M., and Levinson, S. F. (1996). Imaging of the elastic properties of tissue-a review. *Ultrasound in Medicine and Biology*, 22:959–977.

Garra, B. S., Céspedes, E. I., Ophir, J., Spratt, S. R., Zuurbier, R. A., Magnant, C. M., and Pennanen, M. F. (1997). Elastography of breast legions: Initial clinical results. *Radiology*, 202:79–86.

Gokhale, N. H., Richards, M. S., Oberai, A. A., Barbone, P. E., and Doyley, M. M. (2004). Simultaneous elastic image registration and elastic modulus reconstruction. *IEEE International Symposium on Biomedical Imaging: Macro to Nano*, 1:543–546.

Goss, S. A., Johnston, R. L., and Dunn, F. (1978). Comprehensive compilation of emperical ultrasonic properties of mammalian tissues. *Journal of the Acoustical Society of America*, 64:423–457.

Hall, T. J., Bilgen, M., Insana, M. F., and Chaturvedi, P. (1996). Phantoms for elastography. *Proceedings of the IEEE Ultrasonics Symposium*, 2:1193–1196.

Hall, T. J., Zhu, Y., and Spalding, C. S. (2003). In vivo real-time freehand palpation imaging. *Ultrasound in Medicine and Biology*, 29:427–435.

Harris, J. R., Lippman, M. E., Morrow, M., and Hellman, S. (1996). *Diseases of the Breast*. Lippincott-Raven Publishers.

Homolka, P., Gahleitner, A., Prokop, M., and Nowotny, R. (2002). Optimization of the composition of phantom materials for computed tomography. *Physics in Medicine and Biology*, 47:2907–2916.

Houten, E. E. W. V., Miga, M. I., Weaver, J. B., Kennedy, F. E., and Paulsen, K. D. (2001). Three-dimensional subzone-based reconstruction algorithm for mr elastography. *Magnetic Resonance in Medicine*, 45:827–837.

Hughes, T. J. R. (1999). *The Finite Element Method*. Dover Publications.

Insana, M. F. and Bamber, J. C. (2000). Special issue on tissue motion and elasticity imaging. *Physics in Medicine and Biology*, 45.

Jackson, V. P. (1990). The role of us in breast imaging. *Radiology*, 177:305–311.

Jackson, V. P., Hendrick, R. E., Feig, S. A., and Kopans, D. B. (1993). Imaging of radiographically dense breast. *Radiology*, 188:297–301.

Jain, R. K. (1999). Transport of molecules, particles, and cells in solid tumors. *Annual Review of Biomedical Engineering*, 1:241–263.

Kallel, F. and Bertrand, M. (1996). Tissue elasticity reconstruction using linear perturbation method. *IEEE Transactions on Medical Imaging*, 15:229–313.

Keys, R. (1981). Cubic convolution interpolation for digital image processing. *IEEE Transactions on Acoustics, Speech and Signal Processing*, 29:1153–1160.

Kolen, A. F., Miller, N. R., Ahmed, E. E., and Bamber, J. C. (2004). Characterization of cardiovascular liver motion for the eventual application of elasticity imaging to the liver in vivo. *Physics in Medicine and Biology*, 49:4187–4206.

Kriege, M., Brekelmans, C. T., Boetes, C., Besnard, P. E., Zonderland, H. M., Obdeijn, I. M., Manoliu, R. A., Kok, T., Peterse, H., Tilanus-Linthorst, M. M., Muller, S. H., Meijer, S., Oosterwijk, J. C., Beex, L. V., Tollenaar, R. A., de Koning, H. J., Rutgers, E. J., and Klijn, J. G. (2004). Efficacy of mri and mammography for breast-cancer screening in women with a familial or genetic predisposition. *New England Journal of Medicine*, 351:427–437.

Krouskop, T. A., Wheeler, T. M., kallel, F., Garra, B. S., and Hall, T. (1998). Elastic moduli of breast and prostate tissues under compression. *Ultrasonic Imaging*, 20:260–274.

Macowski, A. (1983). *Medical Imaging.* Prentice-Hall,Inc.

Manduca, A., Oliphant, T. E., Dresner, M., Mahowald, J. L., Kruse, S. A., Amromin, E., Felmlee, J. P., Greenleaf, J. F., and Ehman, R. L. (2001). Magnetic resonance elastography: Noninvasive mapping of tissue elasticity. *Medical Image Analysis*, 5:237–254.

Nathanson, S. D. and Nelson, L. (1994). Interstitial fluid pressure in breast cancer, benign breast conditions, and breast parenchyma. *Annals of Surgical Oncology*, 1:333–338.

Nightingale, K., Soo, M. S., Nightingale, R., and Trahey, G. (2002). Acoustic radiation force impulse imaging: In vivo demonstration of clinical feasibility. *Ultrasound in Medicine and Biology*, 28:227–235.

Niklason, L. T., Christian, B. T., Niklason, L. E., Kopans, D. B., Castleberry, D. E., Opsahl-Ong, B. H., Landberg, C. E., Slanetz, P. J., Giardino, A. A., Moore, R., Alagli, D., DeJule, M. C., Fitzgerald, P. F., Fobare, D. F., Giambattista, B. W., Kwasnick, R. F., Liu, J., Lubowski, S. J., Possin, G. E., Richotte, J. F., Wei, C., and Wirth, R. F. (1997). Digital tomosynthesis in breast imaging. *Radiology*, 205:399–406.

Nocedal, J. (1980). Updating quasi-newton matrices with limited storage. *Mathematics of Computation*, 35:773–782.

Oberai, A. A., Gokhale, N. H., Doyley, M. M., and Bamber, J. C. (2004). Evaluation of the adjoint equation based algorithm for elasticity imaging. *Physics in Medicine and Biology*, 49:2955–2974.

Oberai, A. A., Gokhale, N. H., and Feijóo, G. R. (2003). Solution of inverse problems in elasticity imaging using the adjoint method. *Inverse Problems*, 19:297–313.

Ophir, J., Alam, S. K., Garra, B., Kallel, F., Konofagou, E., Krouskop, T., and Varghese, T. (1999). Elastography: ultrasonic estimation and imaging of the elastic properties of tissue. *Proceedings of the Institution of Mechanical Engineers*, 213:203–233.

Ophir, J., Céspedes, I., Ponnekanti, H., Yazdi, Y., and Li, X. (1991). Elastography: a method for imaging the elasticity of biological tissues. ultrasonic imaging. *Ultrasonic Imaging*, 13:111–134.

Ophir, J., Kallel, F., Varghese, T., Konofagou, E., Alam, A. K., Krouskop, T., Garra, B., and Righetti, R. (2001). Elastography. *Comptes Rendus de l'Acadmie des Sciences - Series IV - Physics*, 2:1193–1212.

Oppenheim, A. V. and Schafer, R. W. (1999). *Discrete-Time Signal Processing.* Prentice-Hall,Inc.

Paszek, M. J., Zahir, N., Johnson, K. R., Lakins, J. N., Rozenberg, G. I., Gefen, A., Reinhart-King, C. A., Marguilies, S. S., Dembo, M., Boettiger, D., Hammer, D. A., and Weaver, V. M. (1999). Transport of molecules, particles, and cells in solid tumors. *Annual Review of Biomedical Engineering*, 1:241–263.

Polletti, M. E., Goncalves, O. D., and Mazzaro, I. (2002). X-ray scattering from human breast tissues and breast-equivalent materials. *Physics in Medicine and Biology*, 47:47–63.

Powell, D. E. and Stelling, C. B. (1994). *The Diagnosis and Detection of Breast Disease*. Mosby.

Press, W. H., Teukolsky, S. A., Vetterling, W. T., and Flannery, B. P. (2002). *Numerical Recipes in C++:The Art of Scientific Computing*. Cambridge University Press.

Ross, A. S., Saulnier, G. J., Newell, J. C., and Isaacson, D. (2003). Current source design for electrical impedance tomography. *Physiological Measurement*, 24:509–516.

Rownd, J., Madsen, E. L., Zagzebski, J. A., Frank, G., and Dong, F. (1997). Phantoms and automated system for testing resolution of ultrasound scanners. *Ultrasound in Medicine and Biology*, 23:245–260.

Sarntinoranont, M., Rooney, F., and Ferrari, M. (2003). Interstitial stress and fluid pressure within a growing tumor. *Annals of Biomedical Engineering*, 31:327–335.

Sarvazyan, A. P., Rudenko, O. V., Swanson, S. D., Fowlkes, J. B., and Emelianov, S. Y. (1998). Shear wave elasticity imaging: A new ultrasonic technology of medical diagnostics. *Ultrasound in Medicine and Biology*, 24:1419–1435.

Simonetti, G., Cossu, E., Montanaro, M., Caschili, C., and Giuliani, V. (1998). Whats new in mammography. *European Journal of Radiology*, 27:S238–S241.

Sinkus, R., Lorenzen, J., Schrader, D., Lorenzen, M., Dargatz, M., and Holz, D. (2000). High-resolution tensor mr elastography for breast tumour detection. *Physics in Medicine and Biology*, 45:1649–1664.

Skovoroda, A. R., Emelianov, S. Y., and O'Donnell, M. (1995). Tissue elasticity reconstruction based on ultrasonic displacement and strain images. *IEEE Transactions on Ultrasonics, Ferroelectronics, and Frequency Control*, 42:747–765.

Smith, R. A., Saslow, D., Sawyer, K. A., Burke, W., Costanza, M. E., III, W. P. E., Foster, R. S., Hendrick, E., Eyre, H. J., and Sener, S. (2003). American cancer society guidelines for breast cancer screening: Update 2003. *CA: A Cancer Journal for Clinicians*, 53:141–169.

Taylor, L. S., Porter, B. C., Rubens, D. J., and Parker, K. J. (2000). Three-dimensional sonoelastography: principles and practices. *Physics in Medicine and Biology*, 45:1477–1494.

Walker, W. F. and Trahey, G. E. (1995). A fundamental limit on delay estimation using partially correlated speckle signals. *IEEE Transactions on Ultrasonics, Ferroelectrics, and Frequency Control*, 42:301–308.

Wellman, P., Howe, R. H., Dalton, E., and Kern, K. A. (1999). Breast tissue stiffness in compression is correlated to histological diagnosis. Technical report, Harvard Biorobotics Laboratory.

Wu, T., Stewart, A., Stanton, M., McCauley, T., Phillips, W., Kopans, D. B., Moore, R. H., Eberhard, J. W., Opsahl-Ong, B., Niklason, L., and Williams, M. B. (2003). Tomographic mammography using a limited numbber of low-dose cone-beam projection images. *Medical Physics*, 30:365–380.

Zitova, B. and Flusser, J. (2003). Image registration methods: A survey. *Image and Vision Computing*, 21:977–1000.

CURRICULUM VITAE

Michael Scott Richards

Department of Radiology
University of Michigan Medical Center
3315 Kresge III
200 Zina Pilcher Place
(617) 413-8247
msrichar@umich.edu

Research Interests:

Diagnostic Ultrasound
Biomechanics
Therapeutic Ultrasound
Signal/Image Processing
Biomechanical Systems

Education:

2001-2007 **Boston University   MS/Ph.D. Biomedical Engineering**
"Quantitative Three Dimensional Elasticity Imaging." Advisor: Paul E. Barbone, Ph.D.

1997-2001 **University of Rochester   B.S. Biomedical Engineering**

Awards:

National Institutes of Health Ph.D. Training grant in Quantiative Biology and Physiology, Boston University, Biomedical Engineering Department, 2001.

First Place, ASME International Mechanical Engineering Congress and Exposition, Bioengineering Division's Student Paper Competition, 2001.

The Charles L. Neuton Prize for Engineering Proficiency, University of Rochester, 2001.

Research Experience:

2006-present	**Department of Radiology, University of Michigan Medical Center** (1) Developing elastic modulus imaging technique, using three dimensional ultrasound imaging, for a clinical mammography study evaluating methods to improve mammographic specificity.
2002-2006	**Biomechanical Imaging Group, Boston University Research Assistant** (1) Developing cross correlation based and finite element based algorithms for three dimensional image registration and displacement estimation. (2) Developing algorithms to solve the finite element based inverse problem which calculates shear modulus distributions from measured displacement fields. (3) Developing protocol for the creation of tissue mimicking phantoms to be used in ultrasound and x-ray mechanical imaging experiments. (4) Building the experimental setup and protocol for image acquisition during mechanical compression experiments for both ultrasound and x-ray tomosynthesis imaging systems. (5) Developing statistical analysis for evaluating the accuracy and resolution of mechanical measurements using ultrasound and x-ray systems.
2000-2001	**University of Rochester: Rochester, NY Senior Project** Characterization of the mechanical properties of soft tissue. Performed creep and stress relaxation tests on bovine liver tissue and modeled the viscoelastic stress/strain response. The purpose of the work was to characterize tissue properties for sonoelastography imaging experiments.
Summer 2000	**Massachusetts Institute of Technology: Boston, MA Internship** Studied the molecular and biochemical mechanisms that regulate adult stem cell kinetics. Specifically the p53 tumor suppressor gene and its regulated expression in rat liver stem cells.

Professional Development:

July 2005   Mayneord-Phillips Summer School: *Ultrasound and Other Minimally-Invasive Therapies*
Oxford, UK

Technical Qualifications:

MATLAB, FORTRAN 90, C/C++, NASTRAN, OPENMP, LINUX, UNIX, MAC OS, WINDOWS

Publications:

Gokhale, N.H., Richards, M.S., Oberai, A.A., Barbone, P.E., Doyley, M.M. *"Simultaneous Elastic Image Registration and Elastic Modulus Reconstruction"* Proceedings International Symposium on Biomedical Imaging 2004: From Nano to Macro, Institute of Electrical and Electronics Engineers 2nd International Symposium on Biomedical Imaging, April 2004.

Conference Proceedings / Abstracts:

Barbone, P.E., Richards, M.S., Gokhale, N.H., Rivas Aroni, C., Leiderman, R., Bamber, J.C., Oberai, A.A. *"Progress In Quantitative Biomechanical Imaging"* Institute for Mathematics and its Applications Workshop W10.17-21.05, Imaging from Wave Propagation, October 2005.

Gokhale, N.H., Richards, M.S., Doyley, M.M., Oberai, A.A., Barbone, P.E. *"Imposing Physical Constraints to Yield Accurate and Unbiased Displacement Estimates"* Proceedings of the Third International Conference on the Ultrasonic Measurement and Imaging of Tissue Elasticity, October 2004.

Taylor, L.S., Richards, M.S., Moskowitz, A.J., Lerner, A.L., Rubens, D.J., and Parker, K.J. *"Viscoelastic Effects in Sonoelastography: Impact on Tumor Detectability"* Institute of Electrical and Electronics Engineers Ultrasonics Symposium Proceedings, 2001. Vol. 2, 1639-1642.

Richards, M.S., Moskowitz, A.J., Taylor, L.S., and Lerner, A.L. *"Modeling the Viscoelastic Response of Bovine Liver Tissue"* American Society Of Mechanical Engineers International Mechanical Engineering Congress and Exposition, 2001.

Conference Presentations:

Richards, M.S., Oberai, A.A., Barbone, P.E., Gokhale, N.H. *"Three-dimensional ultrasound image registration and shear modulus reconstruction."* 151st Meeting of the Acoustical Society of America, June 2006. (Oral Presentation)

Richards, M.S., Barbone, P.E., Oberai, A.A., Gokhale, N.H., Wu, T., Moore, R.H. and Kopans, D.B., Bamber, J.C. *"Three Dimensional Image Registration and Elastic Shear Modulus Reconstruction"* Center for Subsurface Sensing and Imaging Systems Research and Industrial Collaboration Conference, October 2005. (Invited Oral Presentation)

Barbone, P.E., Richards, M.S., Gokhale, N.H., Rivas Aroni, C., Leiderman, R., Bamber, J.C., Oberai, A.A. *"Progress In Quantitative Biomechanical Imaging"* Center for Subsurface Sensing and Imaging Systems Research and Industrial Collaboration Conference, October 2005. (Poster)

Richards, M.S., Barbone, P.E., Oberai, A.A., Gokhale, N.H., Wu, T., Moore, R.H. Kopans, D.B., Bamber, J.C. *"Three Dimensional Ultrasound Image Registration and Shear Elastic Modulus Reconstruction."* Fourth International Conference on the Ultrasonic Measurement and Imaging of Tissue Elasticity, October 2005. (Oral Presentation)

Barbone, P.E., Richards, M.S., Gokhale, N.H., Rivas Aroni, C., Leiderman, R., Bamber, J.C., Oberai, A.A. *"Progress In Quantitative Biomechanical Imaging"* GTCBio International Conference on Tumor Progression and Therapeutic Resistance, September 2005. (Poster)

Richards, M.S., Barbone, P.E., Oberai, A.A., Gokhale, N.H., Wu, T., Moore, R.H. and Kopans, D.B. *"Quantitative Three Dimensional Elasticity Imaging"* Center for Subsurface Sensing and Imaging Systems National Science Foundation Annual Site Visit, April 2005. (Poster)

Richards, M.S., Barbone, P.E., Oberai, A.A., Gokhale, N.H., Wu, T., Moore, R.H. and Kopans, D.B. *"Quantitative Three Dimensional Elasticity Imaging"* Center for Subsurface Sensing and Imaging Systems Research and Industrial Collaboration Conference, October 2004. (Poster)

Richards, M.S., Barbone, P.E., Wu, T., Moore, R.H. and Kopans, D.B. *"X-Ray Tomosynthesis Elastography: A Feasibility Study"* Center for Subsurface Sensing and Imaging Systems Research and Industrial Collaboration Conference, November 2003. (Poster)

Richards, M.S., Barbone, P.E., Wu, T., Moore, R.H. and Kopans, D.B. *"X-Ray Tomosynthesis Elastography: A Feasibility Study"* Second International Conference on the Ultrasonic Measurement and Imaging of Tissue Elasticity , October 2003. (Poster)

Richards, M.S., Barbone, P.E., Wu, T., Moore, R.H. and Kopans, D.B. *"X-Ray Tomosynthesis Elastography: A Feasibility Study"* Center for Subsurface Sensing and Imaging Systems National Science Foundation Annual Site Visit, March 2003. (Poster)

Richards, M.S., Barbone, P.E. *"Estimating Tissue Displacement from a Series of Ultrasound Images"* Center for Subsurface Sensing and Imaging Systems Research and Industrial Collaboration Conference, December 2002. (Poster)